STRUCTURAL AND FUNCTIONAL STUDIES OF TYPE THREE SECRETION VIRULENCE

FACTORS FROM GRAM NEGATIVE PATHOGENIC BACTERIA

A DISSERTATION IN

Cell Biology and Biophysics

and

Molecular Biology and Biochemistry

Presented to the Faculty of the University

of Missouri-Kansas City in partial fulfillment of

the requirements for the degree

Doctor of Philosophy

by

MICHAEL L BARTA

B.S., Kansas State University, 2007

Kansas City, Missouri

STRUCTURAL AND FUNCTIONAL STUDIES OF TYPE THREE SECRETION VIRULENCE

FACTORS FROM GRAM NEGATIVE PATHOGENIC BACTERIA

Michael L. Barta, Candidate for the Doctor of Philosophy Degree

University of Missouri-Kansas City, 2011

ABSTRACT

Many pathogenic Gram-negative bacteria utilize type III secretion systems (TTSS) to alter the normal functions of target host epithelial cells. Of the 1.1 million deaths that are caused by *Shigella* each year, nearly a third are in children under five years of age. *Salmonella enterica* serovar Typhimurium is the leading cause of hospitalization and death due to food-borne gastroenteritis in the U.S. The pathogenesis of both of these species involves the invasion of epithelial cells of the gastrointestinal tract, which requires the use of a type III secretion system (TTSS). The *Shigella* type III secretion apparatus (TTSA) is composed of a basal body spanning both bacterial membranes and an exposed oligomeric needle. Host altering effectors are secreted through this energized conduit to promote bacterial invasion. The active needle-tip complex of *S. flexneri* is composed of a tip protein, IpaD, and two pore-forming translocators, IpaB and IpaC. Maturation of the needle-tip complex proceeds in a stepwise manner. IpaD is at the tip of the nascent TTSA needle where it controls the first step of TTS activation. The bile salt deoxycholate (DOC) binds to IpaD to induce recruitment of the first translocator, IpaB, into the maturing tip complex. The pore-forming translocators are bound by the class II chaperone, IpgC, within the bacterial cytoplasm in order to prevent premature

association and degradation. Despite their importance in promoting *Shigella* virulence, few

molecular level details are known regarding the interactions between IpgC and its targets, IpaB and

IpaC. Additionally, the mechanism by which DOC serves to stabilize a conformational change within

IpaD is poorly understood. Methods in structural biology, in particular X-ray crystallography, are

extremely valuable in addressing such questions. We present here the crystal structures of IpgC

(identifying an alternative quaternary state), DOC-bound IpaD and the N-terminal regions of both

IpaB and SipB, the *S.* Typhimurium first translocator homolog. These structures have facilitated the

functional analysis of crucial determinants of Gram-negative pathogens that would otherwise not

have been possible. Additionally, these structural studies have revealed the critical α-helical nature of

each protein subunit involved in mature needle-tip-translocon formation.

APPROVAL PAGE

The faculty listed below, appointed by the Dean of the School of Biological Sciences, have examined a dissertation titled "Structural and Functional Studies of Type Three Secretion Virulence Factors from Gram-negative Pathogenic Bacteria," presented by Michael L. Barta, candidate for the Doctor of Philosophy degree, and certify that in their opinion it is worthy of acceptance.

Supervisory Committee

Brian Geisbrecht, Ph.D., Committee Chair

Cell Biology and Biophysics

Lawrence Dreyfus, Ph.D.

Dean, School of Biological Sciences

Samuel Bouyain, DPhil

Molecular Biology and Biochemistry

Alexander Idnurm, Ph.D

Cell Biology and Biophysics

Gerald Wyckoff, Ph.D.

Molecular Biology and Biochemistry

CONTENTS

Chapter

LIST OF ILLUSTRATIONS

LIST OF TABLES

LIST OF ABBREVIATIONS

Burkholderia invasion chaperone A	(BicA)
Circular dichroism spectroscopy	(CD)
Deoxycholate	(DOC)
Forster resonance energy transfer	(FRET)
Invasion plasmid antigen B	(IpaB)
Invasion plasmid antigen C	(IpaC)
Invasion plasmid antigen D	(IpaD)
Invasion plasmid gene C	(IpgC)
Isopropyl β-D-1-thiogalactopyranoside	(IPTG)
Liquid Chromatography Mass Spectrometry	(LC-MS)
Membrane expression of ipa E	(MxiE)
Phosphate-buffered saline	(PBS)
Salmonella invasion chaperone A	(SicA)
Salmonella invasion protein B	(SipB)
Salmonella invasion protein D	(SipD)
Species	(Spp.)
Specific Yersinia chaperone D	(SycD)
Tetratricopeptide repeat	(TPR)
Tobacco etch virus	(TEV)
Trypticase soy broth	(TSB)
Type III Secretion Apparatus	(TTSA)
Type III Secretion System	(TTSS)

ACKNOWLEDGEMENTS

CHAPTER 1

INTRODUCTION

Diarrheal diseases caused by bacterial pathogens are a major public health burden, with the

World Health Organization (WHO) estimating that 4.5 billion incidences of diarrhea led to 1.8

million deaths in 2002 (68). Of these infectious cases, five to fifteen percent can be attributed to

Shigella infection, with upwards of 1.1 million fatalities (50, 65). While the large majority of cases

(~99%) are limited to underdeveloped countries due to malnutrition, limited hygiene and

contaminated water, shigellosis has become a problem for daycares, nursing homes and natural

disaster regions (60). Transmission of *Shigella* spp. occurs by the oral-fecal route within bacteria

entering the body by ingestion of contaminated food and water sources. Acquisition of infection can

occur with consumption of as few as 10-100 microorganisms (25). Shigellosis, a severe form of

bacillary dysentery characterized by inflammation of the intestinal lining, fever, cramps and bloody

diarrhea (84), begins with bacterial invasion of the colonic epithelial cells.

Shigella pathogenesis studies have centered on the mechanisms of *Shigella flexneri* and much

of the current knowledge is indeed based upon this species (84). Upon reaching the large intestine, *S.

flexneri* initiates infection by invading in a multistep process (**Figure 1**). Penetrating the intestinal

epithelium, the body's physical and functional pathogen barrier (81), begins via transcytosis within

microfold cells (M cells) to the basolateral side (82, 98). Upon transcytosis, *S. flexneri* is engulfed by

macrophages where it rapidly induces apoptosis (105, 106), allowing bacterial escape and release of

proinflammatory cytokines (104). Massive inflammation results from this flood of cytokines which

eventually leads to archetypical *S. flexneri* pathology. Upon release from macrophages, invasion of

epithelial cells (EC) occurs from the basolateral side. Bacterial replication within host ECs occurs in

1
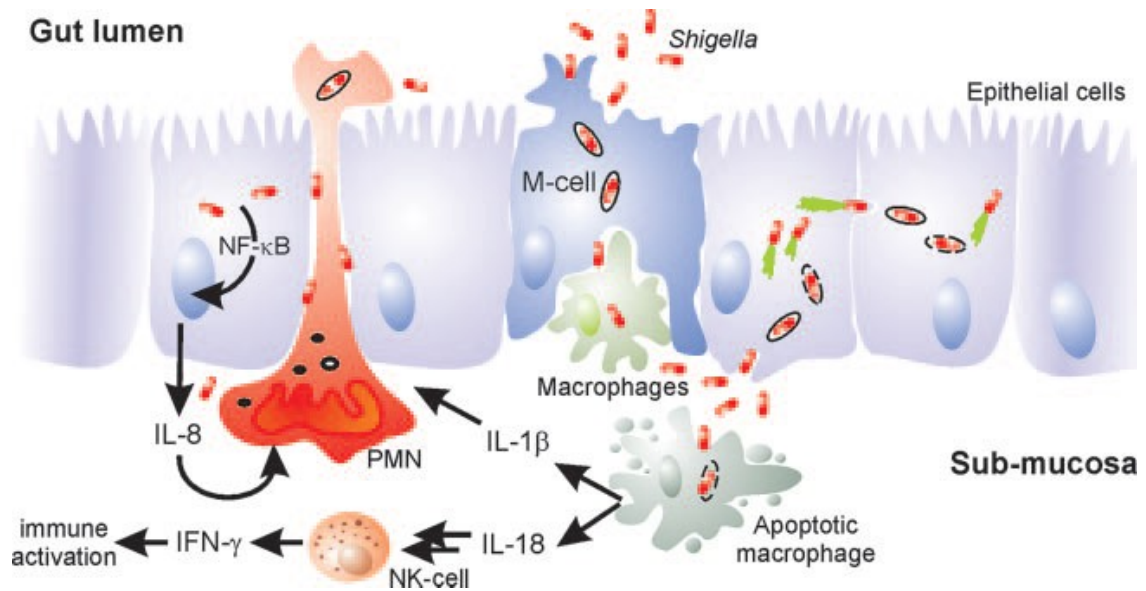
FIGURE 1. Cellular pathogenesis of *Shigella* spp. *S. flexneri* passes the EC barrier by transcytosis through M cells and encounters resident macrophages. The bacteria evade degradation in macrophages by inducing an apoptosis-like cell death, which is accompanied by proinflammatory signaling. Free bacteria invade the EC from the basolateral side, move into the cytoplasm by vectorial actin polymerization, and spread to adjacent cells. Proinflammatory signaling by macrophages and EC further activates the innate immune response involving NK cells and attracts PMN. The influx of PMN disintegrates the EC lining, which initially exacerbates the infection and tissue destruction by facilitating the invasion of more bacteria. Ultimately, PMN phagocytose and kill *Shigella*, thus contributing to the resolution of the infection. (84)

the cytoplasm (83). Movement from cell to cell is accomplished by polymerization of actin; protecting *S. flexneri* from extracellular, host immune response (6, 61). Recruitment of polymorphonuclear neutrophil leukocytes (PMN) to the site of infection initially exacerbates bacterial invasion, but ultimately results in resolution of the infection (11, 56). However, secreted bacterial effectors modulate the severity of inflammation by downregulating host immune responses. Exploitation of these signaling pathways allows the bacterium to evade the immune system and proliferate (74).

Manipulation of host cell signaling, as well as facilitation of initial invasion, is accomplished in Gram-negative bacteria such as *S. flexneri* and *Salmonella enterica* serovar Typhimurium via the Type Three Secretion System (TTSS). Bacteria expressing TTSS can be classified into phylogenetic families based upon the mechanism of infection and sequence conservation of the TTSS-specific genes (38). Genes encoding the TTSS (and the secreted 'late' effectors) are located on a 31-kb fragment of large virulence plasmid (17). While the *S. flexneri* TTSS is comprised of a single needle structure, *S.* Typhimurium encodes two separate TTSS within *Salmonella* pathogenicity island 1 (SPI-1) and SPI-2. Both bacterial species belong to the Inv-Mxi-Spa family of TTSS, which also includes *Burkholderia pseudomallei* and *Yersinia entericolitica* (94). TTSS from different bacterial species are generally conserved in ultrastructure, despite pathogen-host specific adaptations (17, 92). The architecture of the TTSS (**Figure 2**) is such that effectors are transported across three membranes: the inner and outer bacterial membrane as well as the host plasma membrane. This molecular syringe contains a cytoplasmic ATPase driven secretion apparatus (62), a seven-ringed basal body spanning both bacterial membranes (85, 86) and an external needle comprised of a helical polymer (9, 16). Structural visualization of the TTSS needle by transmission electron microscopy suggests that the narrow channel prevents transport of fully folded proteins. Indeed, it is believed that retention of some secondary structure elements, such as 2-helix bundles, are retained after partial unfolding at the secretion apparatus prior to secretion (20).

3
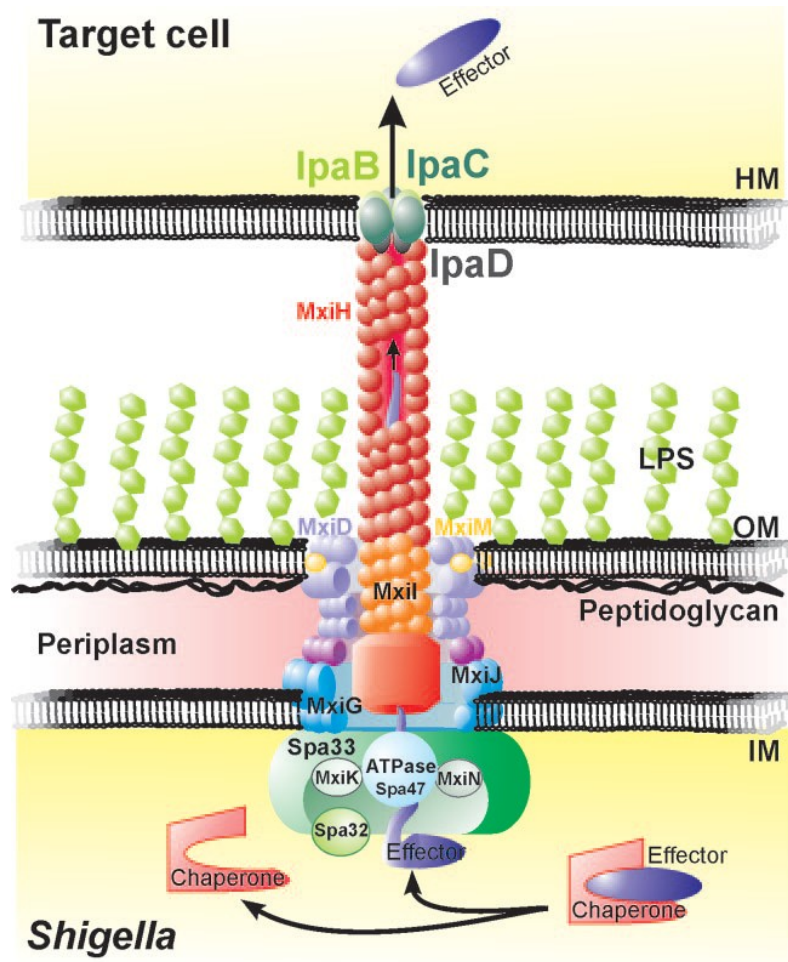
FIGURE 2. Architecture of the *S. flexneri* Mxi-Spa TTSS. The *S. flexneri* Mxi-Spa T3SS consists of four main parts. The seven-ringed basal body spans the bacterial IM, the periplasm, and the OM. The hollow needle is attached to a socket and protrudes from the basal body to the bacterial surface. Contact with host cell membranes (HM) triggers the IpaD-guided membrane insertion of the IpaB-IpaC translocon at the needle tip. The TTSS is completed by the cytoplasmic C ring, which is comprised of proteins that energize the transport process and mediate the recognition of substrates, chaperone release, and substrate unfolding. (84)

4

Injection of bacterial effectors into the host epithelial cell membrane and cytoplasm leads to large scale cytoskeletal rearrangement resulting in bacterial internalization (74). Bacterial control of the host innate immune response and modulation of the resulting inflammatory response is accomplished by a family of secreted *Shigella* 'late' effector proteins. Insertion of the translocon pore frees the class II chaperone IpgC from interaction with the translocators IpaB and IpaC (84). Unbound IpgC is then free to interact with the transcriptional activator, MxiE, promoting the expression and secretion of a panel of 'late' effector proteins (57, 76). Upon secretion through the TTSA, these substrates are responsible for numerous events promoting bacterial invasion and intracellular replication. These events include: promotion of actin polymerization at one pole of intracellularly located *Shigella* (IcsA and IpaC) (6, 52, 74), induction of rapid apoptotic death in macrophages via interaction with Caspase-1 (IpaB) (104-106), escape from host cell autophagy (IcsB) (66) and inhibition of pro-inflammatory factors (OspG) (74) among several other host innate immune response interactions. Manipulation of numerous host responses, accomplished by secretion of 'late' effectors through the TTSA, is thus critical for invasion, intracellular replication and dissemination of *Shigella*.

Assembly of the structural components of the TTSS is sufficient for transport of effector proteins. However, controlled secretion and formation of the translocon pore requires the translocator proteins IpaB and IpaC as well as the needle tip protein IpaD in *S. flexneri* (96). Prior to activation of the TTSS both translocator proteins are separately bound by the class II chaperone, IpgC, in order to prevent premature association (63). Maturation of the needle tip complex (and resulting translocon pore) proceeds in a step-wise manner in *S. flexneri* (**Figure 3**). Upon completion of the Type Three Secretion Apparatus (TTSA), the needle tip protein IpaD localizes to the distal end of the polymerized needle (30). Here, IpaD serves as an environmental sensor at the exposed end of the needle while forming a multimeric plug in order to prevent premature effector secretion (45, 75). Upon interacting with host bile salts, such as deoxycholate (DOC), IpaD undergoes a conformational

change, prompting the recruitment of the first translocator IpaB (24, 67, 90). Newly exposed IpaB detects host cell contact via membrane components, potentially with host membrane-bound cholesterol (36), inducing the recruitment of the second translocator IpaC (28). Both translocator proteins are now able to insert into the host membrane, forming the multimeric translocon pore and completing the TTSA conduit (8, 96). Bacterial effectors are translocated into the host cytoplasm, initiating invasion.

Class II chaperones are a conserved subset of proteins essential (63) to TTSS function that serve to prevent premature association of the translocator proteins, while maintaining them in a secretion competent state within the bacterial cytoplasm (73). In *S. flexneri*, the gene *ipgC* encodes a small (17-kDa) cytoplasmic chaperone protein. In the absence of IpgC the translocators interact within the bacterial cytoplasm and are targeted for degradation (84). Upon activation of the TTSS, and translocation of IpaB and IpaC, IpgC is free to interact with the AraC-like transcription factor, MxiE to promote expression of the late-effector genes (57). The crystal structure of the *Yersinia enterocolitica* chaperone, SycD, was reported in 2008 where dimerization was proposed to be essential for translocator interaction (13). The structure of SycD demonstrated that class II
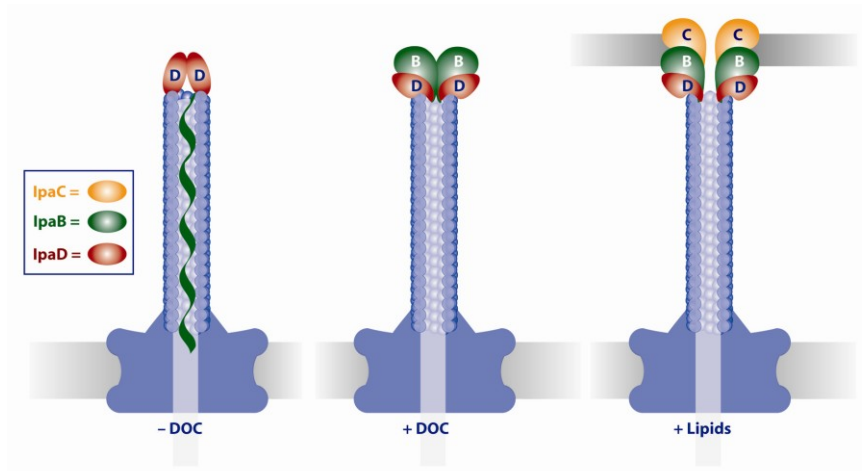
FIGURE 3. Step-wise Maturation of the Needle-Tip Complex. IpaD resides at the nascent TTSA needle tip (left). It is joined by IpaB after exposure to bile salts (center). Upon contact with liposomes, IpaC is recruited to the tip where it completes the TTSA conduit and with IpaB forms the nascent translocon. *In vivo* the translocon is deposited into the host cell membrane to allow translocation of effectors to promote host cell invasion [figure courtesy of Dr. Wendy Picking].

chaperones are all alpha-helical and comprised of tetratricopeptide repeats (TPR). Additionally, the cocrystal structure of PcrH from *Pseudomonas aeruginosa* was published in 2010 with a peptide comprising the chaperone binding domain (CBD) of the second translocator PopD (44). While both PcrH and SycD display a high sequence identity (~60%), they share a rather low 26% sequence identity with IpgC. However, all three chaperone proteins demonstrate a great deal of structural homology, specifically within the concave translocator binding cleft, indicating a conserved translocator binding approach across TTSS-possessing bacterial species. Additionally, we have demonstrated that IpgC can adopt two different quaternary structures, with both asymmetric (55) and head-to-head (3) dimerization interfaces being possible. The impact of variable class II chaperone quaternary states on translocator interaction has yet to be elucidated.

Prior to activation of the TTSA the *S. flexneri* needle tip protein localizes to the distal end of the polymerized needle, where it regulates the TTSS secretion state by forming a multimeric plug (30). Johnson *et al.* solved the crystal structure of IpaD in 2006. IpaD is dumbbell shaped in nature, with a stabilizing intramolecular coiled-coil flanked by domains on each terminus (45). The N-terminal two helix bundle acts as a chaperone domain, preventing premature oligomerization with the bacterial cytoplasm (45). Fluorescence spectroscopy experiments revealed that IpaD (and to a lesser extent, SipD from *S.* Typhimurium) could interact with bile salts, such as DOC (90). Interaction with host environmental bile salts induces a conformational change (24) within IpaD that stimulates recruitment of the first translocator IpaB to the nascent needle complex (67). Deletion of the distal C-terminal domain within IpaD disrupted the ability of IpaB to stably associate at the tip (45). Additionally, even short deletions with the C-terminal 5 residues of IpaD eliminates host cell invasion and pore formation (75). Incubation of *S. flexneri* with bile salts results in a concomitant increase in cultured cell invasion (28). Thus, IpaD functions as a small-molecule biosensor at the tip of the TTSA. Further elucidation of the mechanism of ternary tip complex maturation, required that we determine the cocrystal structure of IpaD bound to DOC. Identification of the bile salt binding site

allowed us to perform site directed mutagenesis to better understand the role of DOC in tip complex maturation. Elimination of the two residues believed to most strongly interact with DOC, greatly disrupted the ability of *S. flexneri* to invade cultured cells. Crystal structures of SipD bound to bile salts have recently been presented (14, 54). Comparison of the changes seen within the cocrystal structures of homologous needle tip proteins allows for pathogen-specific conclusions to be drawn. Ultimately, bile salt interaction with IpaD at the tip of the needle results in priming of the *S. flexneri* tip complex via recruitment of the first translocator IpaB, resulting in a single, discrete step towards host cell invasion.

While the atomic structures of several TTSA needle (20, 97, 103) and needle tip proteins (14, 45) have been elucidated, solving the structures of the translocators has met with little success, which is due in part to the apolar physical nature of these membrane-penetrating proteins. Lack of success in this area continues to hamper developing the full mechanistic understanding of the TTSA and the role of type III secretion in causing highly debilitating disease. In *Shigella*, newly exposed IpaB detects host cell contact via membrane components to induce recruitment of IpaC, the second translocator protein, to the bacterial surface where it works in concert with IpaB to form a pore in the host cell membrane (28). This allows subsequently secreted 'effector proteins' to pass through the TTSA conduit and into the target cell membrane. As is the case in all TTSS, the tip protein and both translocators are essential to bacterial pathogenesis (64). Within the C-terminal region of IpaB, the first translocator, two putative transmembrance helices (313-346 and 400-423) exist within a larger hydrophobic domain, proposed to interact with IpaC, the second translocator (4, 34, 72). Membrane insertion of IpaB requires tip-localized IpaD, but not the presence of IpaC (8). Identification of distinct structural domains within the translocator protein that is surface-exposed prior to actual host cell invasion would be expected to provide clues to discrete regions that are responsible for the protective capacity of this protein. An especially attractive feature of the needle tip protein (IpaD) and the mobilization of the first translocator protein (IpaB) is that the information derived from their

structure function relationships could provide the foundation for subunit vaccines for the prevention of shigellosis and salmonellosis. Here we present the structure for the N-terminal region of IpaB and its homolog SipB. We also examine the potential mechanisms of these proteins based on homology to structurally related pore-forming proteins.

CHAPTER 2

MATERIALS AND METHODOLOGY

Cloning, Overexpression and Purification of Recombinant Forms of Gram-negative Virulence Factors

Class II Chaperone from *Shigella flexneri* IpgC

A designer gene fragment encoding residues 10-155 of IpgC was amplified from the virulence plasmid of *S. flexneri* via PCR and subcloned into pT7HMT (31). Following confirmation of its DNA sequence, this expression vector was transformed into BL21 (DE3) *Escherichia coli* cells and cultured in Terrific Broth at 37°C to an $A_{600\ nm}$ of 0.8. Protein expression was induced overnight at 18°C by adding IPTG to 1 mM final concentration. Cells were harvested by centrifugation, resuspended in lysis buffer (20 mM Tris pH 8.0, 500 mM NaCl, and 10 mM imidazole), and then lysed in a microfluidizer. The soluble target protein was collected in the supernatant following centrifugation of the cell homogenate and purified on a Ni^{2+}-NTA Sepharose column according to standard protocols (31). Recombinant TEV protease was used to digest the fusion affinity tag from the target protein. After desalting into 20 mM Tris (pH 8.0), final purification was achieved by Resource Q anion-exchange chromatography (GE Biosciences). Following this, the purified protein was concentrated to 10 mg/mL and exchanged into H_2O for further use. A similar protocol was used to subclone, overexpress, and purify full-length IpgC, a further truncated form that consisted of residues 21-155 ($IpgC^{21-155}$), and the $IpgC^{1-151}$ variant described by Lunelli *et al.* (55). Expression vectors encoding the $Ala^{94}Glu/Val^{95}Gln$ double mutant of both $IpgC^{10-155}$ and $IpgC^{1-151}$ were generated by PCR using the two-step megaprimer method (12); the corresponding proteins were overexpressed and purified as described above.

11

Needle Tip Protein from *S. flexneri* IpaD

A gene fragment encoding residues 39–322 (possessing a C322S mutation to prevent covalent dimerization) of IpaD was amplified from the virulence plasmid of *S. flexneri* using PCR and the resulting fragment was subcloned into the expression plasmid pT7HMT (31). The sequence-confirmed plasmid was transformed into *E. coli* BL21 (DE3) cells, which were then cultured in Terrific Broth supplemented with kanamycin (50 μg/ml) at 37 $^{\circ}$C to an A_{600nm} of 0.8. Protein expression was induced overnight at 18 $^{\circ}$C by adding IPTG to 1 mM. Bacterial cells were harvested by centrifugation, resuspended in lysis buffer (20 mM Tris (pH 8.0), 500 mM NaCl, and 10 mM imidazole), and then lysed by microfluidization. The soluble tagged protein was collected in the supernatant following centrifugation of the cell homogenate and purified on a Ni^{2+}-NTA Sepharose column according to published protocols (31). Recombinant TEV protease was used to digest the fusion affinity tag from the target protein as previously described (31). After desalting into 20 mM Tris (pH 8.0), final purification was achieved by Resource Q anion-exchange chromatography (GE Biosciences). Following this, the purified protein was concentrated to 30 mg/ml, buffer exchanged by ultrafiltration into ddH_2O, and stored at 4 °C for further use.

First Translocators from *S. flexneri* and *Salmonella enterica* serovar Typhimurium, IpaB and SipB, respectively

Full-length IpaB (residues 1-580) was amplified from the virulence plasmid of *S. flexneri* via PCR and subcloned into pT7HMT (31). Upon verification of its DNA sequence, this expression vector was co-transformed, along with full-length IpgC (residues 1–155) in the pACYC-DUET vector (3), into BL21 (DE3) *E. coli* cells and cultured in kanamycin (50 μg/ml) / chloramphenicol (30 μg/ml)-selective Terrific Broth at 37°C to an $A_{600\ nm}$ of 0.800. Protein co-expression was induced overnight at 18°C by adding IPTG to 1 mM final concentration. Cells were harvested by centrifugation, resuspended in lysis buffer (20 mM Tris pH 8.0, 500 mM NaCl, and 10 mM

imidazole), and then lysed in a microfluidizer. Soluble translocator/chaperone complex was collected in the supernatant following centrifugation of the cell homogenate and purified on a Ni^{2+}-NTA Sepharose column according to standard protocols (31). Chromosomal *S.* Typhimurium DNA was used to amplify full-length SipB (residues 1–593) via PCR and subcloned into pACYC-DUET (Novagen). Co-expression and purification of sequence verified SipB with full-length SicA (residues 1–165) in the pT7HMT vector (31) was accomplished as described above.

Designer gene fragments of IpaB (residues 28-226) and SipB (30-237) were designed based upon the protease stable fragments identified by limited proteolysis. Amplification via PCR from the full-length sequence confirmed plasmids of each first translocator allowed for subcloning into the pT7HMT vector. Overexpression and purification was carried out as described above. Additionally, recombinant TEV protease was used to digest the fusion affinity tag from each target protein. Final purification for $IpaB^{28.226}$ was achieved by desalting into 20 mM Ethanolamine (pH 9.0) prior to performing cation-exchange chromatography over a Resource S column (GE Biosciences). Purified $IpaB^{28.226}$ was concentrated to 5 mg/ml and exchanged into H_2O for further use. Final purification of $SipB^{30.237}$ was achieved by desalting into 20 mM Tris HCl (pH 8.0) prior to performing anion-exchange chromatography over a Resource Q column (GE Biosciences). Purified $SipB^{30.237}$ was concentrated to 10 mg/ml and buffer exchanged into 10 mM Tris (pH 7.1), 50 mM NaCl for future use.

Limited Proteolysis of TTSS Chaperone/Translocator Complexes

Limited proteolysis of IMAC-purified IpgC/IpaB and SicA/SipB complexes by subtilisin digestion at 25°C with a protein concentration of 2 mg/ml was used to generate protease stable translocator fragments. Varying enzyme:substrate ratios (by concentration) were analyzed to determine appropriate ratio for experiment (data not shown). A 1:200 ratio was identified as optimal for each translocator/chaperone complex. Over the course of 360 minutes, 5 μL aliquots were taken

every 15 minutes and boiled immediately in 4x SDS sample buffer for 10 minutes. SDS-PAGE was used to analyze the samples and protease stable products were characterized by LC-MS/MS (48).

Crystallization of Recombinant TTSS Virulence Proteins

Class II Chaperone from *S. flexneri* IpgC

IpgC$^{10-155}$ was crystallized by vapor diffusion of hanging drops at 20°C. Specifically, 1 μL of protein solution (10 mg/mL in ddH$_2$O) was mixed with 1 μL of reservoir solution containing 0.2 M magnesium chloride hexahydrate, 0.1 M Bis-Tris (pH 6.5) and 25% (w/v) PEG 3350, and the drops were equilibrated over 500 μL of reservoir solution. Clusters of needle-shaped crystals appeared overnight and continued to grow in size for approximately 7 days. Mechanical disruption of these clusters was used to obtain single, diffraction quality samples for diffraction analysis. Crystals were flash cooled in a cryoprotectant solution consisting of reservoir buffer with an additional 5% (w/v) PEG 3350. Crystals of IpgC$^{21-155}$ were also produced using an analogous approach. Briefly, 1 μL of protein solution (10 mg/mL in ddH$_2$O) was mixed with 1 μL of reservoir solution containing 0.1 M HEPES (pH 7.5) and 2.0 M ammonium formate, and the drops were equilibrated over 500 μL of reservoir solution. Single diamond shaped crystals appeared overnight and continued to grow for 2-3 days. Crystals were flash cooled in a cryoprotectant solution consisting of reservoir buffer with 30% (v/v) glycerol. Diffraction quality crystals were not obtained for full-length IpgC.

Needle Tip Protein IpaD from *S. flexneri*

Attempts to cocrystallize full length recombinant *S. flexneri* IpaD in the presence of DOC failed to yield any samples suitable for X-ray diffraction. However, unexpected in-drop proteolysis of IpaD in the presence of a molar excess of (~0.3 mM) DOC yielded single block-shaped crystals after 4 months. Optimization of the mother liquor condition resulted in large, block-shaped crystals (~300 μm in diameter). IpaD-DOC cocrystals were obtained by vapor diffusion of hanging drops at

20 °C. Specifically, 1 μl of protein solution (10 mg/ml in water) was mixed with 1 μl of reservoir solution containing 20 mM magnesium chloride hexahydrate, 100 mM HEPES (pH 7.5) and 20% (w/v) polyacrylic acid sodium salt 5100, and equilibrated over 500 μl of reservoir solution. Crystals were flash cooled in a cryoprotectant solution consisting of reservoir buffer with an additional 15% (v/v) glycerol.

<div align="center">First Translocator IpaB from S. flexneri</div>

Initial crystallization experiments for IpaB[28.226] failed to yield any samples suitable for X-ray diffraction analysis. However, adventitious proteolysis at the N-terminus of IpaB was observed over the course of several months, and subsequent rescreening using this partly degraded sample identified a condition that yielded single brick-shaped crystals in one day. Following optimization, the final crystal samples were obtained by vapor diffusion of hanging drops at 20°C where 2.5 μl of protein solution (2.5 mg/ml in H_2O) was mixed with 2.5 μl of reservoir solution (0.6 M sodium formate and 21% (w/v) PEG 2000 MME) and equilibrated over 500 μl of reservoir solution. Crystals were flash cooled in a cryoprotectant solution consisting of reservoir buffer supplemented with 15% (v/v) glycerol.

Screening for phasing atoms was accomplished by Native polyacrylamide gel electrophoresis (PAGE) of IpaB[28.226] and heavy atom mixtures (10). Single band gel shifts indicated a shift in protein charge, potentially from heavy atom derivatization. Compounds demonstrating Native PAGE shifts were chosen for further screening via in-drop soaking. Platinum derivatives were generated by adding 1 μl of K_2PtCl_4, K_2PtCl_6 and $K_2Pt(NO_2)_4$ (concentrations ranging from 0.5 mM to 20 mM) in reservoir solution to the 5 μl drop, and incubated overnight. Intact crystals were flash cooled as previously described.

First Translocator SipB from *S.* Typhimurium

Crystals of Seleno-L-Methionine-labeled SipB[30.237] failed to appear upon initial crystallization trials. However, similar to the crystallization of IpaB[28.226], adventitious degradation yielded a stable protein core. Crystals of degraded SipB[30.237] were obtained by vapor diffusion of hanging drops at 20°C. Specifically, 1.5 μl of protein solution (10 mg/ml in 10 mM Tris (pH 7.1), 50 mM NaCl) was mixed with 1.5 μl of reservoir solution containing 0.15 M potassium bromide and 27% (w/v) PEG 2000 MME, and the drops were equilibrated over 500 μl of reservoir solution. Small, blade-like microcrystals appeared within one day. Diffraction quality crystals were obtained by microseeding techniques (70), over a one week period. Crystals were flash cooled in a cryoprotectant solution consisting of reservoir buffer alone.

Diffraction Data Collection, Structure Determination, Refinement and Analysis

Class II Chaperone from *S. flexneri* IpgC

Monochromatic X-ray diffraction data (λ =1.000 Å) were collected from single IpgC[10-155] and IpgC[21-155] crystals at 100 K using beamlines 22-BM and 22-ID, respectively, of the Advanced Photon Source, Argonne National Laboratory **(Table 1)**. Following data collection, individual reflections were indexed, integrated, and scaled using HKL2000 (71). Initial phase information was obtained for the IpgC[10-155] data by maximum-likelihood molecular replacement using PHASER (58). Residues 30-151 of a single copy of the refined IpgC[1-151] structure were used as a search model (55). The single most highly scored solution contained 18 unique IpgC[10-155] polypeptides in the asymmetric unit, which corresponded to a solvent content of 56.8%.

Structure refinement was carried out using the protocols implemented in *phenix.refine* (2). First, three rounds of individual coordinate and isotropic atomic-displacement factor refinement were conducted and the refined model was used to calculate both $2F_o$-F_c and F_o-F_c maps. These maps

16

Table 1. Diffraction Data Collection and Structure Refinement Statistics - IpgC

Data Collection[a]			
Crystal		IpgC[10.155]	IpgC[21.155]
		Native	Native
Beamline		APS 22-BM	APS 22-ID
Space Group		$P2_1$	$P3_1$ or $P3_2$
Unit Cell Dimensions			
	a (Å)	140.50	86.11
	b (Å)	71.47	86.11
	c (Å)	171.01	476.27
	β (°)	93.86	
Wavelength (Å)		1.0000	1.0000
Resolution (Å)		50-3.30	50-3.40
Completeness (%)		88.5 (49.6)	89.3 (79.1)
Reflections (total)		151,044	89,308
Reflections (unique)		45,608	48,191
Redundancy (fold)		3.4x	1.9x
<I>/<σI>		14.9 (50.7)	10.0 (33.2)
R_{merge} (%)[b]		7.3 (1.4)	7.0 (1.8)

Refinement

RCSB Accession Code		3KS2

Protein Molecules/AU		18
R_{work}/R_{free} (%)[c]		25.9/29.6
Number of Atoms		
	Protein	20,070
Ramachandran Plot (%)		
	Favored	91.50
	Allowed	5.8
	Outliers	2.7
RMSD		
	Bond Lengths (Å)	0.011
	Bond Angles (°)	1.290

[a]Numbers in parentheses are for the highest-resolution shell.

[b]$R_{merge} = \Sigma_h\Sigma_i|I_i(h)\text{-}<I(h)>|/\Sigma_h\Sigma_iI_i(h)$, where $I_i(h)$ is the ith measurement of reflection h and $<I(h)>$ is a weighted mean of all measurements of h.

[c]$R = \Sigma_h|F_{obs}(h)\text{-}F_{calc}(h)|/\Sigma_h|F_{obs}|$. R_{cryst} and R_{free} were calculated from the working and test reflection sets, respectively. The test set constituted 5% of the total reflections not used in refinement.

were used to manually build residues 18-29 and 152-154 of the master polypeptide chain, which is denoted chain A in the PDB file. This intermediate model was subjected further to an identical series of refinement steps prior to a final, single round of TLS refinement in *phenix.refine*; each individual polypeptide chain was treated as its own unique TLS group. The final model displays R_{work}/R_{free} values of 25.9/29.6%, respectively, and consists of residues 18-154 for all 18 copies of $IpgC^{10-155}$ present in the asymmetric unit. RAMPAGE analysis of the final model revealed that 91.5% and 5.8% of the 2,430 residues modeled occupied either favored or allowed regions of the Ramachandran plot, respectively (77). Additional electron density that corresponded to N terminally directed residues were visible in both $2F_o$-F_c and F_o-F_c maps calculated from the final model. Side chain features were poor in these areas, however, and this precluded accurate modeling of these residues in the final structure. The coordinates of the crystal structure described here have been deposited in the RCSB database under the accession code 3KS2.

<p align="center">Needle Tip Protein IpaD from *S. flexneri*</p>

Monochromatic X-ray diffraction data were collected to 1.9 Å limiting resolution in the space group $P2_1$ from a single crystal at 100 K using beamline 22-BM of the Advanced Photon Source, Argonne National Laboratory **(Table 2)**. Following data collection, individual reflections were indexed, integrated, merged and scaled using HKL2000 (71). Initial phase information was obtained by maximum-likelihood molecular replacement using PHASER (58). Specifically, chain A of PDB entry 2J0O (wild-type *S. flexneri* IpaD) was manually truncated to residues 131-322 within PyMol (23) to reflect the likely sequence of IpaD within the cocrystal (as judged by MALDI-TOF), and this resulting structure was used as a search model. The single most highly scored solution contained an IpaD dimer in the asymmetric unit; this arrangement corresponded to a Matthews's coefficient of 2.93 $Å^3$/Da and a solvent content of 57.7%.

Table 2. Diffraction Data Collection and Structure Refinement Statistics - IpaD

Data Collection[a]		
Crystal		IpaD[122.319]/DOC Native
Beamline		APS 22-BM
Space Group		$P2_1$
Unit Cell Dimensions		
	a (Å)	62.97
	b (Å)	43.72
	c (Å)	93.757
	β (°)	97.42
Wavelength (Å)		1.0000
Resolution (Å)		25.28-1.90
Completeness (%)		97.7(82.9)
Reflections (total)		224,385
Reflections (unique)		39,374
Redundancy (fold)		5.7x
$<I>/<\sigma I>$		21.1 (2.48)
R_{merge} (%)[b]		7.2 (45.1)

Refinement	
RCSB Accession Code	3R9V
Protein Molecules/AU	2
R_{work}/R_{free} (%)[c]	22.9/25.5

Number of Atoms

	Protein	2826
	Ligand	56
	Solvent	244

Ramachandran Plot (%)

	Favored	96.6
	Allowed	2.3
	Outliers	1.1

RMSD

	Bond Lengths (Å)	0.010
	Bond Angles (°)	1.186

B factor (Å^2)

	Protein	38.0
	Ligand	37.4
	Solvent	38.8

Ligand Occupancy (%)

	Chain A	0.95
	Chain B	0.96

[a]Numbers in parentheses are for the highest-resolution shell.

[b]$R_{merge} = \Sigma_h\Sigma_i|I_i(h)-<I(h)>|/\Sigma_h\Sigma_iI_i(h)$, where $I_i(h)$ is the ith measurement of reflection h and $<I(h)>$ is a weighted mean of all measurements of h.

[c]$R = \Sigma_h|F_{obs}(h)-F_{calc}(h)|/\Sigma_h|F_{obs}|$. R_{cryst} and R_{free} were calculated from the working and test reflection sets, respectively. The test set constituted 5% of the total reflections not used in refinement.

Structure refinement was carried out using the protocols implemented in *phenix.refine* (2). One round of simulated annealing, individual coordinate and isotropic atomic-displacement factor refinement was conducted, and the refined model was used to calculate both $2F_o$-F_c and F_o-F_c difference maps. These maps were used to iteratively improve the model by manual building in Coot (26, 27), followed by additional coordinate and atomic-displacement factor refinement. Ordered solvent molecules were added according to the default criteria of *phenix.refine*, and inspected manually using Coot prior to model completion. Additional information and refinement statistics are presented in **Table 2.** Chain A contains an intact polypeptide encompassing residues 122-319, while regions of poor map quality between residues 174-194 and 270-278 within chain B prevented complete coverage from residues 124-318.

<center>First Translocator IpaB from *S. flexneri*</center>

Monochromatic X-ray diffraction data (λ=1.000 Å) were collected from single native IpaB[28.226] crystals at 100 K using beamline 22-BM of the Advanced Photon Source, Argonne National Laboratory. Heavy atom soaked IpaB[28.226] crystals were exposed to X-rays of wavelengths corresponding to Pt peak and remote edges 1.07197Å and 1.0000Å) at beamline 22-BM (**Table 3**). Following data collection, individual reflections were indexed, integrated, and scaled using HKL2000 (71). Experimental phase information was obtained from the anomalous and dispersive differences in the K_2PtCl_4-derivatized IpaB[28.226] dataset by AutoSol within the *phenix.refine* suite (2), which identified two Pt heavy-atom sites within the asymmetric unit. Iterative model building into the experimental electron-density map was carried out within AutoBuild of the *phenix.refine* suite in the space group $P2_1$. One round of individual coordinate and isotropic atomic-displacement factor refinement were conducted, and the refined model was used to calculate both $2F_o$-F_c and F_o-F_c difference maps. These maps were used to iteratively improve the experimental model by manual

<center>22</center>

Table 3. Diffraction Data Collection and Structure Refinement Statistics – IpaB/SipB

Data Collection[a]

Crystal		IpaB[28.226]	IpaB[28.226]	IpaB[28.226]	SipB[30.237]	SipB[30.237]
		Native	Pt Remote	Pt Peak	SeMet Remote	SeMet Peak
Beamline		APS 22-BM	APS 22-BM	APS 22-BM	APS 22-BM	APS 22-BM
Space Group		$P2_1$	$P2_1$	$P2_1$	$P2_12_12$	$P2_12_12$
Unit Cell Dimensions						
	a (Å)	52.391	52.300	52.300	51.144	51.052
	b (Å)	28.372	28.060	28.060	84.646	84.715
	c (Å)	104.804	104.760	104.760	159.155	159.336
	β (°)	95.966	95.920	95.920		
Wavelength (Å)		1.0000	1.0000	1.0719	0.9724	0.9793
Resolution (Å)		50-2.1	50-2.5	50-2.5	50-2.8	50-3.0
Completeness (%)		91.7 (59.3)	95.7 (72.0)	97.2 (80.5)	98.0 (87.2)	99.2 (95.5)
Reflections (total)		61,832	68,016	71,247	209,952	86,789
Reflections (unique)		18,186	10,464	10,634	17,478	14,590
Redundancy (fold)		3.4x	6.5x	6.7x	12.0x	5.9x
$<I>/<\sigma I>$		13.4 (2.0)	18.6 (2.82)	19.4 (3.6)	18.8 (2.55)	14.3 (2.05)
R_{merge} (%)[b]		8.5 (42.5)	8.4 (35.0)	8.2 (27.8)	10.0 (67.1)	11.5 (61.1)

Refinement

RCSB Accession Code		3U0C			3TUL	

Protein Molecules/AU	2	4
$R_{\text{work}}/R_{\text{free}}$ (%)^{c}	24.53/29.45	29.73/31.67
Number of Atoms		
Protein	2426	3877
Solvent	88	43
Ramachandran Plot (%)		
Favored	97.7	95.7
Allowed	0.6	4.0
Outliers	1.7	0.2
RMSD		
Bond Lengths (Å)	0.008	0.009
Bond Angles (°)	1.066	1.240
B factor (Å^2)		
Protein	44.76	52.56
Solvent	50.60	58.10

^{a}Numbers in parentheses are for the highest-resolution shell.

$^{b}R_{\text{merge}} = \Sigma_h\Sigma_i|I_i(h)\text{-}<I(h)>|/\Sigma_h\Sigma_iI_i(h)$, where $I_i(h)$ is the ith measurement of reflection h and $<I(h)>$ is a weighted mean of all measurements of h.

$^{c}R = \Sigma_h|F_{\text{obs}}(h)\text{-}F_{\text{calc}}(h)|/\Sigma_h|F_{\text{obs}}|$. R_{cryst} and R_{free} were calculated from the working and test reflection sets, respectively. The test set constituted 5% of the total reflections not used in refinement.

building in Coot (26, 27), followed by additional coordinate and atom-displacement factor refinement.

The refined experimental model was used to obtain initial phase information for the high resolution, native IpaB[28.226] structure by maximum-likelihood molecular replacement using PHASER (58). The single most highly scored solution within the space group $P2_1$ contained a model for two IpaB polypeptides. This arrangement corresponded to a Matthews coefficient of 2.28 Å³/Da and a solvent content of 46%. Electron density corresponding to residues 74-224 of IpaB was modeled for both chains within the $P2_1$ space group structure. Additional information and refinement statistics for all three structures is presented in **Table 3**. The coordinates of the crystal structure described here has been deposited in the RCSB database (51) under the accession code 3U0C.

<center>First Translocator SipB from S. Typhimurium</center>

X-ray diffraction data were collected at wavelengths corresponding to Se remote (λ=0.97243 Å), peak (λ=0.97934 Å) and edge (λ=0.97949 Å) wavelengths from a single SeMet-labeled SipB[30.237] crystal at 100 K using beamline 22-BM of the Advanced Photon Source, Argonne National Laboratory (**Table 3**). Following data reduction experimental phase information was obtained from the anomalous and dispersive differences within the SeMet-labeled SipB[30.237] dataset by AutoSol within the *phenix.refine* suite (2), which identified the positions of twelve Se-atom sites within the asymmetric unit. One round of individual coordinate and isotropic atomic-displacement factor refinement were conducted upon the initial automated model built by AutoSol (2), and the refined model was used to calculate both $2F_o$-F_c and F_o-F_c difference maps. These maps were used to iteratively improve the experimental model by manual building in Coot (26, 27), followed by additional coordinate and atom-displacement factor refinement. Side chains were modeled according to the SipB sequence using SeMet sites as a guide. Ordered solvent molecules were added according to the default criteria of *phenix.refine*, and inspected manually using Coot prior to model completion.

Analysis of the asymmetric unit revealed four SipB polypeptides within the space group $P2_122_1$ with a Matthews coefficient of 2.53 $\text{Å}^3/\text{Da}$ and a solvent content of 54%. Electron density corresponding to residues 82 – 122, 126 – 174 and 182 - 226 of SipB were modeled in at least one polypeptide chain. Crystal packing placed the loops connecting each alpha helix in solvent channels, and along with the inherent flexibility of these regions, prevented accurate modeling. Additional information and refinement statistics for the structure is presented in **Table 3**. The coordinates of the crystal structure described here have been deposited in the RCSB database (51) under the accession codes 3TUL.

Ligand Fitting of Deoxycholate

Modeling for the DOC ligand was accomplished using the PRODRG server (87), and restraint files were generated using *phenix.elbow* (2). Inspection of the initial F_o-F_c difference maps described above revealed unmodeled contiguous density that corresponded to ordered ligand near the N-terminus (α3 and α7) of both copies of IpaD found within the asymmetric unit. *Phenix.ligandfit* (2) was subsequently used to fit and model a single DOC molecule per IpaD monomer. Refinement of the ligand-bound IpaD structure was carried out as described above, with the exception that constrained group occupancy refinement was used to estimate the fraction of ligand bound at each site independently.

Analytical Gel Filtration Chromatography of IpgC

Purified protein samples (5 mg/mL) were separated on a Tricorn Superdex 200 10/300 analytical gel filtration chromatography column (GE Biosciences) that had been previously equilibrated in a buffer of 20 mM Tris-HCl (pH 8.0), 200 mM NaCl, 1 mM DTT at 4 °C. Estimates of molecular weight and oligomerization were made by comparing the retention time of individual samples to those of globular protein standards (Bio-Rad).

Chemical Crosslinking of IpgC

Bis(Sulfosuccinimidyl) suberate (BS^3; 80 μL of a 250 μM solution in ddH$_2$O) was added to 20 μL samples (2 mg/mL) of purified IpgC$^{1-151}$ and IpgC$^{10-155}$ at 20 °C. 5 μL aliquots from each reaction were withdrawn at various time points over the course of 240 min and excess BS^3 was quenched by adding 0.75 μL of 25 mM Tris (pH 8.0) for 30 min. Samples were analyzed under reducing conditions by electrophoresis (10% SDS-PAGE) using a Tris-Tricine buffer system.

Copurification Assay for Class II Chaperone Activity

Chaperone activity of full-length IpgC and various deletion proteins was monitored by chromatographic copurification. Specifically, a designer gene fragment encoding a protease-stable domain of *S. flexneri* IpaB (residues 58-357; denoted IpaB$^{58-357}$) was generated by PCR, subcloned in the expression vector pACYC-Duet (Novagen), and sequenced; this vector provides for expression of IpaB$^{58-357}$ without any fusion tag, and IpaB does not bind significantly to Ni^{2+}-NTA Sepharose on its own accord (72). The resulting plasmid was co-transformed with various pT7HMT-IpgC expression vectors (described above) into *E. coli* BL21 (DE3) cells. Cotransformants were identified by antibiotic selection with both chloramphenicol and kanamycin. Cells harboring both expression vectors were cultured and protein expression was induced according to standard methods. Homogenates of induced cells (250 mL total culture volume) were prepared by microfluidization, clarified by centrifugation, and subjected to Ni^{2+}-NTA Sepharose chromatography as described above. Following this, the crude eluate was further separated on a Superdex 75 26/60 preparative gel-filtration column (GE Biosciences). Samples were analyzed under reducing conditions by 4-10% gradient SDS-PAGE using a Tris-Tricine buffer system.

Materials for IpaD Assays

The *S. flexneri ipaD* null strain (SF622) was from P.J. Sansonetti (Institute Pasteur, Paris, France). Antibodies against IpaB, IpaC and IpaD were provided by E.V. Oaks (Walter Reed Army Institute for Research, Silver Spring MD). Alexa-fluor labeled secondary antibodies were from

Invitrogen. *E.coli* Nova Blue cells and ligation reagents were from Novagen (Madison, WI).

Restriction enzymes were from New England Biolabs (Tozer, MA). Oligonucleotide primers were

from IDT (Coralville, IA). All other chemicals were reagent grade.

Bacterial Strains for IpaD Assays

The strains used in this study are listed in **Table 4**. All *ipaD* mutants were constructed by

inverse PCR using pWPsf4D (which contains a copy of the wild-type *ipaD* gene (75)) as a template

and primers incorporating the desired mutation. The resulting linear plasmid was digested with *Nde*I,

intramolecularly ligated, and introduced into the *E.coli* Nova blue cells by transformation. Each

plasmid was subsequently purified and introduced by electroporation into *S. flexneri* SF622.

Ampicillin selection ensured the presence of the recombinant plasmid while kanamycin resistance

and/or Congo red binding were used to ensure the presence of *S. flexneri* virulence plasmid.

Overnight Ipa Protein Secretion

Shigella were grown overnight at 37°C with aeration in tryptic soy broth (TSB). The bacteria

were then removed by centrifugation at 6000 × *g* and the proteins in the culture supernatant were

precipitated by bringing the solution to 10% (w/v) with trichloroacetic acid and incubating at 4°C.

The precipitated protein was collected by centrifugation at 10,000 × *g* for 10 min and the resulting

pellet washed with ice-cold acetone prior to resuspending in 10mM sodium phosphate (pH 7.2)

containing 150mM NaCl (PBS). Two volumes of SDS-sample buffer were then added and the

proteins were separated by SDS-polyacrylamide gel electrophoresis (SDS-PAGE). The proteins were

then transferred to nitrocellulose for routine immunoblot analysis using a mixture of antibodies

against IpaB, IpaC, and IpaD. Proteins were detected using Alexa Fluor 680-labeled goat anti-rabbit

IgG. Western blot images were obtained using an Odyssey Infrared Imaging System (LI-COR,

Lincoln, NE).

Table 4. Bacterial Strains Used in the Study

Strain designation	Resistance
Shigella flexneri ipaD null (SF622)	Kan
SF622 harboring pWPsf4D[a]	Amp/Kan
L134S[b]	Amp, Kan
L134E	Amp, Kan
K137S	Amp, Kan
I138S	Amp, Kan
L315S	Amp, Kan
L315E	Amp, Kan
L134S/L315S	Amp, Kan
L134E/L315E	Amp, Kan

[a]pWPsf4D contains the wild-type *ipaD* gene for expression in *S. flexneri*.

[b]Each mutant designation is for IpaD harboring the designated amino acid change encoded on pWPsf4.

Bacterial Invasion of Cultured Epithelial Cells and Contact-mediated Hemolysis

S. flexneri invasion of HeLa cells was monitored with a gentamycin protection assay as previously described (75). HeLa cells were seeded into 24-well plates and grown overnight in MEM supplemented with 10% calf serum (containing penicillin and streptomycin) at 37 ^{o}C, 5% (v/v) CO_2, and a relative humidity of 100%. *S. flexneri* was then grown on trypic soy agar plates containing 0.025% (w/v) Congo red. Ampicillin was included on plates for growing bacteria harboring the pWPsf4 plasmid to maintain the plasmid. Red colonies (indicative of bacteria that had not lost the *Shigella* virulence plasmid) were used to inoculate 10 ml of TSB containing kanamycin (to maintain the virulence plasmid if the bacteria were derived from SF622) and ampicillin (to ensure maintenance of the pWPsf4 plasmid). The bacteria were grown at 37°C to early log phase ($A_{600} \sim 0.4$) with aeration. The cultures were then split so that half could be incubated for the final 30 min in the presence of 2.5 mM (0.1% w/v) deoxycholate (DOC). The bacteria were then incubated with the HeLa cells for 30 min as described (75) without the centrifugation step. Extracellular bacteria were killed with 50 µg/ml gentamycin. The invading bacteria were visualized by overlaying the HeLa cell monolayers with 1.0% agarose in water, followed by an overlay of 2× LB media in agar. After overnight incubation at 37 ^{o}C, the colonies were counted and the relative level of invasion for bacteria making mutant IpaD was compared to that of *S. flexneri* SF622 harboring pWPsf4D which expressed wild-type IpaD.

Shigella contact-mediated hemolysis was initially measured as described previously (75). Because this method essentially results in 100% lysis of the erythrocytes, it was modified by reducing the number of bacteria incubated with the epithelial cells and shortening the incubation time. This allowed us to obtain subsaturating levels of contact-mediated hemolysis which could be used to detect subtle differences in contact-mediated hemolysis caused by *Shigella* expressing different mutant forms of IpaD. Briefly, bacteria were grown to mid-log phase, collected by centrifugation and

resuspended in PBS. Sheep red blood cells were washed and resuspended in PBS to a concentration

of 10^{10}/ml. Blood cells and bacteria were mixed and forced into contact by centrifuging at 2,200 × g

for 15 min at 20°C. The cells were then incubated at 37°C for 30 min, resuspended in cold PBS and

centrifuged again at 2,200 × g. The amount of hemolysis was then measured by determining the

absorbance of the resulting supernatant fraction at 545 nm. The data are presented as a percent of

total lysis which was determined by incubating the erythrocytes in water. Incubation in PBS served

as a negative control for hemolysis.

Surface Localization of IpaD

To visualize the presence of IpaD at the tip of the *S. flexneri* TTSA needle, bacteria were first

grown to early log phase (A_{600} ~0.4) in TSB with or without 2.5 mM DOC. The bacteria were then

collected by centrifugation, resuspended in PBS, and fixed with 1.5% (v/v) formaldehyde. The

bacteria were affixed to glass slides and blocked with 1% (w/v) bovine serum albumin in

PBS:Odyssey buffer (1:1). IpaD was detected using rabbit anti-IpaD antiserum as the primary

antibody and Alexa Fluor 488 goat anti-rabbit IgG as the secondary antibody. Fluorescence

microscopy was the carried out using an Olympus IX-81 spinning disk confocal microscope using a

mercury light source with the appropriate bandpass filters to excite the fluorophore. In multiple fields

(n ≥10), the number of bacteria with IpaD on their surface was determined as a function of total

bacteria in the field. In some cases where the bacteria were found to have elevated invasion levels in

the absence of DOC, they were examined for the presence of IpaB on their surfaces prior to DOC-

induced maturation.

Miscellaneous

Multiple sequence alignments were carried out using CLUSTALW (93) and aligned with

secondary structure elements using ESPRIPT (33). Class II chaperone sequences used in alignment,

along with their respect accession numbers, were as follows: *Shigella flexneri* IpgC (GI:32307022),

Burkholderia pseudomallei BicA (GI:126447932), *Salmonella enterica* serovar Typhimurium SicA (GI:975294), *Pseudomonas aeruginosa* PcrH (GI: 29826004) and *Yersinia enterocolitica* SycD (GI:23630571). First translocator sequences used in alignment, along with their respective GenBank accession numbers, were as follows: *Shigella flexneri* (GI:281603883), *Burkholderia pseudomallei* (GI:127950892), *Salmonella enterica* serovar Typhimurium (GI:975295), and Enteroinvasive *Escherichia coli* (GI:22022402). Three-dimensional structures were analyzed using the Protein Interfaces, Surfaces, and Assemblies server (PISA) (51) and superimposed using the Local-Global Alignment method (LGA) (101). Representations of all structures were generated using PyMol (23). Calculations of electrostatic potentials at the molecular surface were carried out using DELPHI (80). The DALI server was used to query available structures within the PDB for structural homology (40).

CHAPTER 3

EVIDENCE FOR ALTERNATIVE QUATERNARY STRUCTURE IN A BACTERIAL TYPE III SECRETION SYSTEM CHAPERONE

Overview

Type III secretion systems are a common virulence mechanism in many Gram-negative bacterial pathogens. These systems use a nanomachine resembling a molecular needle and syringe to provide an energized conduit for the translocation of effector proteins from the bacterial cytoplasm to the host cell cytoplasm for the benefit of the pathogen. Prior to translocation specialized chaperones maintain proper effector protein conformation. The class II chaperone, Invasion plasmid gene C (IpgC), stabilizes two pore forming translocator proteins, IpaB and IpaC. IpgC exists as a functional dimer to facilitate the mutually exclusive binding of both translocators. In this study, we present the 3.3 A crystal structure of an amino-terminally truncated form (residues 10-155, denoted IpgC$^{10-155}$) of the class II chaperone IpgC from *Shigella flexneri*. Our structure demonstrates an alternative quaternary arrangement to that previously described for a carboxy-terminally truncated variant of IpgC (IpgC$^{1-151}$).

Specifically, we observe a rotationally-symmetric "head-to- head" dimerization interface that is far more similar to that previously described for SycD from *Yersinia enterocolitica* than to IpgC$^{1-151}$. The IpgC structure presented here displays major differences in the amino terminal region, where extended coil-like structures are seen, as opposed to the short, ordered alpha helices and asymmetric dimerization interface seen within IpgC$^{1-151}$. Despite these differences, however, both modes of dimerization support chaperone activity, as judged by a copurification assay with a recombinant form of the translocator protein, IpaB.

Crystallization and Structure Determination of an Amino-terminally Truncated form of IpgC

Limited subtilisin treatment of recombinant, full-length IpgC was used to generate protease stable fragments of the *Shigella* chaperone that were characterized by LC-MS/MS (48). Two predominant products were identified that corresponded to loss of nine (IpgC$^{10-155}$) and twenty (IpgC$^{21-155}$) residues, respectively, from the amino terminus of IpgC (unpublished results). Recombinant forms of both proteins were overexpressed, purified, and crystallized by hanging-drop vapor diffusion. X-ray diffraction data were collected from both crystal systems as described in **Table 1**. While both crystals diffracted X-rays to moderate resolution, the IpgC$^{21-155}$ crystals displayed very large cell parameters and were not pursued further. Initial attempts to solve the IpgC$^{10-155}$ crystal by molecular replacement all failed when either (a) the complete IpgC$^{1-151}$dimer, (b) residues 10-151 from either monomer of the IpgC$^{1-151}$ structure, or (c) residues 20-151 from either monomer of the IpgC$^{1-151}$ structure were used as a search model. In contrast, iterative rounds of likelihood-based molecular replacement using a search model of residues 30-151 of a single IpgC$^{1-151}$ polypeptide chain eventually provided sufficient information to identify all 18 copies of the IpgC$^{10-155}$ protein present. Given the complexity of the asymmetric unit, and the resolution limits of the diffraction data available, a complete set of 17 strict non-crystallographic symmetry operators was used in all steps of model building and refinement. This resulted in the completed structure (**Figure 4A, B** and **Table 1**) with R$_{work}$ and R$_{free}$ values of 25.9% and 29.6%, respectively.

Evidence for Alternative Quaternary Structures in IpgC

As was expected from the absolute level of sequence identity between the IpgC$^{10-155}$ structure presented here and either IpgC$^{1-151}$ monomer described by Lunelli *et al.* (55), the IpgC polypeptide monomers superimpose well with one another (**Figure 5A, B** and **Table 5**). The only noteworthy difference between these structures lies in the amino terminal regions (i.e. residues 1-30) of these two forms of IpgC. Whereas these residues in IpgC$^{1-151}$ form two short, ordered alpha helices (55), the
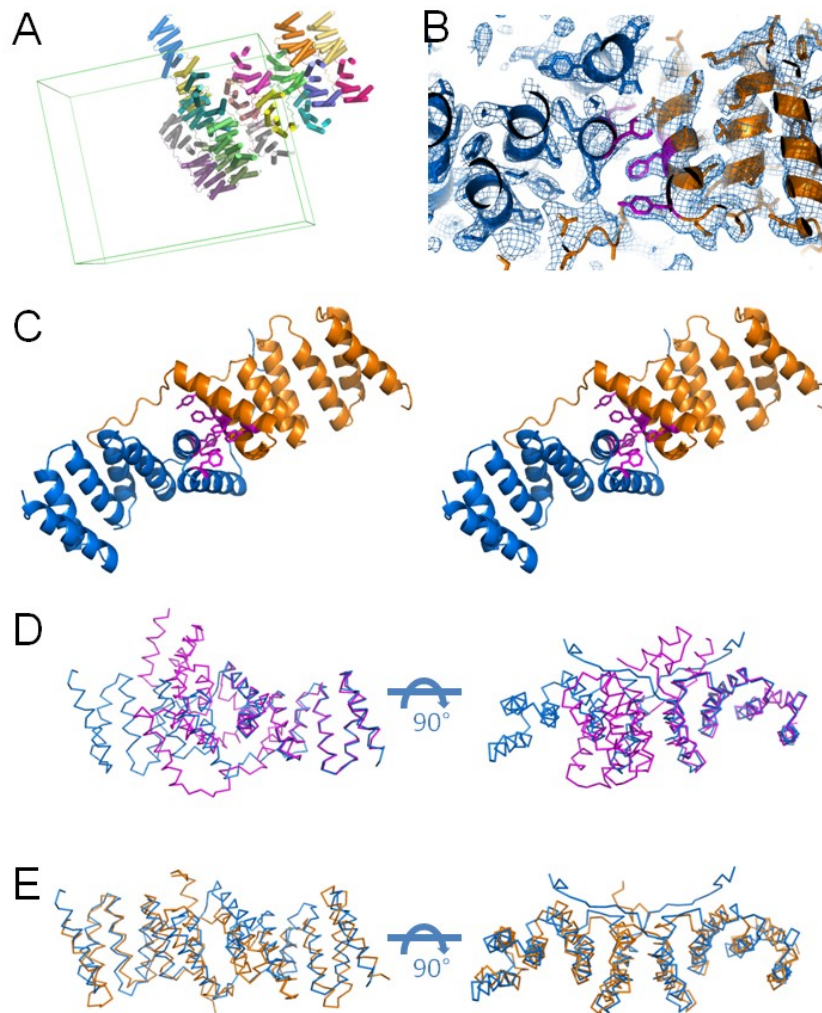
FIGURE 4. The 3.3 Å Crystal Structure of IpgC$^{10\text{-}155}$ Reveals a SycD-like Dimerization Interface. *A*, Refined asymmetric unit of the IpgC$^{10\text{-}155}$ crystal. The 18 distinct polypeptides are colored individually; helices are depicted as cylinders for clarity. The boundaries of the primitive monoclinic cell are shown as a green box. *B*, Representative model-to-map correlation for an IpgC$^{10\text{-}155}$ dimer pair; note that this same pair is colored identically to and further analyzed in panel C. 2Fo-Fc weighted electron density (contoured at 1.2 σ) is drawn as a blue cage. *C*, Detailed stereoscopic view of the dimerization interface observed in IpgC$^{10\text{-}155}$. The two monomers are colored in blue and orange, respectively, while the intercalated network of aromatic sidechains is shown in magenta. *D*, Orthogonal views of superposition by Local-Global Alignment for the proposed IpgC$^{1\text{-}151}$ dimer (magenta) (55) with that of IpgC$^{10\text{-}155}$ (blue). (E) Orthogonal views of superposition by Local-Global Alignment for the proposed SycD$^{21\text{-}163}$ dimer (orange) (13) with that of IpgC$^{10\text{-}155}$ (blue) dimer structure. Additional quantitative descriptions of the quality of the superpositions shown in panels D and E may be found in **Table 5**.

35

same region of IpgC[10-155] adopts an extended coil-like structure. This significant structural difference provides the most likely explanation for why molecular replacement searches with either IpgC[1-151] dimers or models with insufficiently truncated amino termini failed. Separately, quantitative comparisons of structure superposition (101) between IpgC[10-155] and SycD[21-163] reveal that the corresponding monomer structures are nearly as similar to one another as are the two forms of IpgC (**Figure 5C** and **Table 5**). While this is somewhat surprising given the limited sequence identity (~26%) between these proteins, it further underscores the high level of tertiary structure conservation among TTSS class II chaperones.

Examination of the refined structure indicates that the IpgC[10-155] crystals consist of an ordered lattice of protein dimers. However, much like the structures of SycD[21-163] (13), IpgC[1-151] (55), and PcrH[21-160] (44), more than one plausible dimerization arrangement are observed. The first class of dimer is present in nine crystallographically unique copies and is characterized by a "head-to-head" orientation, where each monomer is related by a single axis of rotational symmetry (**Figure 4C** and **Figure 6**). This "head-to-head" dimer buries an average of 1262.5 Å^2 of surface area upon formation, which compares favorably to the 1381.9 Å^2 interface previously described for IpgC[1-151] (55). A distinct class of rotationally-symmetric arrangement occurs only once within the asymmetric unit, though it can be generated for all other IpgC[10-155] chains by application of crystallographic operators (**Figure 7**). It is worth noting, however, that this "tail-to-tail" dimer buries only an average of 756.5 Å^2 upon formation, or approximately 60% of the surface masked by the "head-to-head" structure. Furthermore, the contacts present in the "head-to-head" dimer are more extensive and conserved to a

Table 5. Superposition Analysis for Selected Monomers and Dimers as Determined

by Local-Global Alignment

Structure 1	Structure 2	Corresponding Cα positions[a]	RMSD (Å)	Sequence Identity (%)	LGA_S[c]
IpgC$^{1-151}$ (chain A)	IpgC$^{10-155}$	122/137	0.80	99.18[b]	88.32
IpgC$^{1-151}$ (chain B)	IpgC$^{10-155}$	123/137	1.01	100.00	87.62
SycD$^{21-163}$ (chain A)	IpgC$^{10-155}$	120/137	1.56	25.83	80.61
SycD$^{21-163}$ (AU)	IpgC$^{10-155}$ (chains A&B)	199/274	2.34	18.59	51.27
IpgC$^{1-151}$ (AU)	IpgC$^{10-155}$ (chains A&B)	135/274	1.35	93.33	48.14

[a] Denotes the number of residues from structure 1 that superimpose within 4.0 Å distance of an equivalent position in structure 2.

[b] Even though the actual sequence identity between these two samples is 100%, the Cα location of A30 in chain of A of the IpgC$^{1-151}$ structure actually lies closer to that of I28 of IpgC$^{10-155}$ when these two structures are superimposed.

[c] The LGA_S parameter represents a scoring function to evaluate the overall levels of structural similarity between two sets of coordinates. For each set of corresponding residues, it combines information pertaining to both the faction of residues that overlap within a given RMSD window as well as those that overlap within a given distance cutoff (101).
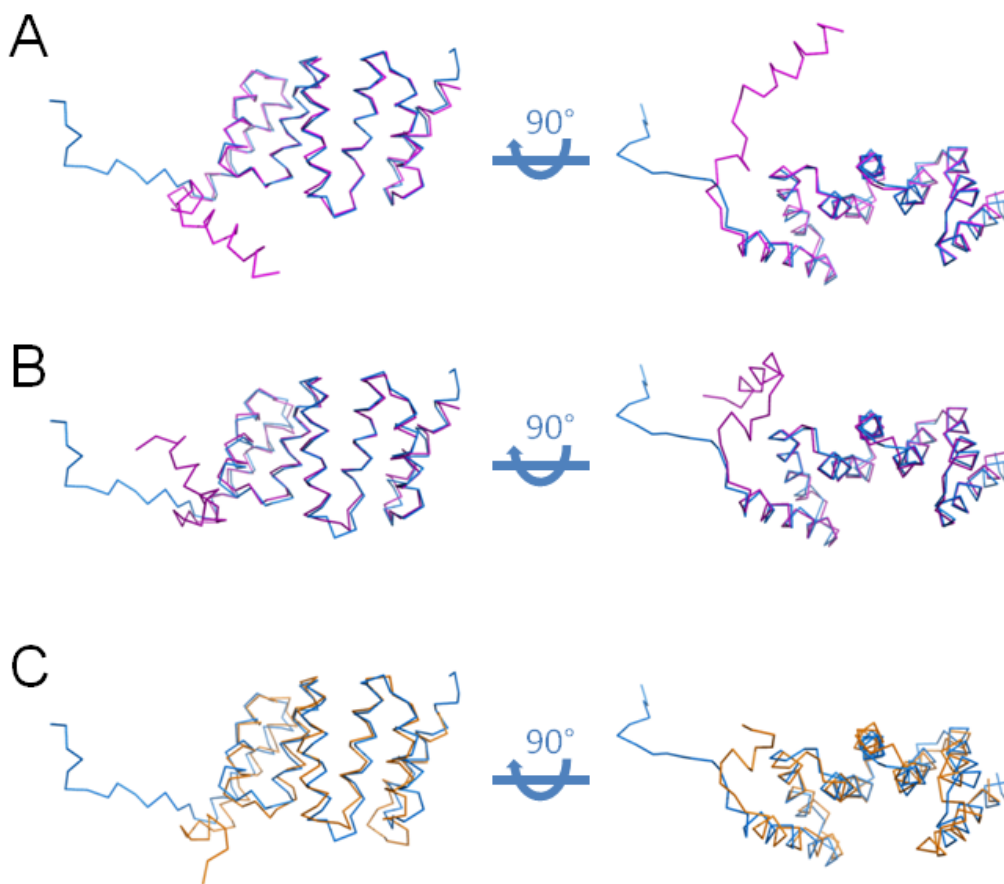
FIGURE 5. Superposition of Monomers from Class II Chaperone Structures. *A*, Orthogonal views of superposition by Local-Global Alignment for the IpgC$^{10-155}$ monomer (blue) with chain A from the published structure of IpgC$^{1-151}$ (magenta) (55). *B*, Orthogonal views of superposition by Local-Global Alignment for the IpgC$^{10-155}$ monomer (blue) with chain B from the published structure of IpgC$^{1-151}$ (magenta) (55). *C*, Orthogonal views of superposition by Local-Global Alignment for the IpgC$^{10-155}$ monomer (blue) with chain A of the published structure of SycD$^{21-163}$ (orange) (13). Additional quantitative descriptions of the quality of each superposition may be found in **Table 5**.

A Superposition of NCS-related Dimer Pairs in the IpgC$^{10\text{-}155}$ Structure

90°

AB: green	GH: yellow	MN: blue
CD: light blue	IJ: pink	OP: orange
EF: purple	KL: white	QR: light green
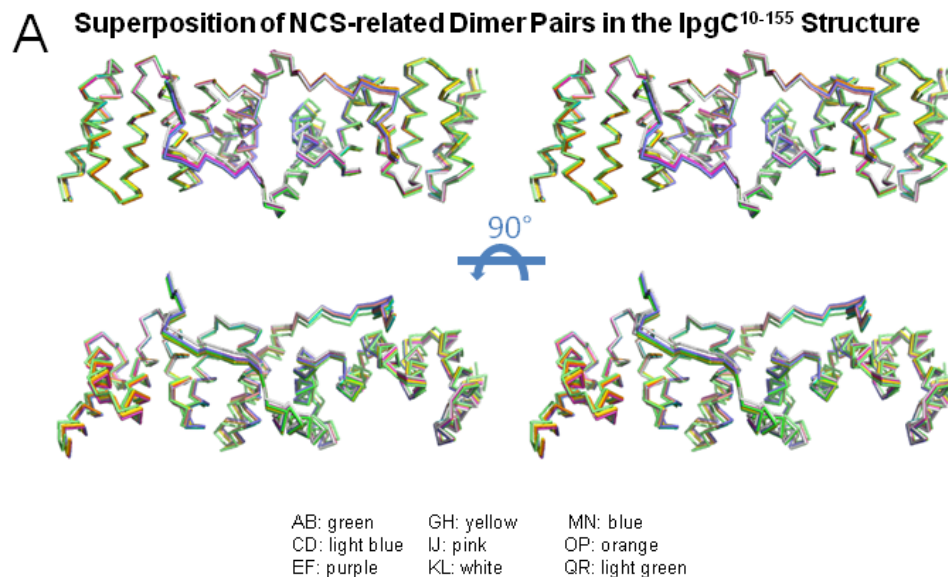
B Superposition Analysis for all Dimer Pairs in the IpgC$^{10\text{-}155}$ Structure as Determined by Local-Global Alignment[a]

Dimer Set 1	Dimer Set 2	RMSD (Å)	LGA_S[b]
AB	CD	0.22	100.00[b]
AB	EF	0.35	100.00
AB	GH	0.52	99.83
AB	IJ	0.25	100.00
AB	KL	0.56	99.71
AB	MN	0.35	100.00
AB	OP	0.42	99.97
AB	QR	1.28	94.74

[a] Sequence identity was 100% over corresponding 274 corresponding Cα positions. Only residue positions from Dimer Set 2 that superimpose within 4.0 Å distance of an equivalent position in Dimer Set 1 are included in RMSD calculations.

[b] The LGA_S parameter represents a scoring function to evaluate the overall levels of structural similarity between two sets of coordinates. For each set of corresponding residues, it combines information pertaining to both the faction of residues that overlap within a given RMSD window as well as those that overlap within a given distance cutoff[10].

FIGURE 6. Analysis of All Dimer Pairs Found in the IpgC$^{10\text{-}155}$ Asymmetric Unit. All nine IpgC$^{10\text{-}155}$ dimer pairs were superimposed by Local-Global Alignment to examine their overall similarity to one another. *A,* Two orthogonal stereoscopic views of each dimer pair superimposed. A legend describing the identity of each protein chain in the corresponding PDB entry (accession code 3KS2) is shown underneath. *B,* Quantitative analysis of all dimer superpositions from **panel A** presented in Table format

39
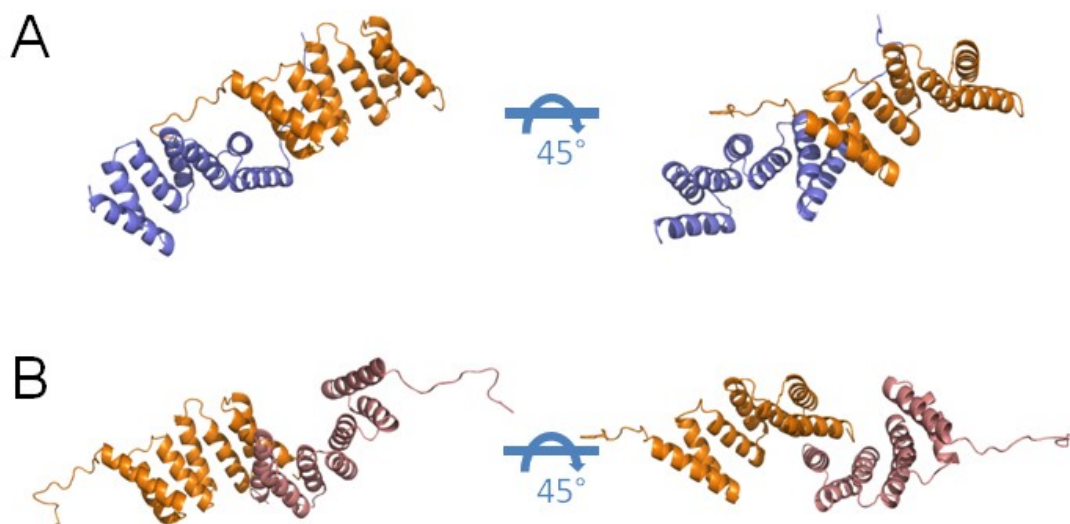
FIGURE 7. Superposition Comparison of Alternative Dimer Assemblies in the IpgC[10-155] Crystal. Potential contacts between either non-crystallographic or crystallographic symmetry-related IpgC[10-155] chains were evaluated using the EBI Protein Interfaces Surfaces and Assemblies (PISA) server (51). *A*, Two views of the rotationally-symmetric "head-to-head" dimer (as shown in Figure 4B, C) that is found in nine copies within the IpgC[10-155] asymmetric unit. On average, this arrangement buries 1262.5 Å^2 of surface area upon formation. *B*, Two views of a rotationally-symmetric "tail-to-tail" dimer found in nine copies following application of crystallographic symmetry operators. On average, this arrangement buries 756.5 Å^2 of surface area upon formation. For the sake of clarity, the relative orientation of the orange colored IpgC[10-155] chain is identical between panels A and B.

far greater extent (21 of 40 residues, or roughly 53%) than are those found in the "tail-to-tail" structure (6 of 18 residues, or roughly 33%). When considered together, these data strongly suggest that the "head-to-head" dimer is the relevant structure for IpgC[10-155], and that the other dimerization mode most likely arises from crystallization.

The identification of a rotationally symmetric dimer within the IpgC[10-155] crystal raised questions about its relationship to the dimers previously described for TTSS class II chaperones (**Figure 4D, E** and **Table 5**). In this regard, the "head-to-head" arrangement of IpgC[10-155] superimposes relatively poorly with the asymmetric dimer of IpgC[1-151]; overall, only 135 of 274 corresponding Cα positions lie within 4.0 Å distance and an RMSD of 1.35 Å. By contrast, the IpgC[10-155] dimer overlays surprisingly well with the dimer previously described for SycD[21-163]; here, 199 of 274 corresponding Cα positions lie within 4.0 Å distance with an RMSD of 2.34 Å. It is important to note that the lower RMSD for the first superposition arises because Cα positions that lie outside of the 4.0 Å distance cutoff are omitted from RMSD calculation. Thus, even though the two IpgC structures share a substantially higher level of identity in terms of sequence and overall monomer structure (**Figure 5** and **Table 5**), the far greater number of aligned residues between the IpgC[10-155] and SycD[21-163] dimers indicates that their "head-to-head" quaternary structures are closely related.

Although the biological unit of the IpgC[1-151] structure has been defined as an asymmetric dimer of structurally unique subunits, examination of IpgC[1-151] chains related by crystallographic symmetry reveals two separate contacts reminiscent of the IpgC[10-155] quaternary structure (**Figure 8**). The first of these contacts is found in the IpaB peptide-bound form of IpgC[1-151], and buries 666.9 Å^2 of surface area upon formation (**Figure 8A**). When compared carefully to the IpgC[10-155] dimer, it is apparent that the symmetry-related IpgC[1-151] chain in this contact is rotated to a greater extent relative
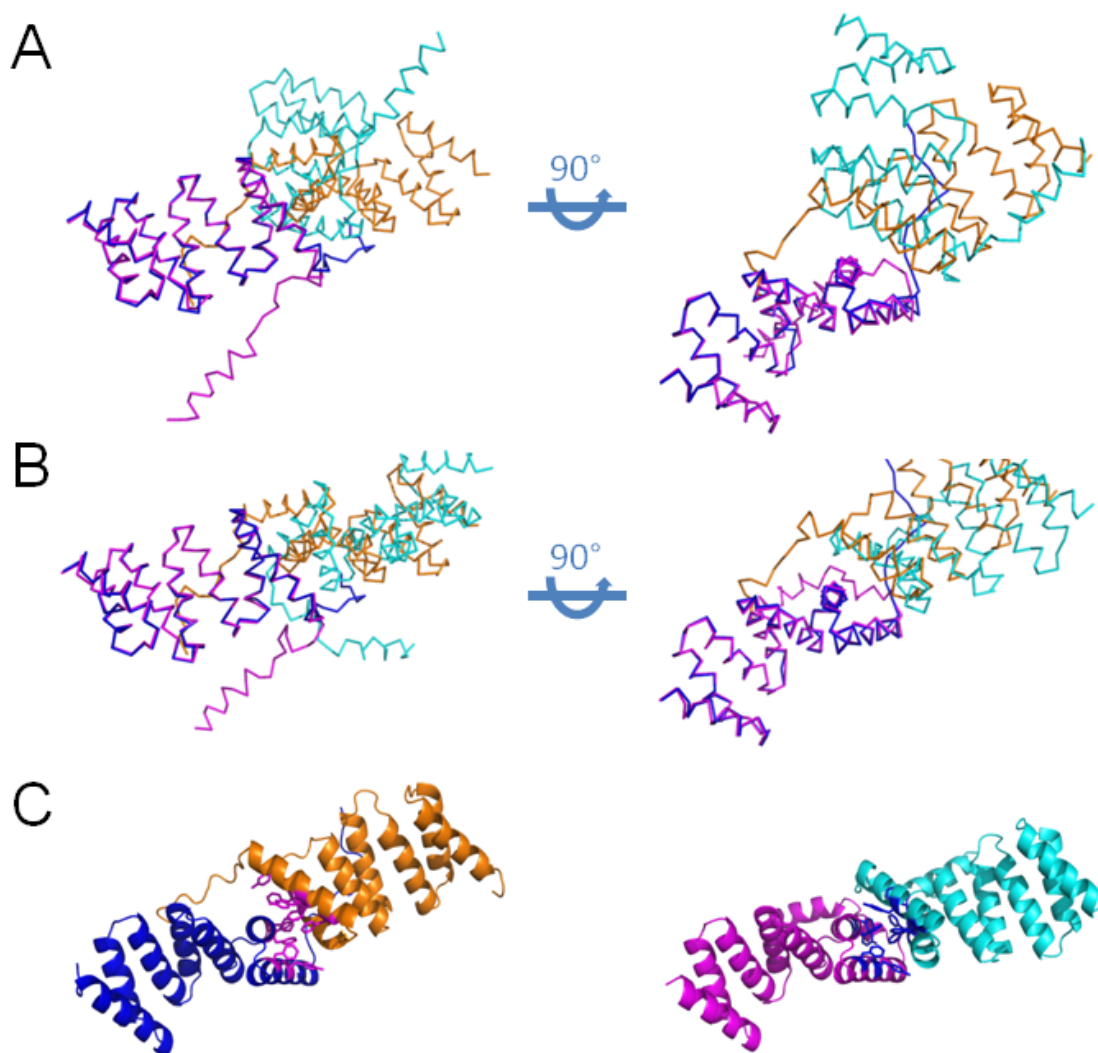
FIGURE 8. Comparison of IpgC$^{10\text{-}155}$ Dimers to Head-to-Head Dimer Assemblies Present in IpgC$^{1\text{-}151}$ Crystals. Both the free (3GYZ) and IpaB peptide-bound (3GZ1) structures of IpgC$^{1\text{-}151}$ were examined for potential "head-to-head" dimerization contacts similar to those observed in the IpgC$^{10\text{-}155}$ structure presented in Figure 4. *A*, Two orthogonal views of a putative dimer (magenta and cyan) from 3GZ1 superimposed with a prototypic dimer of IpgC$^{10\text{-}155}$(blue and orange). This dimer is generated by applying the crystallographic symmetry operator *x,-y+1,-z*, and buries 666.9 Å^2 of surface area upon formation. *B*, Two orthogonal views of a putative dimer from 3GYZ superimposed with the IpgC$^{10\text{-}155}$ dimer; all chains are colored as in panel A. This dimer is generated by applying the crystallographic symmetry operator *x-y,-y,-z+⅔*, and buries 950.4 Å^2 of surface area upon formation. *C*, Two identical views of the IpgC$^{10\text{-}155}$ dimer (left) and the symmetry-generated dimer from 3GYZ shown in panel B (right). The set of aromatic residues described in Figure 3 are colored magenta and blue in the left and right panels, respectively.

42

to the monomer found within the asymmetric unit; as a result, only 130 of 264 Cα positions superimpose within 4.0 Å distance. Separately, a "head-to-head" dimer is also observed within the lattice contacts of the unbound IpgC[1-151] structure (**Figure 8B**). This arrangement buries 950.4 Å^2 of surface area upon formation and, aside from the previously mentioned difference in the amino terminal region, shares a higher level of homology to the IpgC[10-155] dimer. In this case, 176 of 264 possible Cα positions superimpose within 4.0 Å distance. Most importantly, the aromatic residues which line this interface are identical to those found in the IpgC[10-155] dimer (**Figure 8C**), as described below.

Residues that Comprise the 'Head-to-Head' Dimerization Interface in IpgC are Conserved Across TTSS Class II Chaperones

While the IpgC[10-155] dimer buries approximately 1260 Å^2 of surface area upon formation, closer inspection reveals that this interaction is comprised largely of two separate regions from each respective monomer. The first of these gives rise to the SycD-like interface (~680 Å^2), and involves an intricate array of almost exclusively hydrophobic interactions between the α2 and α3 helices of opposing IpgC[10-155] chains. Chief among these is a network of homophilic contacts between Phe residues at positions 46, 58, and 61, the sidechains of which nearly intercalate with one another (**Figure 4B, C**). Hydrophobic interactions aside, a single hydrogen bond between the sidechains of Tyr[42] and Glu[53] is also found within this interface. Separately, a distinct region of contact that masks nearly 580 Å^2 of surface area is likewise observed in the IpgC[10-155] dimer. This interface arises from packing of nearly the entire extended amino terminus of one IpgC[10-155] chain against primarily the α5 helix of its counterpart polypeptide (**Figure 9**). Intriguingly, this region includes residues Ala[94] and Val[95], two residues whose concerted mutation has been shown to disrupt the dimerization of IpgC[1-151] (55). Analytical gel filtration chromatography was used to analyze the effect of this double mutant on the oligomeric state of both IpgC[1-151] and IpgC[10-155] (**Figure 10**). However, both proteins migrated as
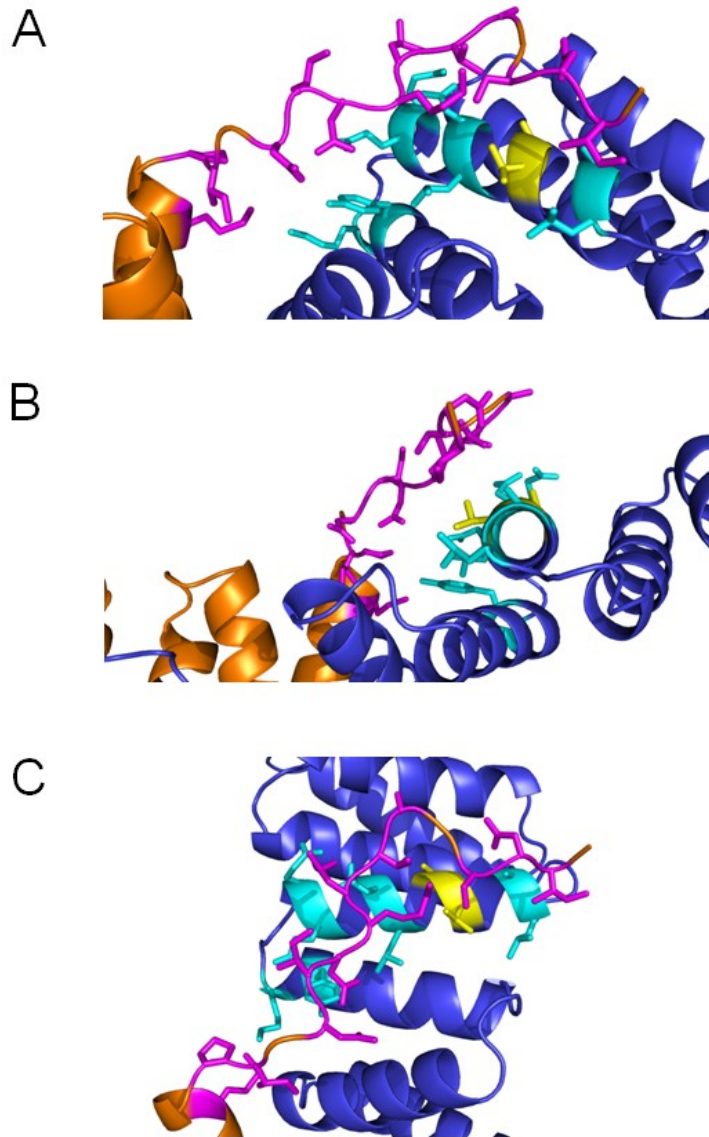
FIGURE 9. Magnified View of the Interface between the Amino-terminal Region and Helix α5 in an IpgC$^{10-155}$ Dimer. The individual monomers that comprise the IpgC$^{10-155}$ dimer are depicted as blue and orange cartoons, while the residues contributing to buried surface area (ball-and-stick) in this region are colored in magenta and cyan, respectively. Residues Ala^{94} and Val^{95}, which are critical for dimerization in IpgC$^{1-151}$ (55), are colored yellow for reference. *A*, Rendering of the IpgC$^{10-155}$ dimer from a viewing plane opposite that of Figure 4B, C. *B*, Rotated view of panel A such that the axis of helix α5 is orthogonal to the plane of the page. Note the packing of the amino-terminal residues (magenta) against the sidechains of α5 (cyan and yellow). *C*, Similar to panel B, but the viewing plane has been rotated 90° with respect to the page. The zigzag nature of the packing between the magenta-colored amino-terminus and the opposing monomer is evident in this image.
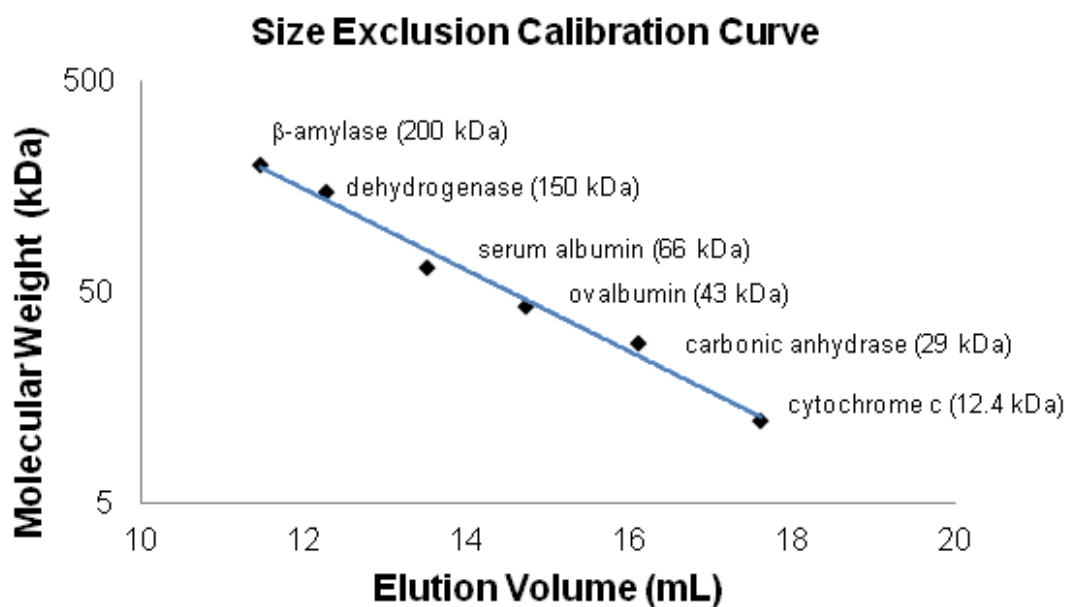
FIGURE 10. Calibration of the Analytical Size Exclusion Chromatography Column. Size exclusion standard curve where observed molecular weight is plotted as a function of elution volume. Calibration points (black diamonds) correspond to the following standard proteins: β-amylase (200kDa), dehydrogenase (150kDa), serum albumin (66kDa), ovalbumin (43kDa), carbonic anhydrase (29kDa) and cytochrome c (12.4kDa). Estimations of molecular weight were determined using the relationship MW = $31.195 \times e^{(-0.443 \times (E.V.))}$, where the molecular weight (MW) is given in kDa and the elution volume (E.V.) is given in mL; the correlation coefficient for this relationship (R^2) is 0.987 (blue line).

a single species with an observed molecular weight of approximately 40 kDa in this assay (**Figures 11**). In contrast to previous data (55), these results suggest that dimerization may not be fully ablated by simultaneous mutation of both Ala^{94} and Val^{95}.

The nature and extent of the contacts made by the IpgC$^{10-155}$ amino terminus makes it difficult to interpret the overall significance of sequence conservation in this region of the protein. However, examination of a structure-based multiple-sequence alignment of class II chaperones indicates that nearly all of the positions mentioned in regard to the SycD-like interface are well conserved (**Figure 12**). This is especially true in the case of BicA and SicA, which are less divergent members of this family. It is somewhat surprising that the residues participating in IpgC$^{10-155}$ homophilic contacts are biochemically distinct from those of SycD, which instead relies on hydrophobic contacts of opposing Ala^{61} and Leu^{65} sidechains for dimerization (13). The fact that the quaternary arrangement of IpgC$^{10-155}$ and SycD$^{21-163}$ is so similar, even though the residues lining this interface are different, strongly suggests that the ability to form this "head-to-head" dimer is a conserved structural feature among TTSS class II chaperones.

The 'Head-to-Head' Dimer of IpgC Supports Chaperone Activity

The remarkably different mode of dimerization between IpgC$^{10-155}$ and IpgC$^{1-151}$ raised questions as to whether two distinct quaternary arrangements could be supported by this protein. To address this question, analytical gel filtration chromatography was used to determine whether the dimers observed in the IpgC$^{10-155}$ structure were present in solution. Comparison of the elution profile of IpgC$^{10-155}$ to a calibration curve of globular protein standards reveals an observed molecular weight of approximately 36 kDa (**Figure 13A** and **Figure 11**); given a theoretical value of 16.7 kDa per monomer, this strongly suggests that this amino-terminally truncated IpgC behaves as a dimer in solution. This conclusion is also supported by chemical crosslinking of IpgC$^{10-155}$, which reveals the generation of covalent IpgC dimers following a timecourse exposure to the amine reactive agent BS^{3}

46

Analytical Gel Filtration of A94E/V95Q Double Mutants of IpgC Proteins
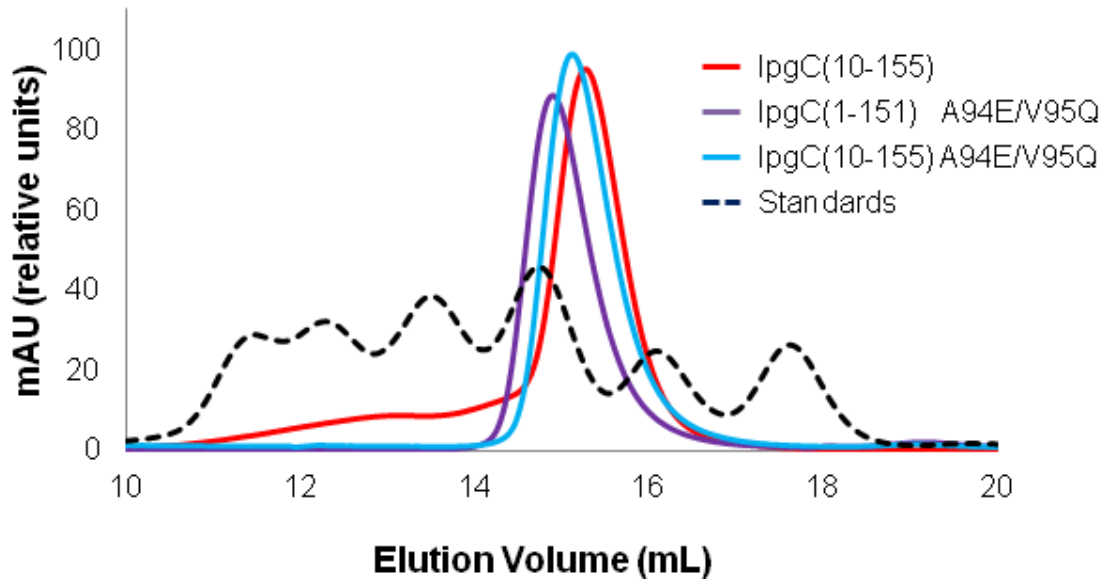
FIGURE 11. IpgC Double Mutants Exist as Dimers in Solution. Samples of purified IpgC (5 mg/mL) proteins were injected onto an analytical gel-filtration column and the elution profiles were compared to a series of known standards to derive an estimation of protein molecular weight **(Figure 11)**. The sample identities are IpgC[10-155] (red), IpgC[10-155] Ala[94]Glu/Val[95]Gln (cyan), and IpgC[1-151] Ala[94]Glu/Val[95]Gln (purple). The standard mixture is shown as a black dashed line. Aside from the standard injection, all curves were normalized to a maximum peak height of 100 mAU for clarity.
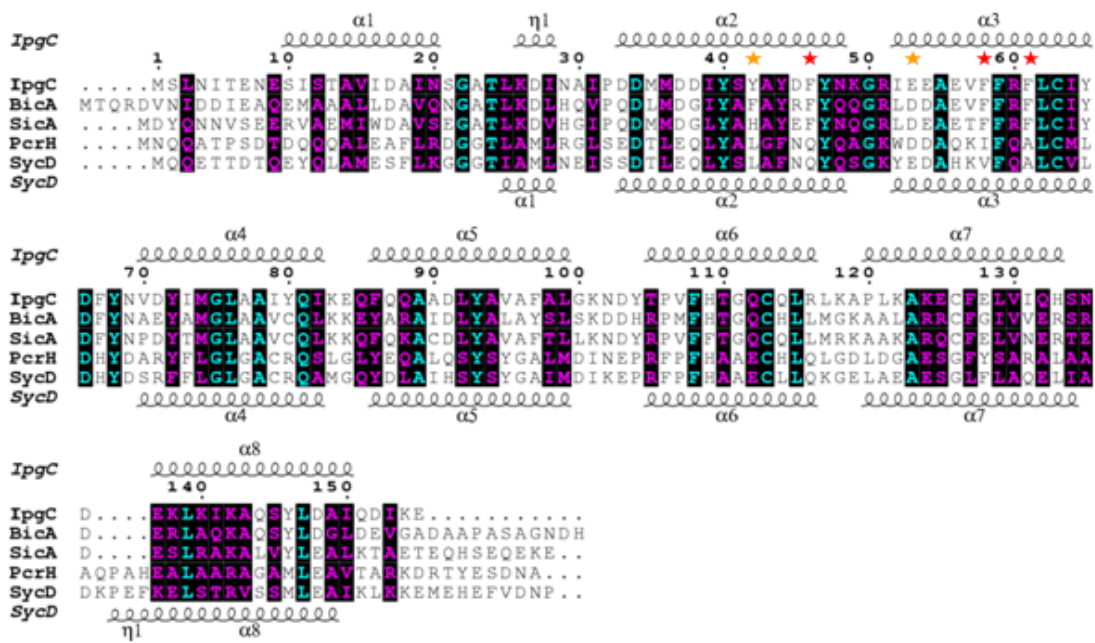
FIGURE 12. **Calibration Residues that Comprise the Head-to-Head Dimerization Interface in IpgC[10-155] are Conserved among Class II Chaperones.** The sequences of IpgC and its homologs were aligned using the ClustalW method (93) and compared to the secondary structure elements of both the IpgC[1-151] (55) and the SycD[21-163] (13) crystal structures with Espript (33). Residue positions were numbered using the IpgC sequence as a reference. Identical residues are shown in cyan typeface, while similar residues (as judged by the BLOSUM62 substitution matrix) are shown in purple typeface. Residues at positions 46, 58, and 61 form "head-to-head" contacts in the crystal structure **(see Figure 4C)** and are denoted with a red star. Residues at positions 42 and 53 appear to form sidechain-to-sidechain hydrogen bonds and are denoted with an orange star.

48
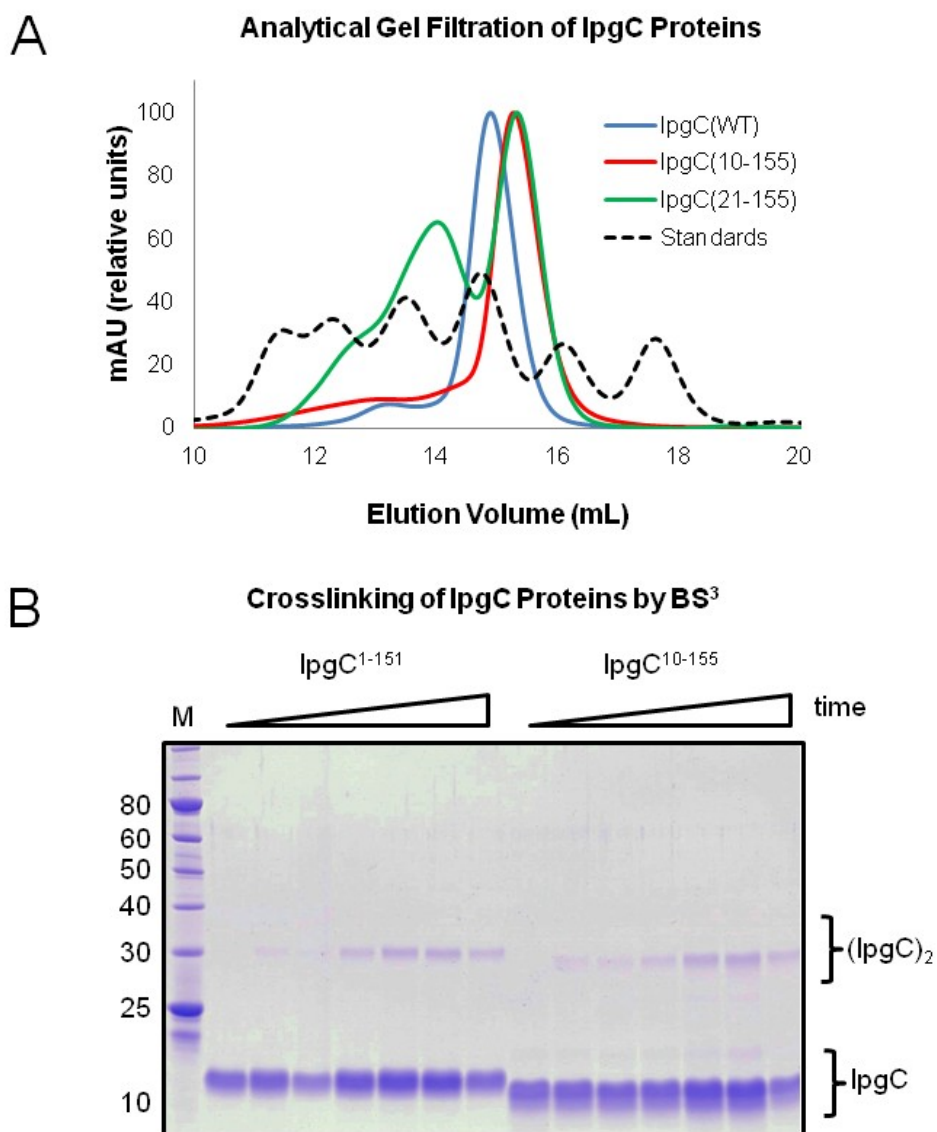
FIGURE 13. IpgC$^{10-155}$ Exists as a Dimer in Solution. *A*, Samples of purified IpgC (5 mg/mL) proteins were injected onto an analytical gel-filtration column and the elution profiles were compared to a series of known standards to derive an estimation of protein molecular weight **(Figure 11)**. The sample identities are IpgC^{WT} (blue), IpgC$^{10-155}$ (red), and IpgC$^{21-155}$ (green). The standard mixture is shown as a black dashed line. Aside from the standard injection, all curves were normalized to a maximum peak height of 100 mAU for clarity. *B*, Purified samples of IpgC representing both asymmetric (IpgC$^{1-151}$) and "head-to-head" dimers (IpgC$^{10-155}$) were exposed to the amine-reactive crosslinking agent BS^3. Samples were removed at 0, 15, 30, 60, 90, 120, and 240 min following the start of crosslinking, quenched by incubation with Tris, and analyzed for the presence of covalent dimers by SDS-PAGE.

Copurification of IpaB with IpgC
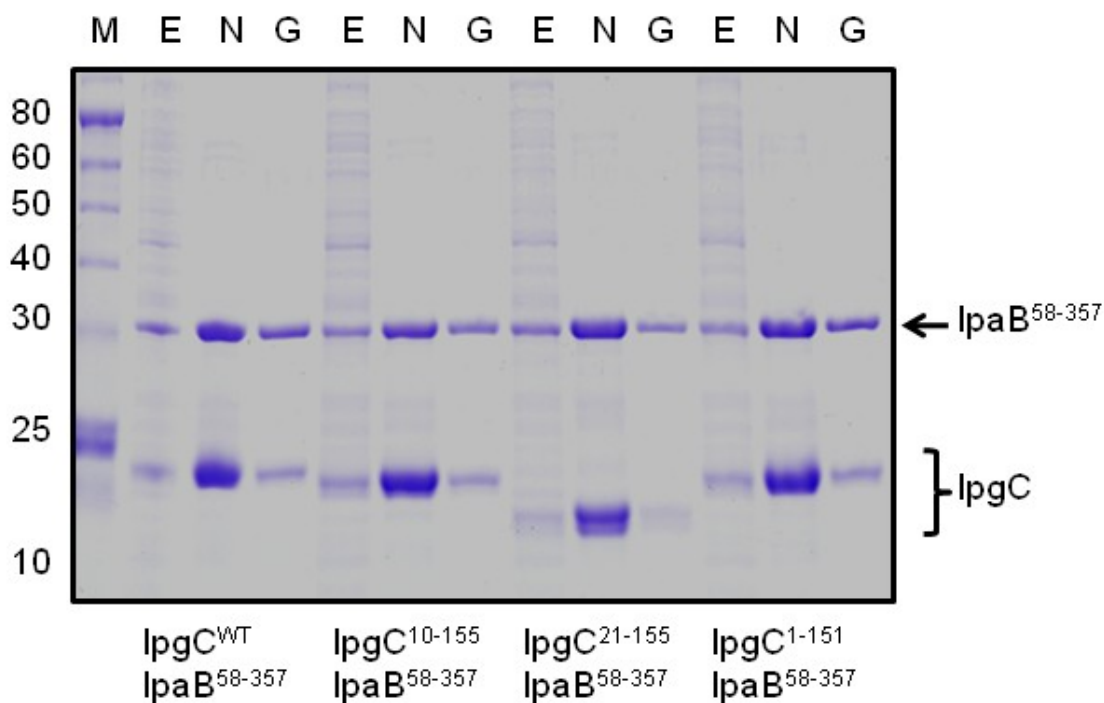
FIGURE 14. Amino-terminally Truncated forms of IpgC Retain Chaperone Activity for IpaB. Full-length and various truncated forms of IpgC were coexpressed with IpaB[58-357] in recombinant strains of *E. coli*. Following induction of protein expression, cells were harvested, lysed, and the soluble extracts were subjected to a copurification protocol to assess the ability of IpgC to bind IpaB. SDS-PAGE was used to analyze various protein samples following each step of copurification: M, protein molecular weight standards; E, clarified cellular extract following microfluidization and centrifugation; N, pooled elute following Ni^{2+}-Sepharose chromatography; G, pooled fractions of the complex following gel-filtration chromatography. Since IpaB accumulates in inclusion bodies in the absence of IpgC activity (63), and since the untagged IpaB lacks the ability to bind Ni^{2+}-NTA Sepharose on its own (72), all four IpgC proteins used in this study maintain chaperone activity.

(**Figure 13B**). Previous studies have also reported that genetic truncation of residues 1-20 in IpgC results in the formation of soluble but aggregated protein and that this is most likely due to the loss of both helices responsible for asymmetric dimerization of IpgC (55). However, two pieces of evidence suggest that this may not be entirely the case. First, while recombinant IpgC$^{21-155}$ did not behave as a single, ideal species when analyzed by gel filtration, it nevertheless migrated according to the defined oligomeric states of tetramer (63 kDa) and dimer (35 kDa). Second, IpgC$^{21-155}$ yielded diffraction quality crystals (**Table 1**), an outcome that seems highly unlikely with an aggregated sample. Separately, both of these amino-terminally deleted forms of IpgC maintain the ability to bind IpaB within the context of a copurification assay (**Figure 14**). Since IpaB cannot be expressed in a soluble fashion in *E. coli* without its cognate chaperone (63), this result indicates that these amino-terminally deleted proteins maintain the chaperone activity previously attributed to IpgC (7). Together, these results strongly suggest that residues 1-20 are dispensable for both dimerization of IpgC and for chaperone activity, and that IpgC is capable of adopting both asymmetric and "head-to-head" dimer arrangements in solution.

From primary to quaternary structure, these results presented here suggest that a symmetric dimerization interface is conserved across bacterial class II chaperones. In light of previous data which have described the structure and function of asymmetric dimerization, our results raise the possibility that class II chaperones may transition between asymmetric and symmetric dimers in response to changes in either biochemical modifications (e.g. proteolytic cleavage) or other biological cues. Such transitions may contribute to the broad range of protein-protein interactions and functions attributed to class II chaperones.

CHAPTER 4

IDENTIFICATION OF THE BILE SALT BINDING SITE ON IPAD FROM *SHIGELLA FLEXNERI* AND THE INFLUENCE OF LIGAND BINDING ON IPAD STRUCTURE

Overview

Type III secretion (TTS) is an essential virulence factor for *Shigella flexneri*, the causative agent of shigellosis. The *Shigella* TTS apparatus (TTSA) is an elegant nano-machine that is composed of a basal body, an external needle to deliver effectors into human cells, and a needle tip complex that controls secretion activation. IpaD is at the tip of the nascent TTSA needle where it controls the first step of TTS activation (90). The bile salt deoxycholate (DOC) binds to IpaD to induce recruitment of the translocator protein IpaB into the maturing tip complex (67). Recent spectroscopic analyses showed that IpaD undergoes a structural rearrangement that accompanies binding to DOC (24). Here we report a crystal structure of IpaD with DOC bound and test the importance of the residues that make up the DOC binding pocket on IpaD function. IpaD binds DOC at the interface between helices α3 and α7, with concomitant movement in the orientation of helix α7 relative to its position in unbound IpaD. When the IpaD residues involved in DOC binding are mutated, some are found to lead to altered invasion and secretion phenotypes. These findings suggest that adoption of a DOC-bound structural state for IpaD primes the *Shigella* TTSA for contact with host cells. The data presented here and in the studies leading up to this work provide the foundation for developing a model of the first step in *Shigella* TTS activation.

Structure of the IpaD[122.319]-DOC complex

IpaD[122.319]-DOC co-crystals were generated as described in Methods and diffracted synchrotron X-rays to 1.9 Å limiting resolution. However, since the initial crystals took nearly 4 months to appear, a number of routine analyses were conducted to address potential questions regarding fortuitous sample degradation. In particular, the results of SDS-PAGE and MALDI-TOF strongly suggested proteolytic loss of α helices 1-2' (approximately residues 40-120) that comprise the IpaD N-terminal domain. With this information, the crystal structure was solved by molecular replacement and contained two molecules of IpaD[122.319] within the asymmetric unit (**Figure 15**). Significantly, initial F_o-F_c maps (calculated as described in Methods) revealed unmodeled contiguous density (Fig. 1A) that represented bound DOC near the N-terminus (α3 and α7) of both IpaD[122.319] polypeptides. Upon placing each DOC ligand, the final model was refined to R_{work} and R_{free} values of 22.9% and 25.5%, respectively (**Fig. 16B** and **Table 6**).

In light of previous findings (90), the more relevant 1:1 complex was that shown in **Figure 16C** in which DOC is bound by a hydrophobic pocket formed by the interface of α3 and α7 of the central coiled-coil of IpaD[122.319]. While this was lower on the coiled-coil than predicted by previous computer docking simulations, it was still consistent with Förster resonance energy transfer (FRET) measurements between a coumarin fluorescence donor probe on Cys322 and the fluorescein acceptor tethered via a linker on FITC-DOC (90) when the length of the linker and dimensions of FITC were considered. The FRET-based distance between these two probes was determined at 42 Å; this was originally interpreted to position the DOC binding site about half way up the central coiled-coil of IpaD[122.319], and was in agreement with preliminary *in silico* analyses. However, when the six carbon tether linking fluorescein (~20 Å) to DOC is considered, DOC would actually be expected to lie in approximately the position shown in Figure 1C.

Table 6. Site Directed Mutagenesis of Key Residues Involved in DOC Binding

IpaD form	Relative Invasion		Hemolysis (%)[c]		IpaD on Surface[d]	
	- DOC[a]	+ DOC[b]	-DOC	+DOC	-DOC	+DOC
Null	0	0	1.9	2.0	0	0
Wild-type	100	335	30.1	23.9	95	93
L134S	141	125	33.5	31.1	98	96
L134E	152	200	38.4	32.9	95	93
K137S	74	237	27.8	25.3	95	96
I138S	91	333	31.7	33.1	94	96
L315S	147	614	35.5	31.4	97	92
L315E	10	0	5.5	3.0	5	<5
L134S/L315S	0	0	1.4	2.0	0	0
L134E/L315E	0	0	1.8	1.7	0	0

[a]Relative to invasion by *S. flexneri* expression wild-type IpaD without DOC added. All invasion results are with less than 15% standard deviation for any individual experiment. Experiments were repeated at least three times. The activity of the complemented *S. flexneri* strain was approximately 80% as invasive as wild-type M90T (75). The wild-type bacteria also responded to DOC with similarly enhanced invasiveness.

[b]Contact-mediated hemolysis is shown relative to complete hemolysis caused by the addition of water.

[c]Contact-mediated hemolysis was determined by a modification of our standard procedure. The number of bacteria and incubation time used were reduced and the values given are relative to 100% lysis using water. A PBS negative control for lysis had a value of 2.2% lysis and all values have a standard deviation of less than 2% based on triplicate measurements from multiple experiments.

[d]Surface localization of IpaD was determined by immunofluorescence staining using anti-IpaD antibodies and is given as the percent cells in multiple fields possessing visible IpaD on their surfaces. Results for L315E varied and in some cases there was no IpaD visible on the bacterial surface prior to addition of DOC.
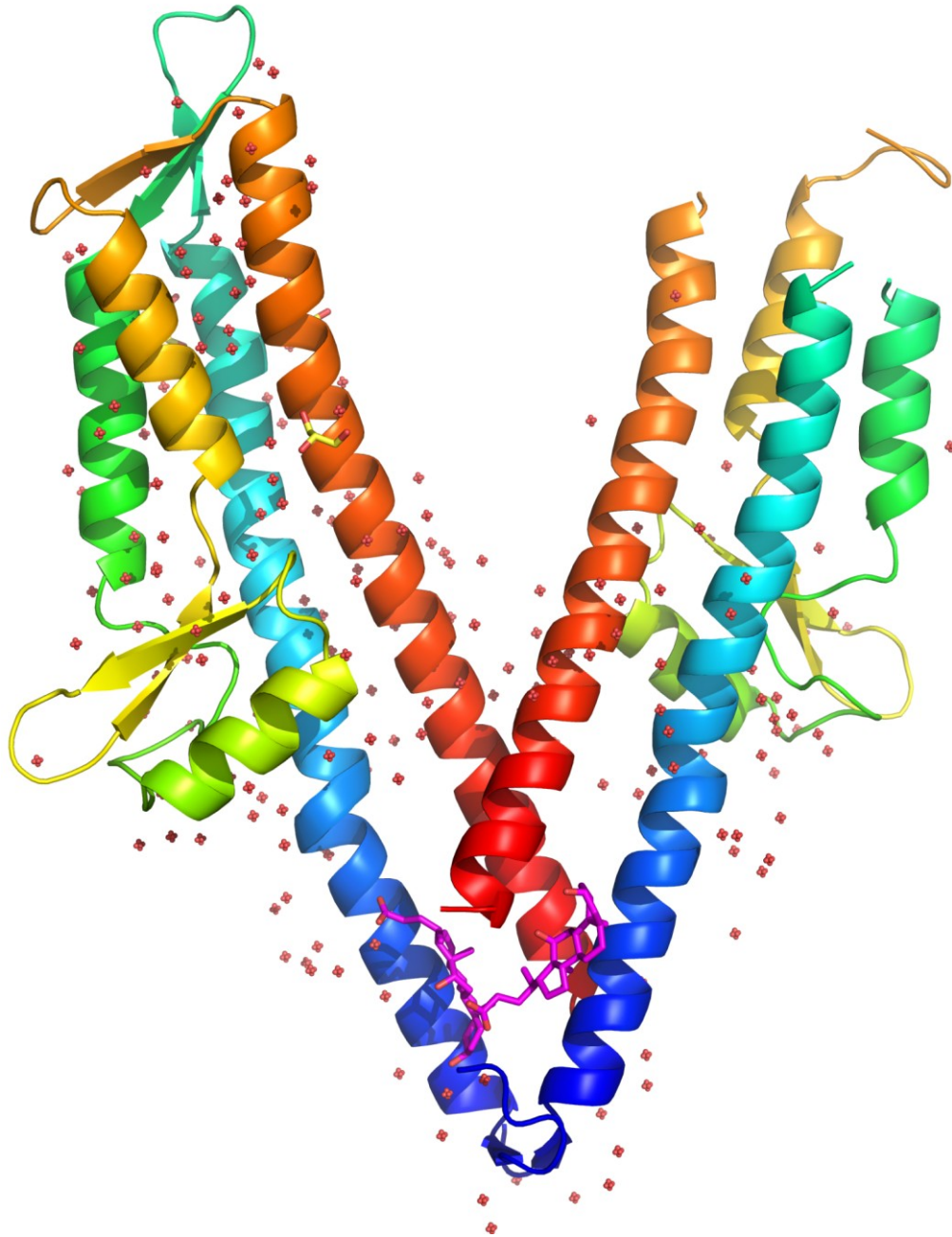
FIGURE 15. Asymmetric unit of 1.90 Å cocrystal structure of IpaD Fragment from *Shigella flexneri* bound to DOC. Crystal structure depicting two copies of IpaD[122.319] (blue (N-terminus) to red (C-terminus coloring scheme)) in ribbon format bound to DOC within the asymmetric unit.
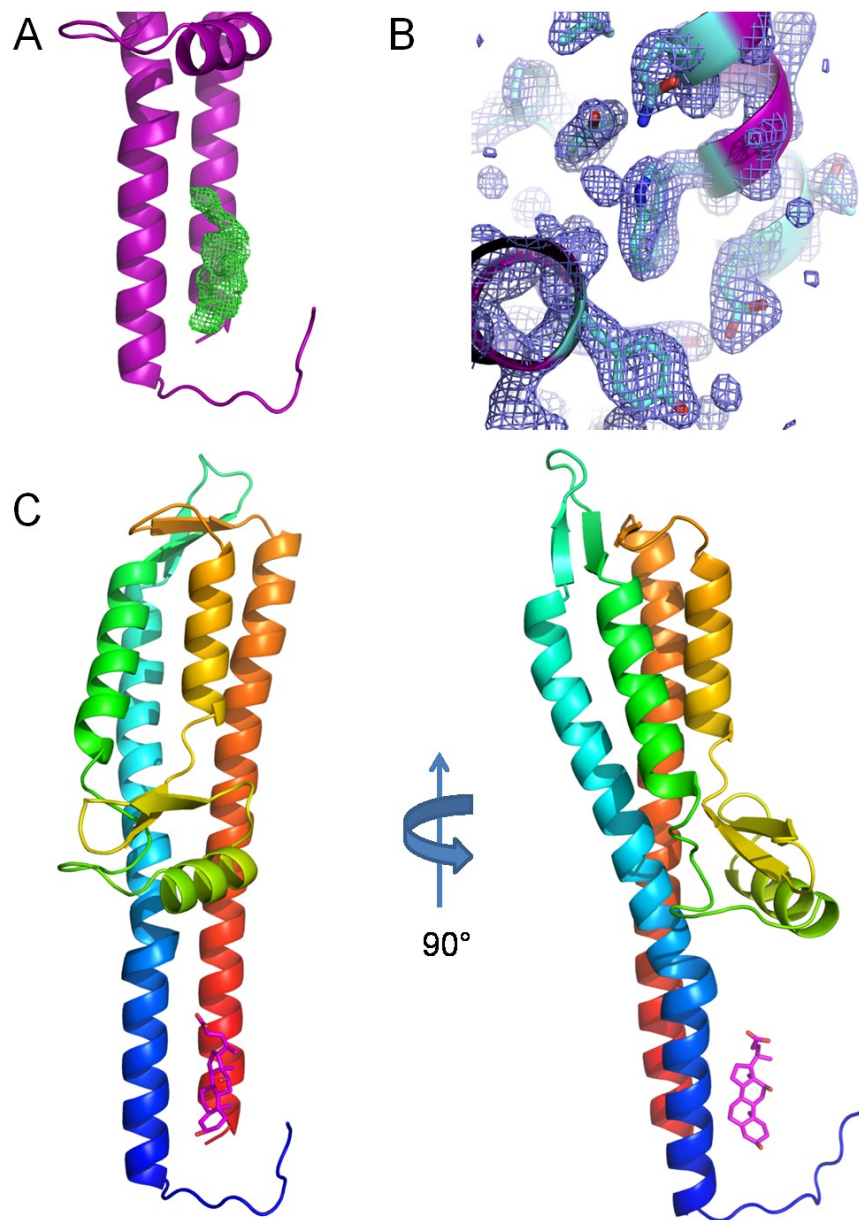
FIGURE 16. 1.90 Å-resolution cocrystal structure of IpaD Fragment from *S. flexneri* bound to DOC. *A*, *F*o-*F*c map (green mesh at 2.0σ contour) of the refined structure in the absence of modeled bile salt. IpaD backbone is depicted in cartoon ribbon format (purple). *B*, Representative model-to-map correlation of an aromatic region of IpaD[122-319] with the *2Fo-Fc* weighted electron density (contoured at 2.0σ) depicted as a blue mesh. *C*, Crystal structure of a single copy of IpaD[122.319] in ribbon format bound to DOC. The two views of the molecule are related by a 90 degrees rotation about the central coiled-coil axis.

When the structure of IpaD[122.319] with DOC bound was superimposed with the native

structure of IpaD, it was apparent that bile salt binding was accompanied by a change in the overall

conformational distribution of the protein (**Fig. 17A**). Specifically, the central coiled-coil (α3 and α7)

became constricted by 2.7 Å in the DOC-bound state, with α5 of the C-terminal domain contracting

slightly as well. This constriction of α7 led to a 7.8 Å shift with respect to its original position within

native IpaD. Again, however, these data were consistent with the previous FRET-based findings of

Dickenson *et al.* (24) who proposed that a kink formed between residues 146 and 149 in α3 of the

central coiled-coil may be a key contributor to the conformational changes observed in solution.

This change is illustrated in the structural overlay depicted in Figure 2B. It was previously found that

DOC binding to an N146Q mutant of IpaD did not appreciably change the conformational

distribution of the protein (as determined by NMR chemical shift mapping) (24). This was

accompanied by a significant reduction in *Shigella* invasiveness. Interestingly, while Dickenson *et al.*

(24) proposed that DOC binding likely stabilized the helical character of α3, the overlay in **Figure

17B** instead suggests that ligand binding stabilizes formation of a bulge at this position.

Site directed mutagenesis of residues involved in DOC binding – effect on host cell invasion

The IpaD[122.319]-DOC structure described in **Figure 16** was analyzed by the CCP4 program

Contact (1, 77) to identify residues located within 2.6 – 5.0 Å of DOC that appeared to contribute to

DOC binding. This identified several positions along IpaD helix α3 (Ile129, Lys137, Ile138, Ser141

and Ile145) as well as a single residue (Leu311) along helix α7. However, two other residues within

this hydrophobic pocket appeared to be most intimately involved in DOC binding; these were Leu134

and Leu315, which are highlighted within **Figure 18**. Using this information, a majority of these

positions were targeted for mutagenesis to assess directly their importance with respect to DOC

binding, and therefore IpaD function. In particular, changes to serine were used to render these
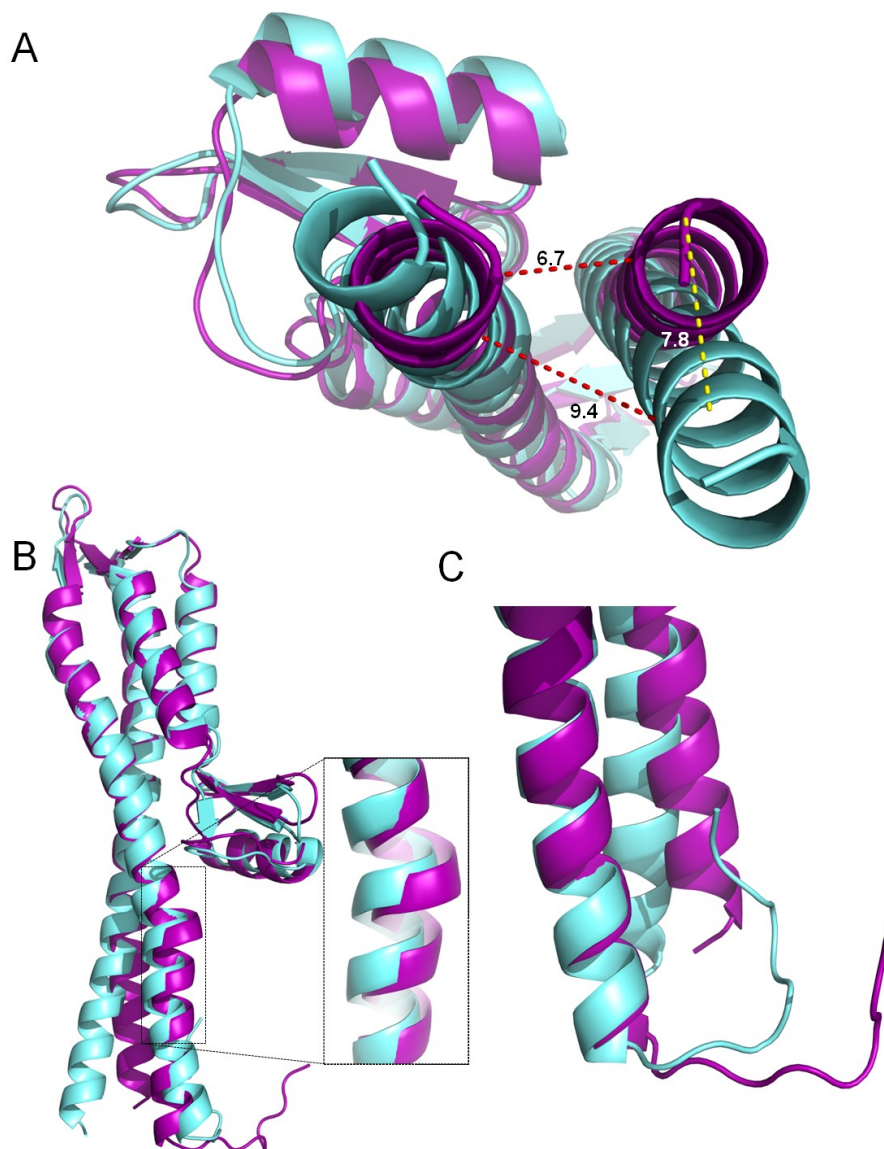
FIGURE 17. Structural alignment of native and DOC-bound IpaD crystal structures. PDB ID: 2J0O, 'native' IpaD[15-332] (aquamarine); 3R9V, DOC-bound IpaD[122.319] (purple). *A*, Structural alignment of native and DOC-bound IpaD structures. Constriction of α3 (left) and α7 (right) highlighted (in red) with distance apart (Å) for both structures (measured from Ile138 to Leu315 on each helix). Movement of α7 (measured from Thr319 carbonyl atom of each structure) within both structures is highlighted in yellow. *B*, Alignment of native and DOC-bound IpaD structures highlighting the exacerbation of the 'kink' region. Coloring of both structures is the same as in panel A. *C*, Alignment of native and DOC-bound IpaD structures, highlighting the distension of the 10 most N-terminal residues within DOC-bound structure when compared to the equivalent region in native IpaD (DOC removed for clarity). Coloring of both structures is that same as in panel A.

normally hydrophobic positions more polar, while changes to glutamate were used to introduce a formal negative charge at these sites.

Whereas several mutants displayed invasion phenotypes that were largely similar to that of *S. flexneri* SF622 expressing wild-type IpaD (the results for only K137S and I138S are shown in **Table 6**), two of the mutants proposed to be most directly involved in DOC binding showed notable changes in invasiveness (**Table 6**). In a typical experiment, the addition of DOC has been shown to cause a three- to four-fold increase in *Shigella* invasiveness of cultured HeLa cells (67). Significantly, the L134S and L134E mutants displayed enhanced invasiveness relative to wild-type IpaD in the absence of DOC, and the addition of DOC had what appeared to be a reduced stimulatory effect on this level of invasiveness (**Table 6**). L315S was also mildly enhanced in invasiveness relative to wild-type IpaD and the addition of DOC caused an increase in invasiveness, even though the increase was somewhat greater than expected (approaching six-fold; **Table 6**). Together, these findings suggested that side chain-ligand interactions of L134 and L315 are critical to the DOC effect on *Shigella* invasiveness.

In contrast to what was seen with either mutation of L134 or that of L315S, mutation of L315 to glutamate (L315E) resulted in a nearly complete loss of invasiveness (**Table 6**). A similar phenotype was observed if both residues were mutated to serine or to glutamate simultaneously (giving L134S/L315S and L134E/L315E, respectively) (**Table 6**). Because these mutants contained multiple mutations, it remained possible that their loss of function was due to induced structural instability; however, each of these proteins could be purified without observable degradation, and no significant changes in their circular dichroism (CD) spectra relative to native IpaD were observed.
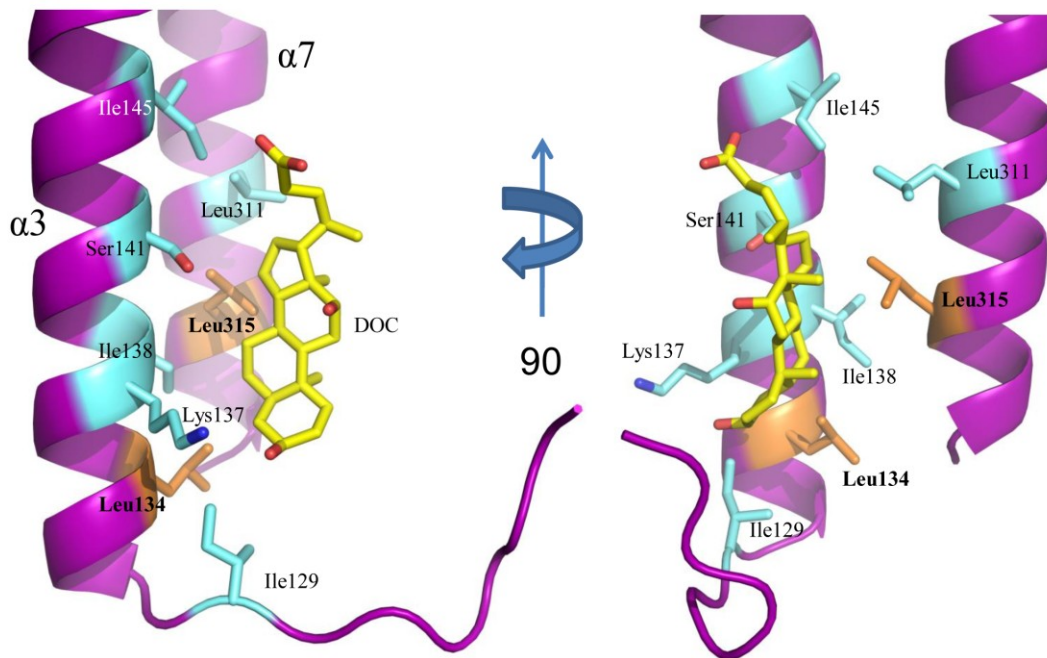
FIGURE 18. DOC-bound active site within IpaD. Amino acid side chains (aquamarine) of IpaD[122.319] within 2.6 - 5.0Å of DOC (yellow). IpaD backbone is depicted in cartoon ribbon format (purple). Side chains intimately involved in DOC interaction, Leu134 and Leu315, are highlighted in orange Crystal structure rotated 90° about the central coiled-coil axis on the right.

Separately, since some of these mutations resulted in what appeared to be enhanced invasiveness prior to DOC addition, it was also possible that these mutations involving residues L134 and L315 might have instead caused IpaB to appear prematurely on the bacterial surface. Indeed, this appeared to be the case since immunofluorescence microscopy showed staining for IpaB on the surface of *S. flexneri* even in the absence of DOC (approximately 93% of cells in each case). At the same time, the same sets of mutations did not change the levels of IpaD presentation on the *Shigella* surface relative to bacterial expressing wild-type IpaD (**Table 6**). Thus, when considered as a whole, these results suggest that L134 and L315 of IpaD have important roles in invasion by *S. flexneri*.

Effect of mutations on contact-mediated hemolysis by *Shigella*

Contact hemolysis provides a measure of *Shigella* ability to insert translocon pores into target cells when the two are forced into contact with one another. As such, it provides an alternative measure of TTSA maturation and function. When the standard contact-mediated hemolysis assay was modified so that it gave subsaturating levels of erythrocyte lysis, similar trends were observed as for the invasion results presented above in the absence of DOC (**Table 6**). *S. flexneri* producing mutant forms of IpaD that had lost their invasion ability (notably L315E, L134S/L315S and L134E/L315E) were unable to cause significant red blood cell lysis, which indicated that they could not efficiently insert a functional translocon pore into the erythrocytes (102). L315E did appear to display a minor amount of contact hemolytic activity that also seemed to correlate with its very low level of invasiveness. Interestingly, those mutants that displayed elevated invasiveness relative to *S. flexneri* making wild-type IpaD in the absence of DOC also appeared to demonstrate modest increases in contact hemolysis activity (**Table 6**).

In contrast to the invasion results following the addition of DOC, there was no clear increase in contact hemolysis by bacteria following incubation with DOC. In fact, *Shigella* making wild-type IpaD appeared to show an overall decrease in contact hemolysis activity (**Table 6**). This is probably

due to the fact that this assay requires that the bacteria be forced into contact with the red blood cells, thereby making it inherently less sensitive to any subtle changes that might be caused by prior incubation with DOC. Nevertheless, mutations within the DOC binding pocket of IpaD did appear to have slight effects on *Shigella*'s contact hemolysis activity, even though monitoring invasion appears to be the most sensitive method to follow the TTSA needle tip maturation process.

The ability to properly deliver a functional translocon pore (consisting of IpaB and IpaC) into target cells is essential for delivery of the effector proteins needed for cellular invasion. Because of this, one possible reason for the inability to invade or induce any contact-mediated hemolysis was that IpaD had lost its ability to remain stably anchored at the TTSA needle tip. Indeed, this appeared to be the case as judged by immunofluorescence microscopy studies. Whereas *S. flexneri* producing mutant forms of IpaD that could not restore invasion or contact-hemolysis failed to show detectable staining for IpaD on their surfaces in the presence or absence of DOC (**Table 6**), all of the invasive *Shigella* strains showed similarly high levels of IpaD on their surfaces without regard to DOC. Curiously, L315E displayed very low levels of both invasiveness and contact hemolysis and had variable staining for low levels of IpaD on the surface (**Table 6**); however for this mutant DOC addition resulted in loss of invasiveness, contact hemolysis, and IpaD surface localization altogether.

Influence of IpaD mutations on secretion control

As mentioned above, the loss of invasiveness for L134S/L315S correlated with a loss of detection of IpaD on the *Shigella* surface (**Table 6**). Because an important function of IpaD is to control type III secretion, the different IpaD mutants were likewise examined with respect to overnight secretion of the translocators. As would be expected, an *ipaD* null strain (SF622) showed no IpaD in overnight culture supernatant fractions, but released elevated levels of IpaB and IpaC into the medium; this reflected an inherent inability to control background levels of type III secretion. Oppositely, secretion control was restored back to low overnight levels when SF622 was

complemented with wild-type IpaD (**Fig. 19**). This level of secretion control was equivalent to what has been seen routinely for both complemented and wild-type *S. flexneri (75)*.

For most of the remaining IpaD single-site mutants described in **Table 6**, overnight secretion appeared to be approximately equivalent to that of the wild-type form of the protein. In contrast, the L134S/L315S double mutant had completely lost secretion control and released large amounts of IpaD, IpaB and IpaC into *Shigella* culture supernatant fractions (**Fig. 19**). The L134E/L315E and L315E mutants gave similar results (data not shown). Because both L134/L315 double mutants and L315E can be readily purified and still maintained expected levels of α-helical structure, these mutations do not appear to cause instability in the overall fold of IpaD; however, based on surface localization experiments (**Table 6**), there could be a change in their conformational distribution that leads to a disruption of the protein-protein contacts needed to maintain IpaD at the TTSA needle tip. In this regard, it is interesting to note that a similar phenotype was observed for IpaD when short C-terminal deletions had been introduced (75).

Discussion

Within these experiments, we have expanded upon previous studies (24) by generating *Shigella* strains that express mutant forms of IpaD and performing detailed phenotypic analyses of the earliest stages of TTSA needle-tip complex formation and progression. This work was made possible by identifying a bile salt-binding pocket in IpaD, as judged by a 1.9 Å co-crystal structure of DOC bound to a core fragment of IpaD (i.e. IpaD^{122,319}). Even though initial crystallization studies were conducted with full-length protein, time-dependent proteolytic degradation of IpaD occurred slowly in the presence of saturating levels of DOC and lead to the loss helices 1-2' specifically (approximately residues 40-120). These residues comprise a small domain that has previously been proposed to serve a self-chaperoning function that prevents premature IpaD oligomerization (45). A similar, yet even more extensively truncated form of IpaD (i.e. residues 133-319; PDB ID 2J0N) was

63
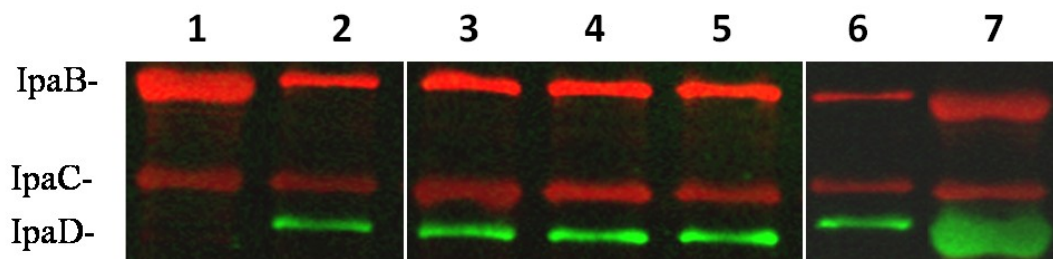
FIGURE 19. Control of overnight secretion for *S. flexneri* SF622 expressing different IpaD mutants. Bacteria were grown overnight in TSB and the proteins present in equal amounts of culture supernatant were separated by SDS-PAGE. IpaB, IpaC and IpaD (labeled) were then detected by immunoblot analysis as described in Methods. The relative abundance of each protein was estimated based on the size of the observed bands. The lanes shown are for supernatants from the following: 1) *S. flexneri* SF622 (*ipaD* null mutant), 2) SF622 expressing wild-type IpaD or 3) L134S, 4) K137S, 5) I138S, 6) L315S, and 7) L134S/L315S. The level of overnight secretion seen for the complemented strain was similar to that seen for overnight secretion by wild-type *S. flenxeri* (75). Lanes were not contiguous, but were from the same gel.

also identified during the prior crystallographic studies of Johnson *et al.* (45). Indeed, superposition of this truncated form of IpaD with that of DOC-bound IpaD reveals that both polypeptides adopt nearly identical structures (168/198 Cα positions align within 5.0 Å with an RMSD of 1.18 Å, **Fig. 20**). It is interesting to note that the truncated IpaD characterized by Johnson *et al.* was generated by deliberate in-drop proteolysis, while the degradation product described here occurred unexpectedly. Furthermore, loss of the self-chaperone domain in IpaD was both time and DOC-dependent, since full-length IpaD itself is stable up to one year at concentrations approaching 1 mM in neutrally-buffered saline solutions (unpublished observations).

Protease sensitivity in the presence of ligand(s) has been documented in the past, and has found use as a sensitive biochemical probe for changes in protein conformation and dynamics (18, 41, 69, 89) In previous work from our lab, we used increased trypsin sensitivity in the presence of a small bacterial protein (~8.5 kDa) to identify a conformational change in the human complement protein C3b (~175 kDa) (35). Since then, we have shown that this protein ligand restricts the overall conformational space sampled by C3b by stabilizing an open conformer that exists in solution, and thus affects its function through a largely allosteric mechanism (15). While these illustrative changes in C3b involve fairly substantial movements, the conformational changes observed between free and bound IpaD appear to be less dramatic. In particular, they are centered around exacerbation of the helical bulge in α3 and a constriction of the central α3 α7 coiled-coil of IpaD (**Fig. 17A, B**). It has to be noted that loss of the self-chaperone domain in the structure presented here precludes a comparison between free and bound forms of IpaD on a truly level basis. The absence of the N-terminal chaperone domain from the DOC-bound structure may actually provide a more appropriate protein model with respect to IpaD structure. The chaperone domain of IpaD is proposed to lie external to the needle after being moved away from the protein body (*i.e.* the central coiled-coil) as it docks at the needle tip (30, 45, 102). Furthermore, current understanding of protein structure also suggests that crystallography is also not the best approach to address such questions in the first place, since the
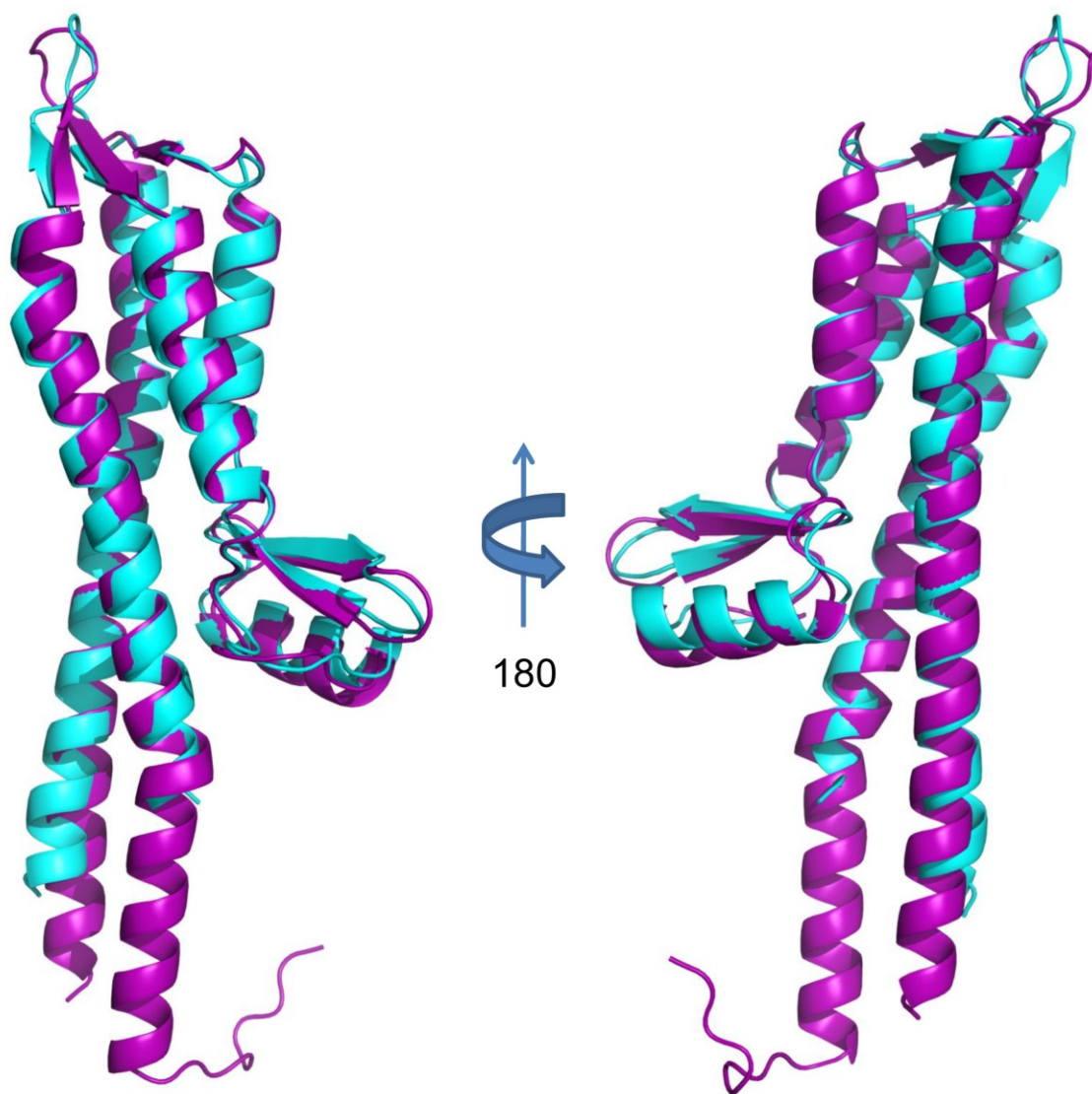
FIGURE 20. Structural alignment of truncated and DOC-bound IpaD crystal structures.
Crystal structures of proteolytically truncated, native IpaD (PDB ID: 2J0N, colored cyan) and
DOC-bound IpaD[122.319] (colored purple). 168/198 Cα positions align within 5.0 Å with an
RMSD of 1.18 Å. The aligned structures are rotated 180° about the central coiled-coil axis on
the right.

structures that result are time-averaged snapshots taken under substantial physical constraints. In keeping with this view, recent models of allostery and ligand-mediated structural transitions would argue that DOC binding stabilizes a pre-existing intrinsic conformation in IpaD, rather than "inducing" or "causing" an altogether new conformation *per se* (21, 95). Thus, the truncated form of IpaD identified by Johnson *et al.* may actually represent the ligand-bound conformation of IpaD seen in the absence of DOC. Finally, while it would be overly speculative to comment on the statistical distribution between the free and DOC binding-competent forms within full-length IpaD, the fact that conformational changes could be detected by both FRET and NMR shift mapping in the presence of DOC strongly suggest that these transitions must occur readily, at least *in vitro*.

Mutational analysis presented here reveals that disruption of the two IpaD residues most closely linked to DOC binding (L134 and L315) resulted in the greatest effects on IpaD-dependent virulence functions. In particular, both the L134S/L315S and L315E mutants lost control of secretion regulation, which potentially implicates the ability to bind DOC in maintenance of IpaD at the needle tip. Since DOC-binding correlates with structural differences in IpaD (as determined by FRET, NMR, and now crystallography), it is possible that changes emanating from the DOC binding pocket precipitate minor conformational shifts that affect the manner in which IpaD interacts with the TTSA needle. In the most direct conceptually-simple case, mutations that influence these conformational changes could impact how well IpaD is stably maintained at the TTSA needle tip. This would be interesting because loss of IpaD from the bacterial surface following mutation of its DOC-binding site suggests that bile salts influence key protein-protein interactions within the needle tip complex, suggesting that these interactions are critical for regulating secretion control. It is also possible that these altered interactions could serve to propagate a DOC-mediated signal from the TTSA needle tip to the base of the TTSA structure. Finally, DOC binding could influence the nature of IpaD's interaction with the first translocator, IpaB, which is held within the core of the TTSA needle or

needle tip complex (67). This could explain why only IpaB is recruited to the TTSA needle tip after following IpaD/DOC binding (67).

Recently there have been two papers published that describe the structures of the IpaD homologue from *Salmonella*, SipD, with bile salts bound. In the first of these, Chatterjee *et al.* presented the structures of a fragment of SipD (SipD$^{39.342}$) bound to deoxycholate and chenodeoxycholate (14). Comparison of these structures with that of IpaD$^{122.319}$-DOC described here reveals two noteworthy differences. First, while DOC binding appears to involve an alternative conformation in IpaD, the apo- and bile salt-bound structures of SipD$^{39.342}$ are nearly identical to each other (29). Whether or not this is due to the presence of the N-terminal self-chaperone domain in SipD remains unclear at this time. Second, whereas the stoichiometry of the IpaD$^{122.319}$-DOC interaction presented here appears to be 1:1 for each IpaD monomer, the SipD$^{39.342}$ co-crystal structures displayed 1:1 stoichiometry only when considered within the context of needle tip multimer (45). Confounding the interpretation of these SipD data is a second paper, which was published after the present work was first submitted. In this report, Lunelli *et al.* proposed an entirely different DOC binding site on SipD than was described by Chatterjee and colleagues (54). In particular, they analyzed a form of SipD fused to PrgI, and suggested that DOC binding involved a region that arose via the interface of SipD and PrgI. Mutagenesis of the SipD residues involved in PrgI binding indicated that the residues involved in binding DOC were also important for SipD function. Among these positions in SipD are R232, Q233 and S236, which are in close proximity to the DOC binding site, as are at least eight residues from PrgI. This stands in perplexing contrast to the previous report on SipD (14), in which residues near the bile salt-binding site are derived from the two different polypeptides (i.e. R41, I45, K338 and F340 from the A subunit, and N104, A108, L318, N321 and L322 from the B subunit). In light of our work described here, it is actually this latter SipD binding site that corresponds more closely to the DOC-binding residues from IpaD. Again, though, it has to be mentioned that this binding site described by Chatterjee *et al.* is comprised of an interface between

adjacent SipB monomers and involves residue contributions from the N-terminal chaperone domain, which is missing in the IpaD[122.319]-DOC co-crystal.

As discussed earlier, the N-terminal domain of IpaD is predicted to associate with MxiH upon extrusion from the needle. The remaining residues of the N-terminal domain within the IpaD[122.319]-DOC structure assume a non-classical secondary structure and extend much further away from the central α3-α7 coiled-coil than observed in the wild-type IpaD structure (**Fig. 17C**). This structural change could be the equivalent of the N-terminal domain "swinging away" in the presence of MxiH at the needle tip as previously hypothesized (30), though this remains to be substantiated. Previously, Zhang *et al.* proposed a model of the IpaD-MxiH interaction in which α3 of IpaD plays a critical role (102). This model, which is shown in **Figure 21**, places the C-terminal domain of IpaD on the outside of the needle core. More significantly in terms of the present work, it also places the location of the DOC binding site identified here on the outside face of the needle. While there is currently some uncertainty regarding the number of IpaD molecules present in the tip complex, it seems fairly likely that the polypeptides involved in forming the secretion plug would continue the canonical helical rise seen within the polymerization of the needle protein MxiH (45). Thus, constriction of both helices comprising the central coiled-coil (as judged by the free versus DOC-bound IpaD structures) provides a potentially attractive mechanism for the opening of the needle pore. The anchoring of IpaD to MxiH would imply that a global constriction of the tip protein should pull IpaD away from the central pore of the needle. This scenario would resemble the opening of an iris on a microscope.
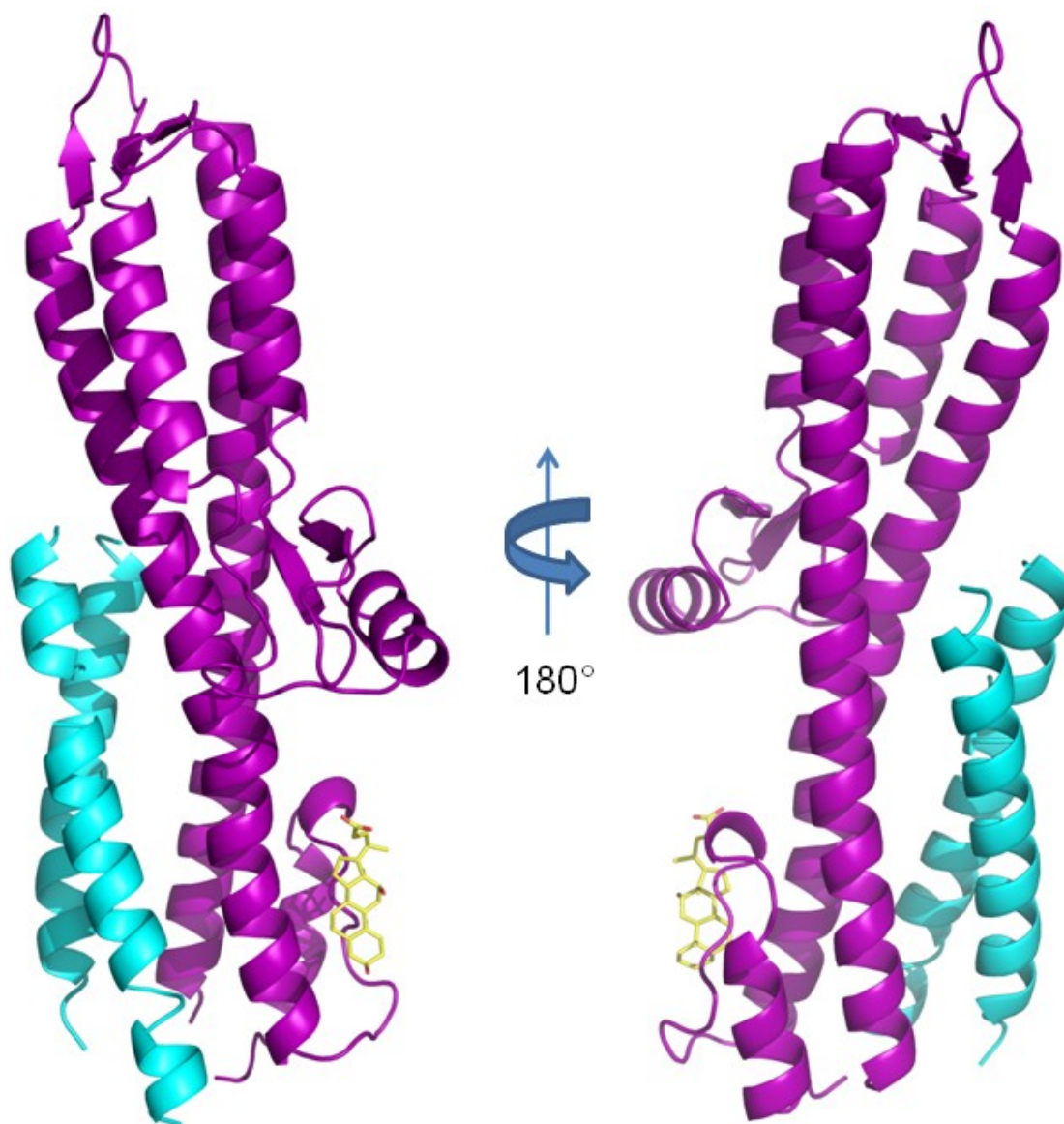
FIGURE 21. Model of IpaD-MxiH Interaction. Crystal structures of native IpaD (purple, with first 100 residues removed for clarity), MxiH (cyan) and DOC (yellow, modeled in equivalent position from DOC-bound structure). The modeled structure is rotated 180° about the central coiled-coil axis on the right.

CHAPTER 5

COILED-COIL DOMAIN FROM TYPE THREE SECRETION SYSTEM

FIRST TRANSLOCATOR PROTEINS REVEAL HOMOLOGY TO

PORE-FORMING TOXINS

Overview

Many pathogenic Gram-negative bacteria utilize type III secretion systems (TTSS) to alter

the normal functions of target cells. *Shigella flexneri* uses its TTSS to invade human intestinal cells

to cause bacillary dysentery (shigellosis) which is responsible for over one million deaths per year.

The *Shigella* type III secretion apparatus (TTSA) is comprised of a basal body spanning both bacterial

membranes and an exposed oligomeric needle. Host altering effectors are secreted through this

energized conduit to promote bacterial invasion. The active needle tip complex of *S. flexneri* is

composed of a tip protein, IpaD, and two pore-forming translocators, IpaB and IpaC. While the

atomic structure of IpaD has been elucidated and studied, structural data on the translocators from the

TTSS family remain elusive. We present here the crystal structures of the N-terminal regions of IpaB

from *S. flexneri* and SipB from *Salmonella enterica* serovar Typhimurium determined at 2.1 Å and

2.8 Å limiting resolution, respectively. Both structures are comprised of an extended length (114 Å in

IpaB and 71 Å in SipB*)* coiled-coil motif sharing a high degree of structural homology to not only

each other, but also with their TTSA needle tip protein partners and pore-forming proteins from other

Gram-negative pathogens (notably, colicin Ia).

**Identification of a Soluble N-terminal Region within the TTSS First Translocators**

Given the limited structural information for the TTSS translocators and the instability of full

length IpaB in the absence of its cognate chaperone IpgC (37, 42, 59, 63), we sought to identify a

soluble fragment of the translocator that would be more amenable to crystallographic analysis. Both IpaB and SipB contain a conserved central hydrophobic region that is predicted to form a single α-helical transmembrane hairpin (4, 42, 46, 59). It has also been shown that the region C-terminal to the hydrophobic domain contains membrane-binding properties (37, 42). Thus, it seemed likely that removal of this entire C-terminal region might yield a soluble, stable translocator fragment.

When purified, recombinant translocator/chaperone complexes were subjected to limited subtilisin digestion, protease resistant translocator fragments for both the IpaB/IpgC and SipB/SicA complexes were identified (**Fig. 22a, b**). Following separation by SDS-PAGE, the resulting fragments were characterized by LC-MS/MS analysis of their respective tryptic peptides (48). One such fragment corresponded to residues 28-226 of *S. flexneri* IpaB (**S3-103-4 in Fig. 22a**), while a similarly sized fragment was also observed for *S.* Typhimurium SipB (**S4-103-4 in Fig. 22b**). The fact that both fragments were derived from a closely overlapping area of distinct proteins supports our hypothesis that a largely stable and otherwise soluble domain is a conserved structural feature within the N-terminal region of these translocators. Indeed, recombinant forms of both IpaB$^{28.226}$ and SipB$^{30.237}$ were readily expressed in the absence of chaperone, and were found to be monodisperse in minimal buffers (as judged by both analytical gel-filtration chromatography and dynamic light scattering) even at concentrations greater than 5 mg/ml (~250μM) protein.

Crystal Structures of the IpaB and SipB Fragments Reveal a Structurally-conserved Intramolecular Coiled-Coil

Despite the encouraging physical properties and the apparent stability of IpaB$^{28.226}$, initial crystallization screening was unsuccessful. However, subsequent adventitious proteolytic degradation within the N-terminal region of IpaB$^{28.226}$ was observed, which yielded a readily crystallizable core consisting of residues 74–224. The structure of *S. flexneri* IpaB$^{74.224}$ was solved by MAD using a platinum derivatized crystal exposed to synchrotron X-rays at two wavelengths corresponding to Pt peak and remote energies (**Table 3**), and the final structure was refined to 2.1 Å
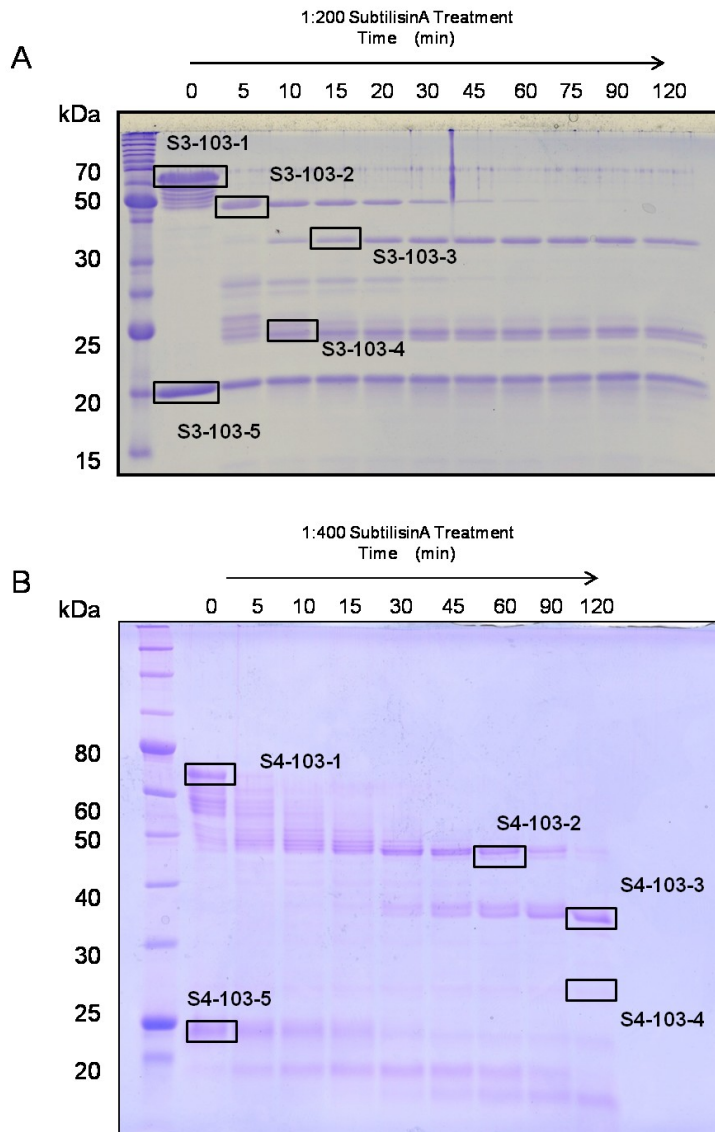
FIGURE 22. Limited Subtilisin Digest of Translocator/Chaperone Complexes. *A*, Full length class II chaperone, IpgC, was co-expressed with the full length first translocator, IpaB, from *Shigella flexneri*. Following IMAC purification, the translocator/chaperone complex was treated with subtilisin (1:200 substrate:enzyme ratio) for 120 min, with aliquots taken at various intervals. Samples were separated via SDS-PAGE and their tryptic peptides were identified by LC-MS/MS. The band identified as S3-103-4 was comprised of IpaB residues 28-226. *B*, Full length class II chaperone, SicA, was co-expressed with the full length first translocator, SipB, from *Salmonella* Typhimurium. Following IMAC purification, the translocator/chaperone complex was treated with subtilisin (1:400 substrate:enzyme ratio) for 120 min, with aliquots taken at various intervals. Samples were separated via SDS-PAGE and their tryptic peptides were identified by LC-MS/MS.

limiting resolution in the space group $P2_1$. The final model consists of two complete polypeptides (**Fig. 23a**) that are comprised of residues 74–224 (**Fig. 24**).

Similarly, the structure of *S.* Typhimurium SipB[82.226] was solved by MAD using crystals of Seleno-L-Methionine-labeled protein exposed to synchrotron X-rays at two wavelengths corresponding to Se peak and remote energies. The final model was refined to a 2.8 Å limiting resolution in the space group $P2_12_12$ and consisted of four polypeptides (**Fig. 23b**). While high-quality model/map correlation was observed for residues 82–122, 126–174 and 182–226 (**Fig. 25**), the electron density map corresponding to solvent exposed loop regions (i.e. residues 123-125 and 175-181) was too weak to model accurately. Interestingly, two of the four SipB polypeptides in the asymmetric unit exhibit different conformations within the 20 N-terminal residues of helix α1 (**Fig. 23c**). This region is characterized by a high degree of conformational flexibility and culminates in a 16.8 Å shift as measured from the carbonyl of Gly[83] within chains A and B. Such intrinsic flexibility is apparently absent from the IpaB crystal structure.

Both IpaB[74.224] and SipB[82.226] are almost entirely α-helical and are comprised of three anti-parallel helices compressed into an intramolecular coiled-coil tertiary structure (**Figs. 24 and 25**). It is interesting to note that previous structure-function analysis of IpaB and SipB predicted that the N-terminal regions of both IpaB (110-170) and SipB (180–216) would contain a coiled-coil domain (5, 34, 42); however, the predicted region is much smaller, and covers only a portion of the entire tertiary structure that is reported here. Interestingly, the latter part of the second and third helices of each structure (residues 104–224 and 126–226 for IpaB and SipB, respectively) display very strong structural identity with one another. Overall 93 of 94 Cα positions superimpose within 5.0 Å with an RMSD of 1.42 Å (**Fig. 26a**), which indicates that this coiled-coil is a conserved feature of these TTSS translocators. This occurs despite the fact that IpaB shares relatively low sequence identity (21%) to the corresponding residues 1-240 of SipB (**Fig. 26b**).
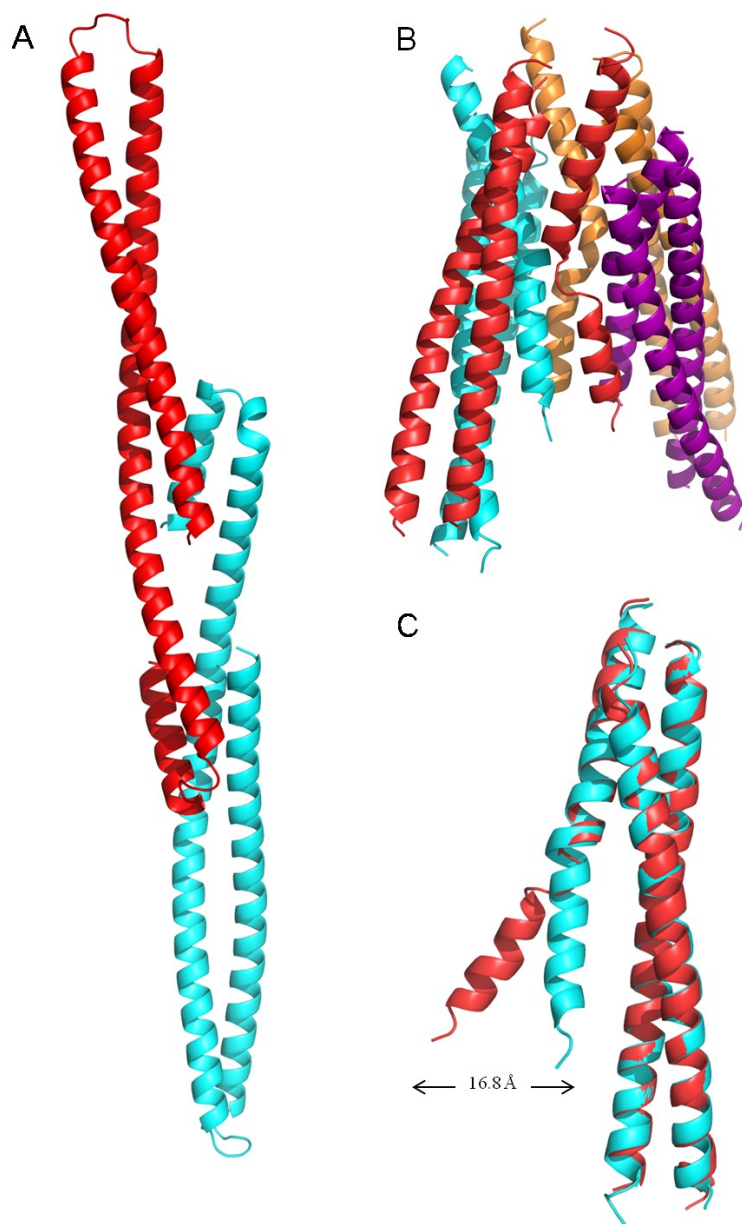
FIGURE 23. Refined IpaB and SipB Asymmetric Unit. *A,* Ribbon diagram of IpaB
asymmetric unit depicting 2 distinct polypeptides. *B*, Ribbon diagram of SipB asymmetric unit.
SipB polypeptides with conformationally rigid α1 are colored cyan and purple. *C*, Structural
superposition of chains A (cyan) and B (red) from panel B depicting the 16.8 Å N-terminal
movement (measurement from Gly83 carbonyl on each chain).
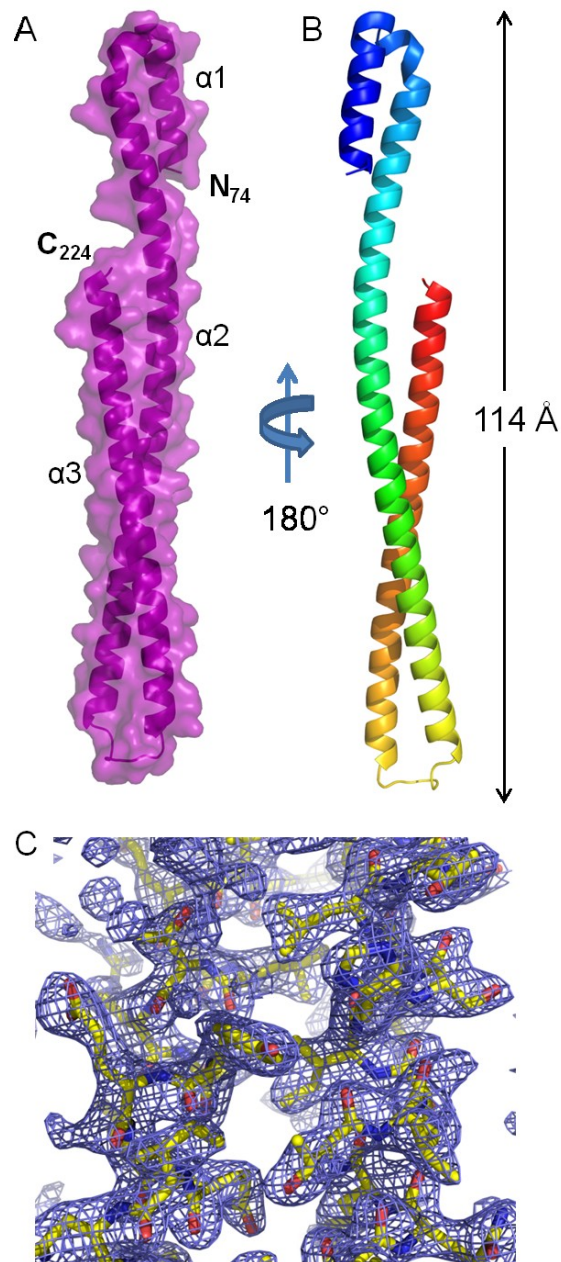
FIGURE 24. Crystal Structure of IpaB$^{74.224}$ at 2.1 Å Resolution. *A*, Crystal structure of *S. flexneri* IpaB (residues 74-224) shown in cartoon ribbon format surrounded by surface representation (colored purple). Two copies of each polypeptide are found within the asymmetric unit (single copy shown for clarity). *B*, Crystal structure rotated 180° about the long axis, colored blue (N-terminus) to red (C-terminus). *C*, Representative model-to-map correlation for IpaB$^{74.224}$; *2F$_o$-F$_c$* weighted electron density (contoured at 2.0 σ) is drawn as a blue cage around a region of the coiled-coil.

The small protein monomers that comprise the TTSA needle of diverse organisms themselves

consist of a helix-turn-helix motif that is essentially a short intramolecular coiled-coil (20, 79, 91, 97,

103). These monomers self-assemble into a superhelical bundle that forms the hollow, yet extended

TTSA needle characteristic of these various pathogens (20). Similarly, a longer intramolecular

coiled-coil is a highly conserved feature among the TTSA needle tip proteins from several families

of pathogens (29), where it appears to constitute a centralized structural scaffold. The fact that IpaD's

presence at the TTSA needle tip is also required for stable maintainence of IpaB following its initial

recruitment (67) suggests that these two proteins are likely to physically interact within the context of

the TTSA needle assembly. Conceivably this could be accomplished most readily through a nearly

parallel alignment of the tip protein and translocator coiled-coils in a manner similar to what has been

previously described for the TTSA needle protein monomers. In this regard, it is likely significant

that the coiled-coil domains of IpaB and SipB (residues 104–224 and 126–226, respectively) share a

high degree of structural identity with the central coiled-coil region of their respective tip proteins,

IpaD (RMSD of 2.47 Å over 101/121 Cα atoms within 5.0 Å) and SipD (RMSD of 2.39 Å over 88/94

Cα atoms within 5.0 Å) (**Fig. 27a, b**).

The IpaB/SipB Coiled-coil Domain is Related to Those of Pore-Forming Colicins

Despite their limited sequence conservation, the coiled-coil regions of IpaB (residues 104–

224) and SipB (residues 126–226) share a high level of structural identity with one another.

Furthermore, these intramolecular coiled-coils are reminiscent of the centralized helical scaffold

within TTSA needle tip proteins. Together, these observations raised questions as to whether this

structurally-conserved region of the TTSS first translocators might also be evolutionarily related to

other proteins. To this end, the refined coiled-coils of both IpaB[104.224] and SipB[126.226] were used to

search for structurally-related motifs within other proteins via the DALI server (40). Intriguingly,

many of the highest-quality matches were found with other proteins involved in membrane targeting

and/or insertion/pore-formation events (49, 88, 99, 100). In particular, colicin E3 (IpaB, Z-score =
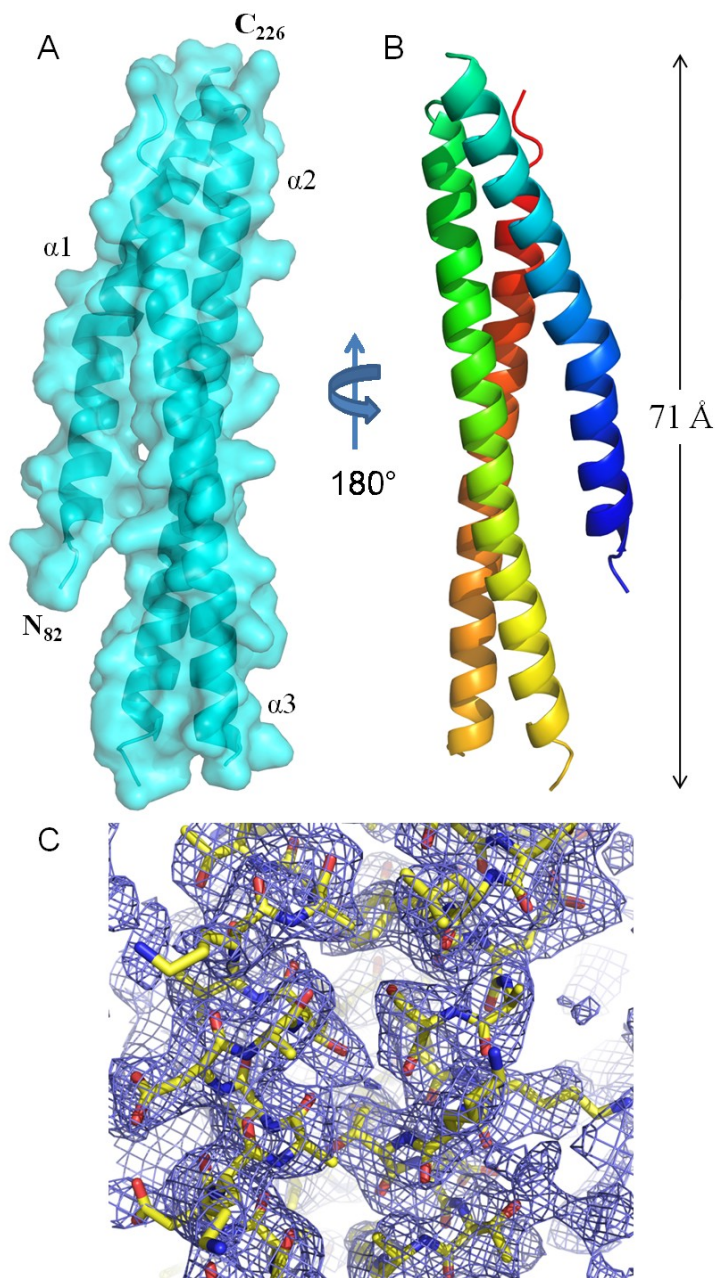
FIGURE 25. Crystal Structure of SipB$^{82.226}$ at 2.8 Å Resolution. *A*, Crystal structure of *S.* Typhimurium SipB (residues 82-226) shown in cartoon ribbon format surrounded by surface representation (colored cyan). Four copies of SipB are found within the asymmetric unit (single copy shown for clarity). *B*, crystal structure rotated 180° about the long axis; colored blue (N-terminus) to red (C-terminus). *C*, representative model-to-map correlation for SipB$^{82.226}$; *2F$_o$-F$_c$* weighted electron density (contoured at 1.5 σ) is drawn as a blue cage around a region of the coiled-coil.
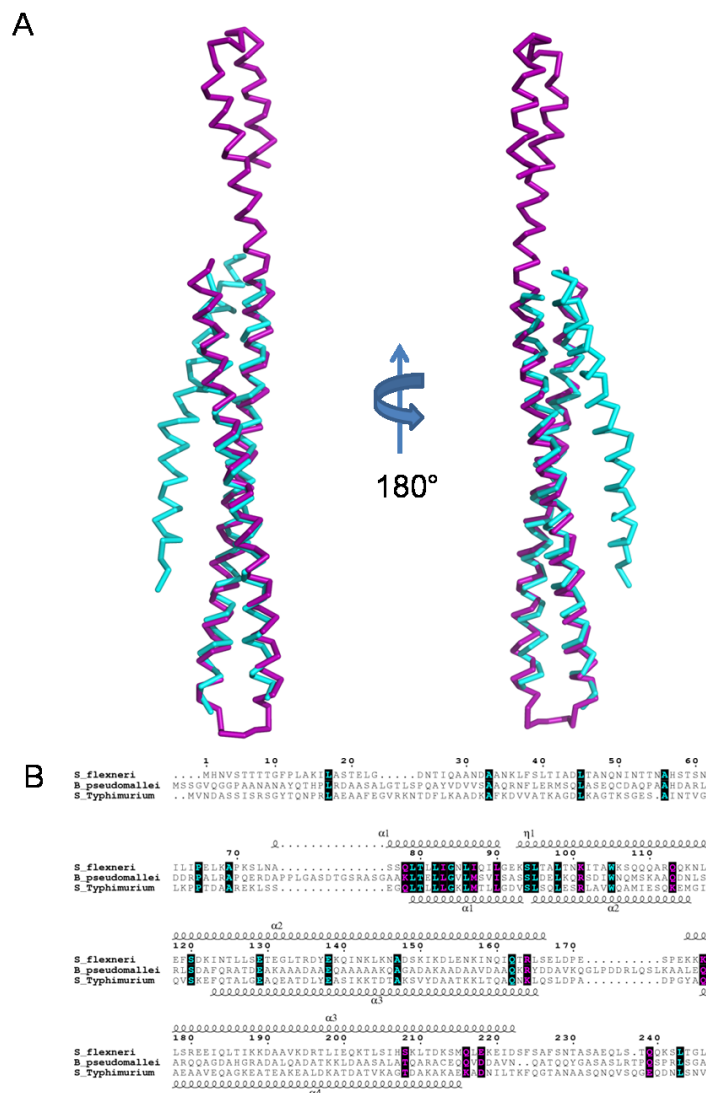
FIGURE 26. Structural Superposition of Translocator Coiled-coils. *A,* Ribbon diagram of a structural alignment of the coiled-coils from IpaB (residues 120-224, purple) and SipB (residues 126-226, cyan) with an RMSD of 1.42 Å over 93/94 Cα atoms within 5.0 Å, rotated 180° about the long axis. Although the overall topology of both structures is similar, there are differences within the N-terminal region spanning the first helix (α1) and turn as well as the length of the second helix (α2). Such differences within the N-terminus of the structures reported here could be reflective of the apparent instability of the chaperone binding domains (CBD) in the absence of their cognate chaperones. *B,* Limited structure-based sequence alignment of type III secretion first translocators (residues 1–240) colored according to residue conservation (cyan=absolute and purple=similar) as judged by the BLOSUM62 matrix. Alignment was generated using ClustalW and rendered with ESPRIPT. Numbers above the sequences correspond to *S. flexneri* IpaB. Secondary structure elements of IpaB and SipB are shown above and below the alignment, respectively.

9.7, RMSD of 2.03 Å over 118/121 Cα atoms; SipB, Z-score = 8.0, RMSD of 1.19 Å over 92/94 Cα atoms) and colicin Ia (IpaB, Z-score = 10.2, RMSD of 1.73 Å over 121/121 Cα atoms; SipB, Z-score = 10.1, RMSD of 1.21 Å over 93/94 Cα atoms) were among the highest scoring matches emanating from this search (**Fig. 28a, b**). Both of these colicins contain extended-length coiled-coil motifs (160 Å for colicin Ia and 100 Å for colicin E3) within their receptor domains. In all of these cases, the coiled-coil domains are responsible for spanning long distances with the purpose of mediating a contact dependent function, notably obtaining access to or transversing a membrane barrier (39, 49, 88, 99). At a fundamental level, this appears to be directly in line with a critical function already ascribed to TTSS first translocator proteins.

Discussion

S. flexneri and *S.* Typhimurium use the TTSS to promote entry into both macrophages and epithelial cells (84). Through the investigation of the *Shigella* TTSA we have been able to demonstrate that the mature needle tip complex is assembled in a stepwise manner. Initially, IpaD localizes to the needle tip where it controls secretion and represents completion of the assembly of the nascent TTSA needle tip complex (30). Interaction of IpaD with environmental small molecules such as host bile salts results in recruitment of IpaB to the needle tip representing a maturation of the tip complex into a form that detects host cell contact (90). Finally, IpaB interacts with liposomes, preferentially those containing cholesterol and sphingomyelin, which mimic the host cell membrane. This ultimately leads to the recruitment of IpaC to the distal end of the needle complex (28). Yet despite this substantial level of mechanistic detail, our understanding of this process at a molecular level has hampered by the lack of structural information on the translocators, IpaB and IpaC.

Overcoming the initial solubility and stability issues associated with full-length translocators has allowed us to present here the first high-resolution structural data for a TTSS translocator protein. The N-terminal regions of IpaB and SipB, from *S. flexneri* and *S.* Typhimurium, respectively, display
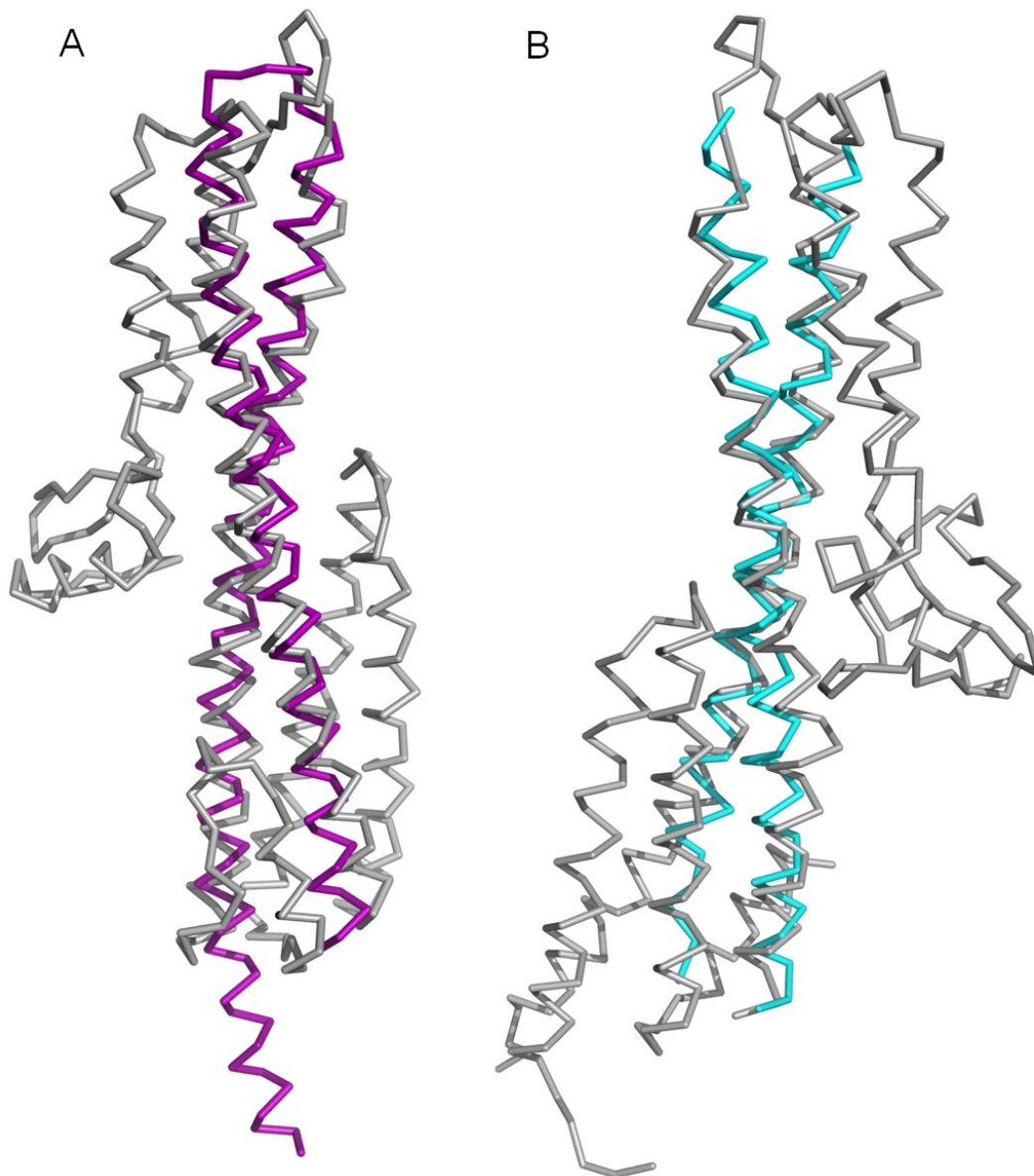
FIGURE 27. Structural Alignment of Type Three Secretion Protein Coiled-coils. *A,* ribbon diagram of a structural alignment of IpaD (residues 39-322, grey) and IpaB (residues 104-224, purple) with an RMSD of 2.47 Å over 101/121 Cα atoms within 5.0 Å. *B,* ribbon diagram of a structural alignment of SipD (residues 36-342, grey) and SipB (residues 126-226, cyan) with an RMSD of 2.39 Å over 88/94 Cα atoms within 5.0 Å.
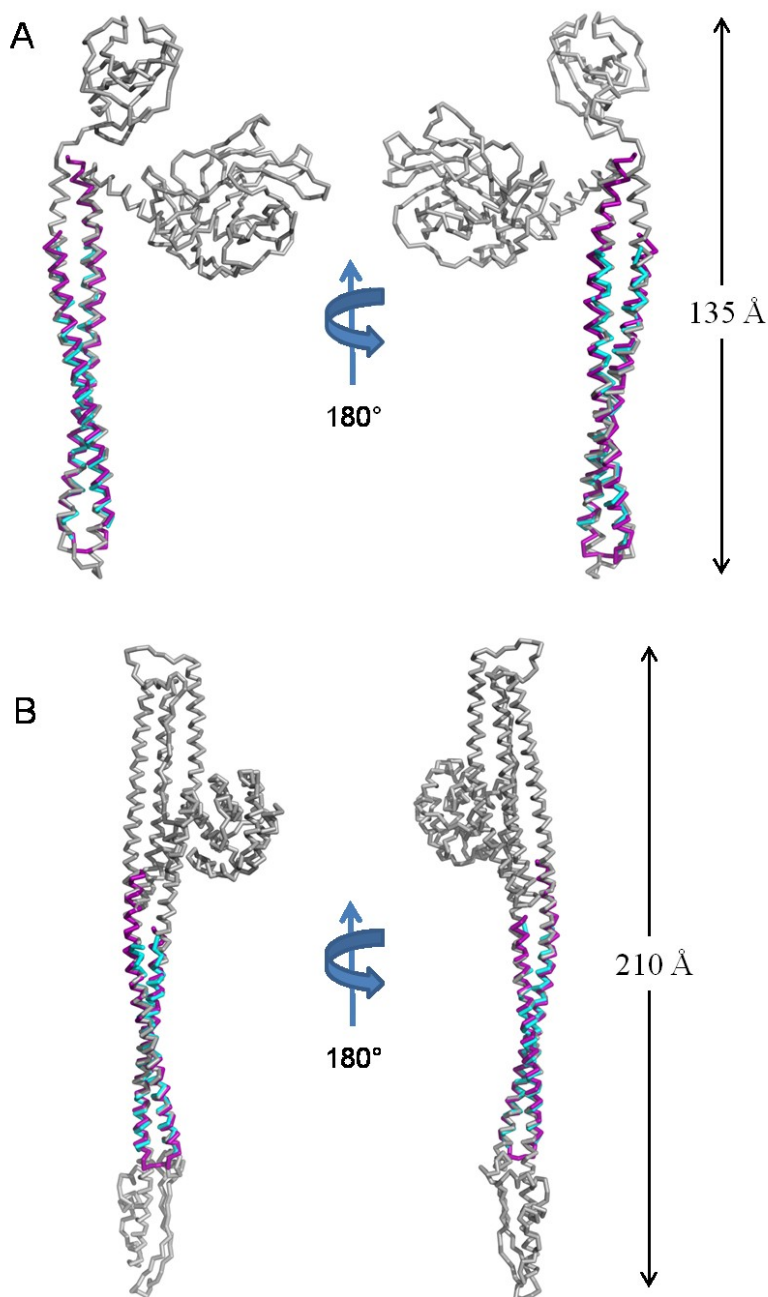
FIGURE 28. Coiled-coil Homology with Pore-forming Proteins. *A*, ribbon diagram of IpaB (residues 104-224, purple) and SipB (residues 126-226, cyan) superposed over *Escherichia coli* Colicin E3 (colored grey; PDB code= 1JCH) with an RMSD of 2.03 Å over 118/121 Cα atoms for IpaB and an RMSD of 1.19 Å over 92/94 Cα atoms for SipB. Crystal structures rotated 180° about the long axis. *B*, ribbon diagram of IpaB (residues 104-224, purple) and SipB (residues 126-226, cyan) superposed over *Escherichia coli* Colicin Ia (colored grey; PDB code= 1CII) with an RMSD of 1.73 Å over 121/121 Cα atoms for IpaB and an RMSD of 1.21 Å over 93/94 Cα atoms for SipB. Crystal structures rotated 180° about the long axis.

strong structural homology to one another while consisting almost entirely of a coiled-coil motif. Additionally, we have identified a significant structural homology between this portion of IpaB and SipB and the centralized coiled-coil of the TTSS tip proteins. This suggests, albeit indirectly, that this region of the first translocator is responsible for the previously reported stable interaction with its cognate tip protein (67). Finally, and perhaps most strikingly, we have shown that the most closely related structures to the coiled-coils of IpaB and SipB are pore-forming and/or membrane associated proteins from the colicin family. This is consistent with a general view within the field that the first translocator protein not only interacts with the target host cell membrane, but also forms a pore as well.

The structural homology shared between the needle monomers, tip proteins, and the N-terminal translocator fragments presented here further underscores the general importance of intramolecular coiled-coils as structural scaffolds within TTS proteins (22). While much work clearly remains to be done (particularly in terms of the remaining regions of IpaB and SipB), these initial structures provide an attractive starting point for understanding the mechanism of matured translocon formation. We believe that the increasing lengths of the coiled-coil structures in MxiH/PrgI, IpaD/SipD and the extreme length of the coiled-coils presented here (114 Å in *Shigella* and 71 Å in *Salmonella*) may allow the putative pore-forming hydrophobic domain of the first translocators to properly oligomerize above the IpaD/SipD-based tip complex. In this position, the assembled translocator multimer can sense host contact via interactions with lipids. Such an interaction would be responsible for concomitant recruitment of the second translocator, IpaC, to the TTSA needle tip, and thus facilitate needle insertion into the host cell membrane (28). It is interesting to note, then, that IpaC is also predicted to contain a coiled-coil (22, 52); by analogy, this domain might interact directly with the coiled-coil region indentified here within the first translocator, IpaB. Once the mature tip complex (IpaD-IpaB-IpaC in *Shigella*, SipD-SipB-SipC in *Salmonella*) has thus

been assembled, full-scale translocation of effectors can then commence, which signals the beginning of TTSS-dependent cellular invasion.

During the course of analyzing the crystal structures presented here, we made the surprising observation that the structures most closely related to the IpaB and SipB coiled-coils are found in either pore-forming or membrane-associated proteins from the colicin family. Colicins comprise a diverse series of bacteriocidal toxins that exert their various activities through an array of distinct mechanisms, such as formation of transmembrane pores formation and DNA cleavage through a potent intrinsic nuclease activity (49, 100). Yet despite the significant differences in their precise bacteriocidal activities, the initial movement of colicins across the target bacterial cell membrane systems appears to be accomplished by a largely similar mechanism (49). For colicin Ia, which is the most similar protein to the coiled-coil region of both IpaB and SipB, recognition of an outer membrane receptor by a region at one end of its long coiled-coil allows a translocation domain to promote access of the protein to the periplasmic space of the target bacterium (32, 99). While still anchored to the outer membrane receptor, the coiled-coil allows the apparently unstructured translocation domain to interact with and insert into target membrane-bound components. Considering their structural homology to members of the colicin family, we can now begin to make larger-scale proposals relevant to TTSS first translocator function. In this regard, it seems very likely that the extended N-terminal coiled-coil domains of IpaB and SipB serve a similar role in both anchoring the first translocators to the IpaD/SipD-based TTSA needle tip complex and placing their respective hydrophobic domains in a position where recognition of and penetration into a target host cell plasma membrane can occur. This would not only maintain IpaB/SipB as a stable component of the maturing TTSA needle tip complex, but also ensure that the energized conduit which is the TTSA remains contiguous.

The structures of the first translocator N-terminal fragments presented here cover approximately 25% of these proteins' sequence. However, they do not provide direct information on

the C-terminal half of these proteins, which contribute to their critical pore-forming structures (4, 46).

The Fold and Function Assignment Server (FFAS) utilizes comparisons between sequences of interest and proteins of known function to then make structural predictions for the sequences of interest (43). When we used FFAS to query the PDB with sequences that correspond to the putative α-helical hairpin regions spanning residues 310-370 of IpaB (34, 42) and residues 320-380 of SipB (37, 42, 59), a region within the pore-forming domain of colicin Ia (residues 579-611) was identified. The pore-forming domain of colicin Ia is comprised of its C-terminal 176 residues, and consists of 10 α-helices arranged in a bundle-type structure (**Fig. 29**) that is similar to other colicin pore-forming domains (39, 99). Perhaps most significantly, the precise region identified by FFAS also corresponds to the hydrophobic helical hairpin that is responsible for anchoring the colicin pore within the host lipid bilayer (100). Thus, while the structural identity between the IpaB and SipB coiled-coils and members of the colicin family is clear, bioinformatic tools suggest that there may be even further relationships between these two groups of proteins.
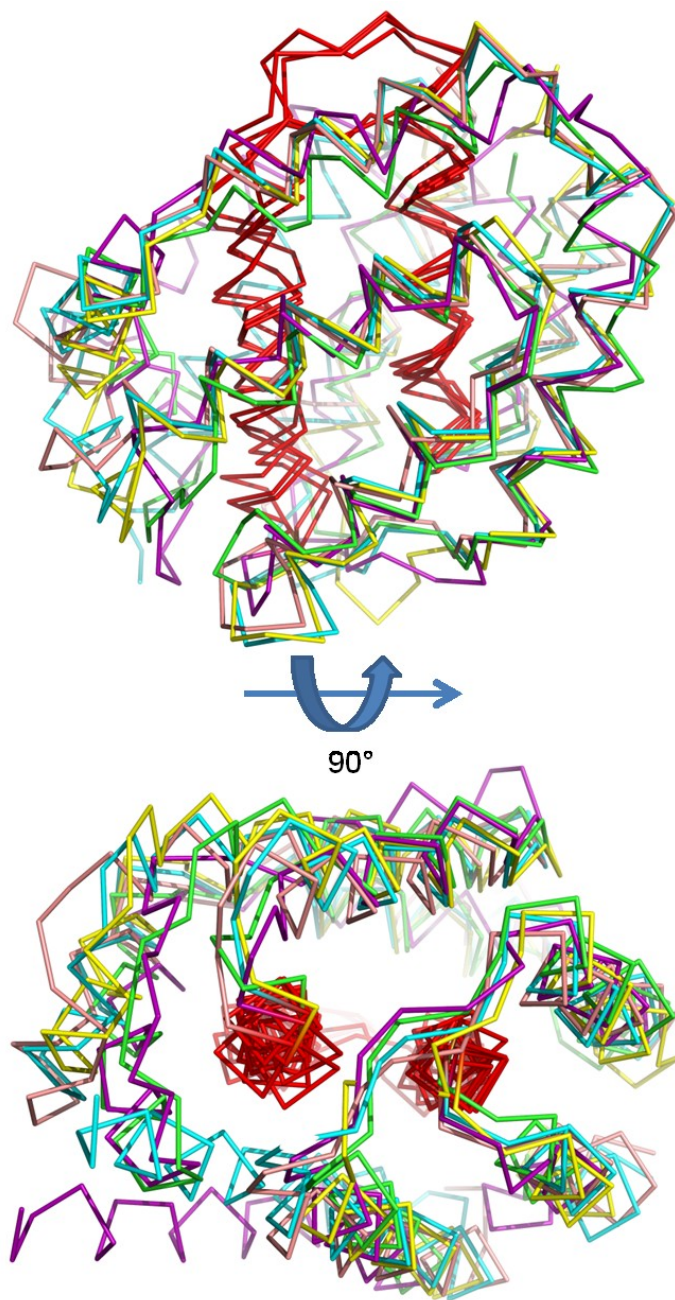
FIGURE 29. Structural Superposition of Colicin Pore-forming Domains. Ribbon diagrams of the structural superposition of the pore-forming domain from Colicins Ia (green, PDB code: 1CII), E1 (purple, 2I88), N (yellow, 1A87), A (cyan, 1COL) and B (pink, 1RH1). Highlighted in red is the hydrophobic α-helical hairpin responsible for anchoring the pore forming domain in the host lipid bilayer. Crystal structures are rotated 90° downward about the central axis of the hairpin on the right.

CHAPTER 6

GLOBAL DISCUSSION

In the last several years, two separate studies have reported the crystal structures of class II

chaperones bound to peptide fragments of TTSS translocator proteins. Even though the structures of

IpgC$^{1-151}$-IpaB (55) and PcrH$^{21-160}$-YopD (44) are meant to mimic recognition of separate classes of

full-length translocator proteins from two distinct organisms, both structures reveal that the

translocator peptide lies within a groove found on the concave TPR "hand" of the chaperone. This

indicates that their mechanism of translocator/ligand recognition is similar, despite the fact that the

quaternary structures appear to differ considerably between IpgC$^{1-151}$ and PcrH$^{21-160}$. The significant

differences between the "head-to-head" dimer observed in both SycD$^{21-163}$ (13) and PcrH$^{21-160}$ (44)

with the asymmetric structure of IpgC$^{1-151}$ raise important questions regarding the precise nature of

class II chaperone dimers in the physiological setting. Further complicating this issue are the cogent

biophysical, biochemical, and/or functional data which support each of these crystal structures.

Our observation that a single TTSS chaperone can adopt two distinct quaternary

arrangements suggests that both the asymmetric and head-to-head dimers may have important

physiological roles in bacterial TTSSs. As stated earlier, IpgC has the ability to bind two separate

translocator proteins, IpaB and IpaC (7), as well as the AraC-family transcription factor, MxiE (76).

The ability of IpgC to bind each of these proteins is regulated by the secretion state of the *S. flexneri*

cell (84). Secretion of both IpaB and IpaC through the TTSA needle liberates IpgC, and allows it to

interact with MxiE; this culminates in the expression of the late effectors (57). It is believed that an

amino terminal secretion signal targets effectors to the secretion system and that chaperones may also
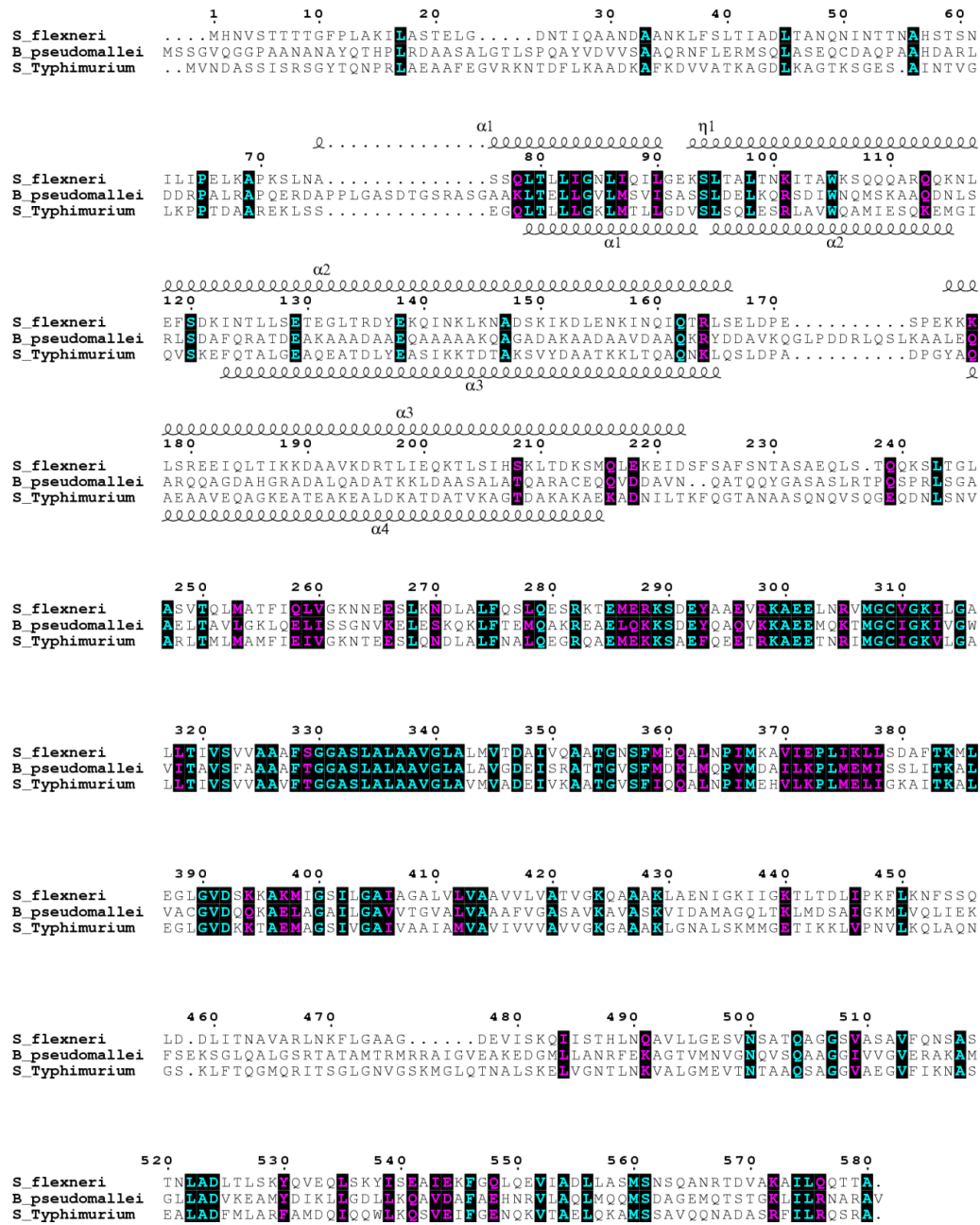
FIGURE 30. Inv-Mxi-Spa TTS Translocator Sequence Alignment. Sequence alignment of animal pathogen type III secretion first translocators from *S. flexneri, B. pseudomallei* and *S.* Typhimurium colored according to residue conservation (cyan = absolute, purple = similar). Alignment was generated using ClustalW and rendered with ESPRIPT. Numbers above the sequences correspond to *S. flexneri* IpaB. Secondary structure elements of IpaB and SipB are shown above and below the alignment, respectively.

be involved in guidance of their complexes to the base of the TTSA needle (57). The potential switch in quaternary structure of IpgC may therefore be involved with its ability to effectively bind or deliver translocators to the secretion system. For example, though both types of chaperone dimer are competent to bind peptide mimics of their translocator targets, a change in dimerization state might alter the stoichiometry of various chaperone/ligand complexes within the context of full-length proteins. Addressing this possibility will require more thorough characterization of translocator proteins, such as IpaB and IpaC, for which little tertiary structural information is currently available. Presented within these studies, are the crystal structures of the N-terminal coiled-coil domains of IpaB and SipB, the S. Typhimurium translocator homolog. Structural characterization of these domains bound to IpgC dimers in both quaternary states could reveal the shift in dimerization interfaces to be structural in nature. Along these lines, IpgC could also transition between asymmetric and symmetric dimerization modes to accommodate its broad range of interaction partners. Because the change in dimerization appears to correlate with a loss of amino acids at the amino terminus of IpgC, an ordered proteolytic event in this region might trigger a change in quaternary structure that affects IpgC function. Whether such a transition could result in a change in the role of IpgC from secretion chaperone to transcriptional coactivator remains to be determined. In any case, additional studies will be needed to explore the potential roles of both modes of class II chaperone dimerization in the *Shigella* TTSS as well as that from other pathogens.

When viewed at first glance, it would be tempting to speculate that the ligand-binding mode identified for IpaD is more relevant than the previously discussed SipD binding studies because it is supported by a previous series of *in vitro* binding studies (90). However, it is critical to realize that *Salmonella* respond much differently to bile salts than do *Shigella* (78). Chief amongst these differences are that bile salts mediate repression of the TTSS that includes SipD and PrgI (i.e. the needle protein) (97) and that short incubation in the presence of DOC causes rapid loss of *Salmonella* invasiveness for cultured cells (unpublished results). Curiously, there exists a high degree of

structural conservation between both the tip proteins (IpaD and SipD) (45) and the needle proteins (MxiH and PrgI) (19, 97) from these two organisms. This suggests that the needle-tip protein interaction is likely to be conserved as well, even though the surface electrostatic features of MxiH and PrgI differ significantly. Thus, while it cannot be ruled out whether different electrostatic properties play a role, it is reasonable to suggest that the difference in binding modes across TTSS-possessing organisms might ultimately give rise to pathogen-specific responses to the same bile salts. In any case, it is clear that fundamental differences in TTSA function exist between these two closely related organisms, and that additional work will be needed to dissect the molecular level changes that occur in response to bile-salts by TTSAs from other bacterial species (14).

Previous solution dynamics experiments along with the crystalline state studies presented here have allowed for a comprehensive analysis of IpaD structural changes that correlate with its binding to bile salts. This has permitted well-informed mutagenesis and phenotypic analysis of what appears to be the first discrete step in TTS activation in *Shigella*, and also provided a framework for developing a testable model of this critical process. This initial step is characterized by the recruitment and stable binding of the first translocator protein, IpaB, to the maturing TTSA needle tip complex. At the tip of the nascent TTSA needle, IpaD is able to sense environmental small molecules such as bile salts that associate with the protein and thereby bind to the needle. The resulting change in IpaD structure perturbs the interaction between the tip complex and the needle itself, giving rise to a conformational signal that brings IpaB to the tip without further type III secretion. How this signal is processed by the apparatus is not clear; however, it could involve interactions between IpaD and IpaB, which is itself located within the needle prior to recruitment (67). This would fit with the previous observation that while we do not detect IpaB on the surface of *S. flexneri* SF622 expressing wild-type IpaD, we can detect it by immunoblot analysis of isolated needles. Alternatively, it is possible that the DOC-stabilized structural transition at the needle tip is relayed through the polymerized needle monomers and then detected by the TTSA base. This would be consistent with

previous studies which showed that point mutations within MxiH can lead to altered secretion status (47). While there are still unanswered questions, this report provides a sound starting point for determining the mechanism of type III secretion induction in *Shigella*.

In the past, approaches based around biochemical characterization of gene deleted strains and comparative analysis of operon structures have proven instrumental in the identification of novel TTSSs from diverse gram-negative bacteria. Yet despite their many similarities at a functional level, analyses based upon sequence conservation alone have not played as significant a role in fostering understanding of various TTSSs - particularly for the Inv-Mxi-Spa TTSS family that is shared between *Shigella*, *Salmonella*, and *Burkholderia* spp. Within this context, the IpaB and SipB translocators of the Inv-Mxi-Spa TTSS family possess a relatively low level of sequence conservation within their N-terminal 240 residues (**Fig. 30**); however, as we have shown here, there exists a telling level of structural identity within this region, but one that required a biochemical mapping approach to identify. Thus, even though regions of these TTSS components may be diverging rapidly at the sequence level, it seems that there is strong selective pressure to maintain the coiled-coil structure within the N-terminal region of the first translocators. Intriguingly, this level of structural conservation appears to be shared between TTSS first translocators and members of the colicin family that likewise appear to have related membrane targeting and/or penetrating functions (100). At a fundamental level, this "shared structure, but low sequence homology" relationship that conclusively links TTSSs to bacteriocins has broad implications for creating and understanding protein family phylogenies.

Because of the essential role of first translocators in type III secretion, the data presented here represent an important step forward which will allow detailed mechanistic dissection of the delivery of effectors to host cells. As importantly, because IpaB, and presumably SipB, is surface exposed prior to host cell contact, they represent potentially valuable targets for vaccine development. Multidrug resistant strains of all *Shigella* spp. are found throughout the underdeveloped world. These

strains are all resistant to common 'first-line' antibiotics, with resistance to new-generation antibiotics spreading at a fast rate (74). Thus, control of shigellosis appears limited to vaccine development, of which limited success has currently been obtained (50, 53). Since current vaccines against these pathogens are serotype specific, the development of IpaB and SipB (or defined regions thereof) into subunit-based vaccines could provide highly sought after heterologous protection among various serovars. As a result, the structures presented here provide valuable information on not only the mechanism of the first translocator's role in TTSS-related disease, but may also suggest a plausible and attractive route to prevention of these diseases in the first place.

IpaB is arguably the centerpiece for transition of the *Shigella* TTSA from a quiescent to an induced secretion state. In this central role, it spends its entire existence in partnership with a series of equally important virulence proteins. Prior to secretion through the TTSA, interaction with both IpaC and other IpaB polypeptides is prevented by interaction with IpgC. Maturation of the tip complex (IpaD-MxiH-IpaB) proceeds in a step-wise manner. Prior to interacting with environmental bile salts, such as DOC, IpaD forms a multimeric plug, preventing premature effector secretion and maintaining IpaB within the needle channel. Upon recruitment to the needle tip, IpaB interacts with the C-terminal distal domain of IpaD, forming a stable multimer that is able to recognize membrane-bound host lipids. This action recruits the second translocator, IpaC, and concomitantly initiates *Shigella* invasion via the formation of an oligomeric translocon pore. Indeed, these studies have revealed the implications of coiled-coils and anti-parallel helical bundles in the formation of the polymerized needle, multimeric tip complex and individual subunits of the translocon pore. At each step of needle complex maturation, α-helical interactions are integral as scaffolds for stable interaction and progression towards the host epithelial membrane. Understanding the mechanism used by *Shigella* to move IpaB from its chaperone-bound state in the cytoplasm to another macromolecular complex at the tip of the TTSA needle, of which these studies have provided a great starting point, will have global applications to all TTSSs.

REFERENCES

1. 1994. The CCP4 Suite: Programs for Protein Crystallography, p. 760-763. vol. D50. Acta Crystallography.

2. **Adams, P., R. Grosse-Kunstleve, L. Hung, T. Ioerger, A. McCoy, N. Moriarty, R. Read, J. Sacchettini, N. Sauter, and T. Terwilliger.** 2002. PHENIX: building new software for automated crystallographic structure determination. Acta Crystallogr D Biol Crystallogr **58:**1948-1954.

3. **Barta, M. L., L. Zhang, W. L. Picking, and B. V. Geisbrecht.** 2010. Evidence for alternative quaternary structure in a bacterial Type III secretion system chaperone. BMC Struct Biol **10:**21.

4. **Baudry, B., M. Kaczorek, and P. J. Sansonetti.** 1988. Nucleotide sequence of the invasion plasmid antigen B and C genes (ipaB and ipaC) of Shigella flexneri. Microb Pathog **4:**345-357.

5. **Berger, B., D. B. Wilson, E. Wolf, T. Tonchev, M. Milla, and P. S. Kim.** 1995. Predicting coiled coils by use of pairwise residue correlations. Proc Natl Acad Sci U S A **92:**8259-8263.

6. **Bernardini, M. L., J. Mounier, H. d'Hauteville, M. Coquis-Rondon, and P. J. Sansonetti.** 1989. Identification of icsA, a plasmid locus of Shigella flexneri that governs bacterial intra- and intercellular spread through interaction with F-actin. Proc Natl Acad Sci U S A **86:**3867-3871.

7. **Birket, S., A. Harrington, M. Espina, N. Smith, C. Terry, N. Darboe, A. Markham, C. Middaugh, W. Picking, and W. Picking.** 2007. Preparation and characterization of translocator/chaperone complexes and their component proteins from Shigella flexneri. Biochemistry **46:**8128-8137.

8. **Blocker, A., P. Gounon, E. Larquet, K. Niebuhr, V. Cabiaux, C. Parsot, and P. Sansonetti.** 1999. The tripartite type III secreton of Shigella flexneri inserts IpaB and IpaC into host membranes. J Cell Biol **147:**683-693.

9. **Blocker, A., N. Jouihri, E. Larquet, P. Gounon, F. Ebel, C. Parsot, P. Sansonetti, and A. Allaoui.** 2001. Structure and composition of the Shigella flexneri "needle complex", a part of its type III secreton. Mol Microbiol **39:**652-663.

10. **Boggon, T. J., and L. Shapiro.** 2000. Screening for phasing atoms in protein crystallography. Structure **8:**R143-149.

11. **Brinkmann, V., U. Reichard, C. Goosmann, B. Fauler, Y. Uhlemann, D. S. Weiss, Y. Weinrauch, and A. Zychlinsky.** 2004. Neutrophil extracellular traps kill bacteria. Science **303:**1532-1535.

12. **Brøns-Poulsen, J., J. Nøhr, and L. Larsen.** 2002. Megaprimer method for polymerase chain reaction-mediated generation of specific mutations in DNA. Methods Mol Biol **182:**71-76.

13. **Büttner, C., I. Sorg, G. Cornelis, D. Heinz, and H. Niemann.** 2008. Structure of the Yersinia enterocolitica type III secretion translocator chaperone SycD. J Mol Biol **375:**997-1012.

14. **Chatterjee, S., D. Zhong, B. A. Nordhues, K. P. Battaile, S. Lovell, and R. N. De Guzman.** 2011. The crystal structures of the Salmonella type III secretion system tip protein SipD in complex with deoxycholate and chenodeoxycholate. Protein Sci **20:**75-86.

15. **Chen, H., D. Ricklin, M. Hammel, B. L. Garcia, W. J. McWhorter, G. Sfyroera, Y. Q. Wu, A. Tzekou, S. Li, B. V. Geisbrecht, V. L. Woods, and J. D. Lambris.** 2010. Allosteric inhibition of complement function by a staphylococcal immune evasion protein. Proc Natl Acad Sci U S A **107:**17621-17626.

16. **Cordes, F. S., K. Komoriya, E. Larquet, S. Yang, E. H. Egelman, A. Blocker, and S. M. Lea.** 2003. Helical structure of the needle of the type III secretion system of Shigella flexneri. J Biol Chem **278:**17103-17107.

17. **Cornelis, G. R.** 2006. The type III secretion injectisome. Nat Rev Microbiol **4:**811-825.

18. **Cui, J., and R. L. Somerville.** 1993. The TyrR protein of Escherichia coli, analysis by limited proteolysis of domain structure and ligand-mediated conformational changes. J Biol Chem **268:**5040-5047.

19. **Darboe, N., R. Kenjale, W. L. Picking, W. D. Picking, and C. R. Middaugh.** 2006. Physical characterization of MxiH and PrgI, the needle component of the type III secretion apparatus from Shigella and Salmonella. Protein Sci **15:**543-552.

20. **Deane, J. E., P. Roversi, F. S. Cordes, S. Johnson, R. Kenjale, S. Daniell, F. Booy, W. D. Picking, W. L. Picking, A. J. Blocker, and S. M. Lea.** 2006. Molecular model of a type III secretion system needle: Implications for host-cell sensing. Proc Natl Acad Sci U S A **103:**12529-12533.

21. **del Sol, A., C. J. Tsai, B. Ma, and R. Nussinov.** 2009. The origin of allosteric functional modulation: multiple pre-existing pathways. Structure **17:**1042-1050.

22. **Delahay, R. M., and G. Frankel.** 2002. Coiled-coil proteins associated with type III secretion systems: a versatile domain revisited. Mol Microbiol **45:**905-916.

23. **DeLano, W. L.** 2002, posting date. The PyMOL Molecular Graphics System. DeLano Scientific. [Online.]

24. **Dickenson, N. E., L. Zhang, C. R. Epler, P. R. Adam, W. L. Picking, and W. D. Picking.** 2010. Conformational Changes in IpaD from Shigella flexneri upon Binding Bile Salts Provide Insight into the Second Step of Type III Secretion. Biochemistry.

25. **DuPont, H. L., M. M. Levine, R. B. Hornick, and S. B. Formal.** 1989. Inoculum size in shigellosis and implications for expected mode of transmission. J Infect Dis **159:**1126-1128.

26. **Emsley, P., and K. Cowtan.** 2004. Coot: model-building tools for molecular graphics. Acta Crystallogr D Biol Crystallogr **60:**2126-2132.

27. **Emsley, P., B. Lohkamp, W. G. Scott, and K. Cowtan.** 2010. Features and development of Coot. Acta Crystallogr D Biol Crystallogr **66:**486-501.

28. **Epler, C. R., N. E. Dickenson, A. J. Olive, W. L. Picking, and W. D. Picking.** 2009. Liposomes recruit IpaC to the Shigella flexneri type III secretion apparatus needle as a final step in secretion induction. Infect Immun **77:**2754-2761.

29. **Espina, M., S. F. Ausar, C. R. Middaugh, M. A. Baxter, W. D. Picking, and W. L. Picking.** 2007. Conformational stability and differential structural analysis of LcrV, PcrV, BipD, and SipD from type III secretion systems. Protein Sci **16:**704-714.

30. **Espina, M., A. J. Olive, R. Kenjale, D. S. Moore, S. F. Ausar, R. W. Kaminski, E. V. Oaks, C. R. Middaugh, W. D. Picking, and W. L. Picking.** 2006. IpaD localizes to the tip of the type III secretion system needle of Shigella flexneri. Infect Immun **74:**4391-4400.

31. **Geisbrecht, B., S. Bouyain, and M. Pop.** 2006. An optimized system for expression and purification of secreted bacterial proteins. Protein Expr Purif **46:**23-32.

32. **Ghosh, P., S. F. Mel, and R. M. Stroud.** 1994. The domain structure of the ion channel-forming protein colicin Ia. Nat Struct Biol **1:**597-604.

33. **Gouet, P., E. Courcelle, D. Stuart, and F. Métoz.** 1999. ESPript: analysis of multiple sequence alignments in PostScript. Bioinformatics **15:**305-308.

34. **Guichon, A., D. Hersh, M. R. Smith, and A. Zychlinsky.** 2001. Structure-function analysis of the Shigella virulence factor IpaB. J Bacteriol **183:**1269-1276.

35. **Hammel, M., G. Sfyroera, D. Ricklin, P. Magotti, J. D. Lambris, and B. V. Geisbrecht.** 2007. A structural basis for complement inhibition by Staphylococcus aureus. Nat Immunol **8:**430-437.

36. **Hayward, R. D., R. J. Cain, E. J. McGhie, N. Phillips, M. J. Garner, and V. Koronakis.** 2005. Cholesterol binding by the bacterial type III translocon is essential for virulence effector delivery into mammalian cells. Mol Microbiol **56:**590-603.

37. **Hayward, R. D., P. J. Hume, E. J. McGhie, and V. Koronakis.** 2002. A Salmonella SipB-derived polypeptide blocks the 'trigger' mechanism of bacterial entry into eukaryotic cells. Mol Microbiol **45:**1715-1727.

38. **He, S. Y., K. Nomura, and T. S. Whittam.** 2004. Type III protein secretion mechanism in mammalian and plant pathogens. Biochim Biophys Acta **1694:**181-206.

39. **Hilsenbeck, J. L., H. Park, G. Chen, B. Youn, K. Postle, and C. Kang.** 2004. Crystal structure of the cytotoxic bacterial protein colicin B at 2.5 A resolution. Mol Microbiol **51:**711-720.

40. **Holm, L., and P. Rosenström.** 2010. Dali server: conservation mapping in 3D. Nucleic Acids Res **38:**W545-549.

41. **Huang, S. G.** 2003. Limited proteolysis reveals conformational changes in uncoupling protein-1 from brown adipose tissue mitochondria. Arch Biochem Biophys **420:**40-45.

42. **Hume, P. J., E. J. McGhie, R. D. Hayward, and V. Koronakis.** 2003. The purified Shigella IpaB and Salmonella SipB translocators share biochemical properties and membrane topology. Mol Microbiol **49:**425-439.

43. **Jaroszewski, L., L. Rychlewski, Z. Li, W. Li, and A. Godzik.** 2005. FFAS03: a server for profile--profile sequence alignments. Nucleic Acids Res **33:**W284-288.

44. **Job, V., P. Mattei, D. Lemaire, I. Attree, and A. Dessen.** 2010. Structural basis of chaperone recognition of type III secretion system minor translocator proteins. J Biol Chem.

45. **Johnson, S., P. Roversi, M. Espina, A. Olive, J. E. Deane, S. Birket, T. Field, W. D. Picking, A. J. Blocker, E. E. Galyov, W. L. Picking, and S. M. Lea.** 2007. Self-chaperoning of the type III secretion system needle tip proteins IpaD and BipD. J Biol Chem **282:**4035-4044.

46. **Kaniga, K., S. Tucker, D. Trollinger, and J. E. Galán.** 1995. Homologs of the Shigella IpaB and IpaC invasins are required for Salmonella typhimurium entry into cultured epithelial cells. J Bacteriol **177:**3965-3971.

47. **Kenjale, R., J. Wilson, S. F. Zenk, S. Saurya, W. L. Picking, W. D. Picking, and A. Blocker.** 2005. The needle component of the type III secreton of Shigella regulates the activity of the secretion apparatus. J Biol Chem **280:**42929-42937.

48. **Kinter, M., and N. E. Serman.** 2000. Protein sequencing and identification using tandem mass spectrometry. Wiley-Interscience, New York.

49. **Kleanthous, C.** 2010. Swimming against the tide: progress and challenges in our understanding of colicin translocation. Nat Rev Microbiol **8:**843-848.

50. **Kotloff, K. L., J. P. Winickoff, B. Ivanoff, J. D. Clemens, D. L. Swerdlow, P. J. Sansonetti, G. K. Adak, and M. M. Levine.** 1999. Global burden of Shigella infections: implications for vaccine development and implementation of control strategies. Bull World Health Organ **77:**651-666.

51. **Krissinel, E., and K. Henrick.** 2007. Inference of macromolecular assemblies from crystalline state. J Mol Biol **372:**774-797.

52. **Kueltzo, L. A., J. Osiecki, J. Barker, W. L. Picking, B. Ersoy, W. D. Picking, and C. R. Middaugh.** 2003. Structure-function analysis of invasion plasmid antigen C (IpaC) from Shigella flexneri. J Biol Chem **278:**2792-2798.

53. **Levine, M. M., K. L. Kotloff, E. M. Barry, M. F. Pasetti, and M. B. Sztein.** 2007. Clinical trials of Shigella vaccines: two steps forward and one step back on a long, hard road. Nat Rev Microbiol **5:**540-553.

54. **Lunelli, M., R. Hurwitz, J. Lambers, and M. Kolbe.** 2011. Crystal structure of PrgI-SipD: insight into a secretion competent state of the type three secretion system needle tip and its interaction with host ligands. PLoS Pathog **7:**e1002163.

55. **Lunelli, M., R. Lokareddy, A. Zychlinsky, and M. Kolbe.** 2009. IpaB-IpgC interaction defines binding motif for type III secretion translocator. Proc Natl Acad Sci U S A **106:**9661-9666.

56. **Mandic-Mulec, I., J. Weiss, and A. Zychlinsky.** 1997. Shigella flexneri is trapped in polymorphonuclear leukocyte vacuoles and efficiently killed. Infect Immun **65:**110-115.

57. **Mavris, M., A. Page, R. Tournebize, B. Demers, P. Sansonetti, and C. Parsot.** 2002. Regulation of transcription by the activity of the Shigella flexneri type III secretion apparatus. Mol Microbiol **43:**1543-1553.

58. **McCoy, A., R. Grosse-Kunstleve, L. Storoni, and R. Read.** 2005. Likelihood-enhanced fast translation functions. Acta Crystallogr D Biol Crystallogr **61:**458-464.

59. **McGhie, E. J., P. J. Hume, R. D. Hayward, J. Torres, and V. Koronakis.** 2002. Topology of the Salmonella invasion protein SipB in a model bilayer. Mol Microbiol **44:**1309-1321.

60. **Mohle-Boetani, J. C., M. Stapleton, R. Finger, N. H. Bean, J. Poundstone, P. A. Blake, and P. M. Griffin.** 1995. Communitywide shigellosis: control of an outbreak and risk factors in child day-care centers. Am J Public Health **85:**812-816.

61. **Monack, D. M., and J. A. Theriot.** 2001. Actin-based motility is sufficient for bacterial membrane protrusion formation and host cell uptake. Cell Microbiol **3:**633-647.

62. **Morita-Ishihara, T., M. Ogawa, H. Sagara, M. Yoshida, E. Katayama, and C. Sasakawa.** 2006. Shigella Spa33 is an essential C-ring component of type III secretion machinery. J Biol Chem **281:**599-607.

63. **Ménard, R., P. Sansonetti, C. Parsot, and T. Vasselon.** 1994. Extracellular association and cytoplasmic partitioning of the IpaB and IpaC invasins of S. flexneri. Cell **79:**515-525.

64. **Ménard, R., P. J. Sansonetti, and C. Parsot.** 1993. Nonpolar mutagenesis of the ipa genes defines IpaB, IpaC, and IpaD as effectors of Shigella flexneri entry into epithelial cells. J Bacteriol **175:**5899-5906.

65. **Niyogi, S. K.** 2005. Shigellosis. J Microbiol **43:**133-143.

66. **Ogawa, M., T. Yoshimori, T. Suzuki, H. Sagara, N. Mizushima, and C. Sasakawa.** 2005. Escape of intracellular Shigella from autophagy. Science **307:**727-731.

67. **Olive, A. J., R. Kenjale, M. Espina, D. S. Moore, W. L. Picking, and W. D. Picking.** 2007. Bile salts stimulate recruitment of IpaB to the Shigella flexneri surface, where it colocalizes with IpaD at the tip of the type III secretion needle. Infect Immun **75:**2626-2629.

68. **Organization, W. H.** 2004, posting date. Global burden of disease (GBD) 2002 estimates. [Online.]

69. **Orrù, S., F. Dal Piaz, A. Casbarra, G. Biasiol, R. De Francesco, C. Steinkühler, and P. Pucci.** 1999. Conformational changes in the NS3 protease from hepatitis C virus strain Bk monitored by limited proteolysis and mass spectrometry. Protein Sci **8:**1445-1454.

70. **Oswald, C., S. H. Smits, E. Bremer, and L. Schmitt.** 2008. Microseeding - a powerful tool for crystallizing proteins complexed with hydrolyzable substrates. Int J Mol Sci **9:**1131-1141.

71. **Otwinowski, Z. a. M., W.** 1997. Processing of X-ray Diffraction Data Collected in Oscillation Mode. Methods in Enzymology **276:**307-326.

72. **Page, A., M. Fromont-Racine, P. Sansonetti, P. Legrain, and C. Parsot.** 2001. Characterization of the interaction partners of secreted proteins and chaperones of Shigella flexneri. Mol Microbiol **42:**1133-1145.

73. **Parsot, C., C. Hamiaux, and A. Page.** 2003. The various and varying roles of specific chaperones in type III secretion systems. Curr Opin Microbiol **6:**7-14.

74. **Phalipon, A., and P. J. Sansonetti.** 2007. Shigella's ways of manipulating the host intestinal innate and adaptive immune system: a tool box for survival? Immunol Cell Biol **85:**119-129.

75. **Picking, W. L., H. Nishioka, P. D. Hearn, M. A. Baxter, A. T. Harrington, A. Blocker, and W. D. Picking.** 2005. IpaD of Shigella flexneri is independently required for regulation of Ipa protein secretion and efficient insertion of IpaB and IpaC into host membranes. Infect Immun **73:**1432-1440.

76. **Pilonieta, M., and G. Munson.** 2008. The chaperone IpgC copurifies with the virulence regulator MxiE. J Bacteriol **190:**2249-2251.

77. **Potterton, E., P. Briggs, Turkenburg, M, and E. Dodson.** 2003. A graphical user interface to the CCP4 program suite, p. 1131-1137. vol. D59. Acta Crystallography.

78. **Prouty, A. M., and J. S. Gunn.** 2000. Salmonella enterica serovar typhimurium invasion is repressed in the presence of bile. Infect Immun **68:**6763-6769.

79. **Quinaud, M., S. Plé, V. Job, C. Contreras-Martel, J. P. Simorre, I. Attree, and A. Dessen.** 2007. Structure of the heterotrimeric complex that regulates type III secretion needle formation. Proc Natl Acad Sci U S A **104:**7803-7808.

80. **Rocchia, W., S. Sridharan, A. Nicholls, E. Alexov, A. Chiabrera, and B. Honig.** 2002. Rapid grid-based construction of the molecular surface and the use of induced surface charge to calculate reaction field energies: applications to the molecular systems and geometric objects. J Comput Chem **23:**128-137.

81. **Sansonetti, P. J.** 2004. War and peace at mucosal surfaces. Nat Rev Immunol **4:**953-964.

82. **Sansonetti, P. J., J. Arondel, J. R. Cantey, M. C. Prévost, and M. Huerre.** 1996. Infection of rabbit Peyer's patches by Shigella flexneri: effect of adhesive or invasive bacterial phenotypes on follicle-associated epithelium. Infect Immun **64:**2752-2764.

83. **Sansonetti, P. J., A. Ryter, P. Clerc, A. T. Maurelli, and J. Mounier.** 1986. Multiplication of Shigella flexneri within HeLa cells: lysis of the phagocytic vacuole and plasmid-mediated contact hemolysis. Infect Immun **51:**461-469.

84. **Schroeder, G., and H. Hilbi.** 2008. Molecular pathogenesis of Shigella spp.: controlling host cell signaling, invasion, and death by type III secretion. Clin Microbiol Rev **21:**134-156.

85. **Schuch, R., and A. T. Maurelli.** 2001. MxiM and MxiJ, base elements of the Mxi-Spa type III secretion system of Shigella, interact with and stabilize the MxiD secretin in the cell envelope. J Bacteriol **183:**6991-6998.

86. **Schuch, R., and A. T. Maurelli.** 1999. The mxi-Spa type III secretory pathway of Shigella flexneri requires an outer membrane lipoprotein, MxiM, for invasin translocation. Infect Immun **67:**1982-1991.

87. **Schüttelkopf, A. W., and D. M. van Aalten.** 2004. PRODRG: a tool for high-throughput crystallography of protein-ligand complexes. Acta Crystallogr D Biol Crystallogr **60:**1355-1363.

88. **Soelaiman, S., K. Jakes, N. Wu, C. Li, and M. Shoham.** 2001. Crystal structure of colicin E3: implications for cell entry and ribosome inactivation. Mol Cell **8:**1053-1062.

89. **Spolaore, B., R. Bermejo, M. Zambonin, and A. Fontana.** 2001. Protein interactions leading to conformational changes monitored by limited proteolysis: apo form and fragments of horse cytochrome c. Biochemistry **40:**9460-9468.

90. **Stensrud, K. F., P. R. Adam, C. D. La Mar, A. J. Olive, G. H. Lushington, R. Sudharsan, N. L. Shelton, R. S. Givens, W. L. Picking, and W. D. Picking.** 2008. Deoxycholate interacts with IpaD of Shigella flexneri in inducing the recruitment of IpaB to the type III secretion apparatus needle tip. J Biol Chem **283:**18646-18654.

91.   **Sun, P., J. E. Tropea, B. P. Austin, S. Cherry, and D. S. Waugh.** 2008. Structural characterization of the Yersinia pestis type III secretion system needle protein YscF in complex with its heterodimeric chaperone YscE/YscG. J Mol Biol **377:**819-830.

92.   **Tampakaki, A. P., V. E. Fadouloglou, A. D. Gazi, N. J. Panopoulos, and M. Kokkinidis.** 2004. Conserved features of type III secretion. Cell Microbiol **6:**805-816.

93.   **Thompson, J., D. Higgins, and T. Gibson.** 1994. CLUSTAL W: improving the sensitivity of progressive multiple sequence alignment through sequence weighting, position-specific gap penalties and weight matrix choice. Nucleic Acids Res **22:**4673-4680.

94.   **Troisfontaines, P., and G. R. Cornelis.** 2005. Type III secretion: more systems than you think. Physiology (Bethesda) **20:**326-339.

95.   **Tsai, C. J., A. Del Sol, and R. Nussinov.** 2009. Protein allostery, signal transmission and dynamics: a classification scheme of allosteric mechanisms. Mol Biosyst **5:**207-216.

96.   **Veenendaal, A. K., J. L. Hodgkinson, L. Schwarzer, D. Stabat, S. F. Zenk, and A. J. Blocker.** 2007. The type III secretion system needle tip complex mediates host cell sensing and translocon insertion. Mol Microbiol **63:**1719-1730.

97.   **Wang, Y., A. N. Ouellette, C. W. Egan, T. Rathinavelan, W. Im, and R. N. De Guzman.** 2007. Differences in the electrostatic surfaces of the type III secretion needle proteins PrgI, BsaL, and MxiH. J Mol Biol **371:**1304-1314.

98.   **Wassef, J. S., D. F. Keren, and J. L. Mailloux.** 1989. Role of M cells in initial antigen uptake and in ulcer formation in the rabbit intestinal loop model of shigellosis. Infect Immun **57:**858-863.

99.   **Wiener, M., D. Freymann, P. Ghosh, and R. M. Stroud.** 1997. Crystal structure of colicin Ia. Nature **385:**461-464.

100. **Zakharov, S. D., E. A. Kotova, Y. N. Antonenko, and W. A. Cramer.** 2004. On the role of lipid in colicin pore formation. Biochim Biophys Acta **1666:**239-249.

101. **Zemla, A.** 2003. LGA: A method for finding 3D similarities in protein structures. Nucleic Acids Res **31:**3370-3374.

102. **Zhang, L., Y. Wang, A. J. Olive, N. D. Smith, W. D. Picking, R. N. De Guzman, and W. L. Picking.** 2007. Identification of the MxiH needle protein residues responsible for anchoring invasion plasmid antigen D to the type III secretion needle tip. J Biol Chem **282:**32144-32151.

103. **Zhang, L., Y. Wang, W. L. Picking, W. D. Picking, and R. N. De Guzman.** 2006. Solution structure of monomeric BsaL, the type III secretion needle protein of Burkholderia pseudomallei. J Mol Biol **359:**322-330.

104. **Zychlinsky, A., C. Fitting, J. M. Cavaillon, and P. J. Sansonetti.** 1994. Interleukin 1 is released by murine macrophages during apoptosis induced by Shigella flexneri. J Clin Invest **94:**1328-1332.

105. **Zychlinsky, A., M. C. Prevost, and P. J. Sansonetti.** 1992. Shigella flexneri induces apoptosis in infected macrophages. Nature **358:**167-169.

106. **Zychlinsky, A., K. Thirumalai, J. Arondel, J. R. Cantey, A. O. Aliprantis, and P. J. Sansonetti.** 1996. In vivo apoptosis in Shigella flexneri infections. Infect Immun **64:**5357-5365.

VITA

Michael Barta was born on April 10th, 1984 in the city of Overland Park, Kansas. He was educated in local public schools and graduated from Shawnee Mission East in 2002. He was recognized as the outstanding math and science student at his high school by Kansas State University in Manhattan, KS where he received a Bachelor of Science degree in Biology in the spring of 2007.

Upon receiving his degree, Michael began a master's program in cellular biology and biophysics at the University of Missouri-Kansas City in the fall of 2007. After one year in the program Mr. Barta transitioned into the interdisciplinary Ph.D program within the School of Biological Sciences at UMKC where he began his dissertation work under the guidance of Dr. Brian V. Geisbrecht. Completion of his dissertation research was accomplished in the summer of 2011.

Mr. Barta is a member of the American Society for Microbiology (ASM). He has authored several peer reviewed research articles in reputed international journals, including:

- **Coiled-coil Domain from Type Three Secretion System First Translocator Proteins Reveal Homology to Pore-forming Toxins. Michael L Barta**, Nicholas E. Dickenson, Mrinalini Patel, J. Andrew Keightley, William D. Picking, Wendy L. Picking and Brian V. Geisbrecht. 2011. (submitted) *J. Mol. Bio.*

- **Identification of the bile salt binding site on IpaD from *Shigella flexneri* and the influence of ligand binding on IpaD structure. Michael L Barta**, Manita Guragain, Philip Adam, Nicholas E. Dickenson, Mrinalini Patil, Brian V. Geisbrecht, Wendy L. Picking and William D. Picking. 2011. (Accepted in press) *Proteins*.

- **Crystal structures of *Staphylococcus epidermidis* Mevalonate Diphosphate Decarboxylase bound to inhibitory analogs reveal new insight into substrate binding and catalysis.**

99

Michael L Barta, D Andrew Skaff, William J McWhorter, Timothy J Herdendorf, Henry M

Miziorko and Brian V Geisbrecht. 2011. *J. Biol. Chem.* 286: 23900-23910. PMID: 21561869

- **Evidence for alternative quaternary structure in a bacterial Type III secretion system
  chaperone. Michael L Barta**, Lingling Zhang, Wendy L Picking, Brian V Geisbrecht. 2010.
  BMC Structural Biology. 10:21. PMID: 20633281

. Mr. Barta is currently interviewing for Postdoctoral Fellowship positions at several

laboratories where he will continue his work in the microbial pathogen field.